

Universität  
Rostock



Traditio et Innovatio

**NOVEL FIBER-BASED PROBE FOR LOCALISED OPTICAL STIMULATION AND  
ELECTROPHYSIOLOGICAL RECORDING IN OPTOGENETICS**

Dissertation zur Erlangung des akademischen Grades  
Doktor - Ingenieur (Dr.-Ing.)  
der Fakultät für Informatik und Elektrotechnik  
der Universität Rostock

---

vorgelegt von

Jelena Petrovic

geboren am 07.03.1990.

in Brcko

aus

Rostock

---

Rostock, 2022

[https://doi.org/10.18453/rosdok\\_id00004173](https://doi.org/10.18453/rosdok_id00004173)

**Thesis reviewers:**

Prof. Dr.-Ing. Dennis Hohlfeld, Institute of Electronic Appliances and Circuits, University of Rostock

Prof. DR. Maria Asplund, Department of Microtechnology and Nanoscience, Electronics Materials and Systems Laboratory, Chalmers University of Technology, Gothenburg Sweden

This work was carried out between January 2019 and August 2022 under supervision of Prof. Dr.-Ing. Dennis Hohlfeld at the Institute of Electronic Appliances and Circuits, University of Rostock.

Submission: September, 2022

Defense: December, 2022

## **Selbstständigkeitserklärung**

Ich versichere hiermit, die vorliegende Dissertation eigenständig und ausschließlich unter Verwendung der angegebenen Hilfsmittel angefertigt zu haben. Alle öffentlichen Quellen sind als solche kenntlich gemacht.

Rostock, September 2022

M.Sc. Jelena Petrovic

Hiermit erkläre ich, dass die vorgelegte Promotionsschrift bisher weder im Ausland noch im Inland in gleicher oder ähnlicher Form einer anderen Prüfungsbehörde vorgelegt wurde.

Rostock, September 2022

M.Sc. Jelena Petrovic

*Dedicated to my husband, who supported me and showed me that I can achieve  
more than I ever thought.*

# Abstract

---

Deep brain stimulation has provided remarkable benefits for people with a variety of neurologic conditions. Besides the advantages of electrical stimulation-based prostheses, a major limitation of these devices is the difficulty to locally constrain the electrical field to attain accurate and precise stimulation of preferably individual single cells. This reduces the device's efficacy and gives rise to potential side effects, such as unintended stimulation of non-targeted brain regions or stimulation of non-therapeutic cell types within the targeted tissue. Genetic modification of nerve cells with ion channels that are sensitive to light brought the promising new method of optogenetics into neuroscience. This unique neuromodulation technique allows optical control of genetically targeted specific neurons that express light sensitive proteins (opsins) integrated into the cell membrane. To achieve light delivery and simultaneous electrophysiological recording from the nervous system, scientists and engineers designed dual optical and electrical probes. The combination of optical and electrical elements in one single probe is referred to as an optrode.

Optrodes usually represent a combination of optical fiber or waveguide (as light guiding structure) and single or multiple microelectrodes that enable simultaneous light delivery and electrophysiological recording. Fiber-based optrodes, are mostly assembled by simply gluing of flat cleaved optical fiber to one or multiple microelectrodes. In rare scenarios, tapered fibers are used as light delivery tools, while metal coatings serve as microelectrodes.

This thesis explains fabrication process of fiber-based optrode consisting of tapered optical fiber with two deposited gold electrodes on its surface. Furthermore, design and construction of custom mechanical grinding setup, that enables fabrication of tapered fiber tips of good optical quality with various cone angles, represents an important part of this thesis. Detailed optical and electrical characterization of fabricated optrodes is also presented.

The fiber tip is formed by mechanical grinding and subsequent polishing of a cleaved optical fiber end using a custom made setup consisting of a horizontal spinning polishing disc and a rotating optical fiber placed on an angular stage, enabling the fabrication of a tapered conical fiber tip with a wide range of cone angles. The influence of process parameters (e.g. rotation speed of grinding disc and fiber rotating fiber, processing time, and grit size of polishing discs) on quality of fabricated cone fiber tips is discussed in detail. Gold electrodes are deposited on the cylindrical fiber surface by magnetron sputtering through a shadow mask, aligned and fixed on custom made fiber holder. In order to deposit multiple electrodes on the same optical fiber, a custom precision fiber rotation setup is used. Methods for improvement of electrode adhesion to fiber surface are also presented. To expose only a small portion of deposited electrodes in tapered region, heat shrink tube is applied, Optrode is then assembled by establishment of electrical contacts between deposited electrodes and printed circuit board (PCB) using conductive silver epoxy. Coupling to a light source is achieved by butt coupling of flat cleaved optrode end to patch LED-coupled optical fiber.

Emission profiles of multiple fiber tip geometries are visualized by placing tapered fibers in a non-scattering medium, Rhodamine-6G solution. Green light was coupled into the optrode for the fluorescence excitation. Effect of cone angle of tapered fiber tip on emission profile is discussed in detail. Application of an integrating sphere enabled investigation of cone angle

effect on total transmitted light power. Detailed analysis of beam shape and illumination volume dependence on cone angle is achieved by obtaining beam profiles at various distances from fiber tip end.

Geometry of deposited microelectrodes is investigated using scanning electron microscope (SEM) and profilometry measurements. Electrochemical impedance spectroscopy (EIS) is applied as a tool for characterization of recording capability of deposited electrodes. The effect of the size of electrode area on impedance magnitude at 1 kHz and cut-off frequency is discussed in terms of electrode's recording capability.

**Keywords:** optrode, optical fiber, optical stimulation, electrical recording, tapered optical fibers

# Zusammenfassung

---

Die tiefe Hirnstimulation hat Menschen mit unterschiedlichen neurologischen Erkrankungen bemerkenswerte Vorteile gebracht. Neben den Vorteilen von auf Elektrostimulation basierenden Prothesen besteht eine Haupteinschränkung dieser Vorrichtungen in der Schwierigkeit, das elektrische Feld lokal einzuschränken, um eine genaue und präzise Stimulation vorzugsweise einzelner Zellen zu erreichen. Dies verringert die Wirksamkeit des Geräts und führt zu potenziellen Nebenwirkungen, wie z. B. einer unbeabsichtigten Stimulation nicht betroffener Gehirnregionen oder einer Stimulation nicht therapeutischer Zelltypen innerhalb des Zielgewebes. Die genetische Veränderung von Nervenzellen mit lichtempfindlichen Ionenkanälen brachte die vielversprechende neue Methode der Optogenetik in die Neurowissenschaften. Diese einzigartige Neuromodulationstechnik ermöglicht die optische Kontrolle einzelner, genetisch modifizierter Neuronen. In die Zellmembran dieser Neuronen sind lichtempfindliche Proteine (Opsine) integriert. Um eine Lichtabgabe und gleichzeitige elektrophysiologische Aufzeichnung aus dem Nervensystem zu gewährleisten, haben Wissenschaftler und Ingenieure Kombinationen aus optischen und elektrischen Sonden entwickelt. Die Integration optischer und elektrischer Elemente in eine einzige Sonde wird als Optrode bezeichnet.

Optroden stellen normalerweise eine Kombination aus Glasfaser oder Wellenleiter (als Lichtleitstruktur) und einzelnen oder mehreren Mikroelektroden dar, die eine gleichzeitige Lichtabgabe und elektrophysiologische Aufzeichnung ermöglichen. Faserbasierte Optroden werden meist durch einfaches Kleben einer flachen, gespaltenen optischen Faser auf eine oder mehrere Mikroelektroden zusammengebaut. In seltenen Fällen werden sich verjüngende Fasern als Lichtübertragungswerkzeuge verwendet, während Metallbeschichtungen als Mikroelektroden dienen.

Diese Arbeit konzentriert sich auf die Erstellung eines Herstellungsprozesses einer faserbasierten Optrode, die aus einer sich verjüngenden optischen Faser besteht mit zweiauf ihre Oberfläche aufgebrachten Metallelektrodenabgeschiedenen Metallelektroden auf ihrer Oberfläche besteht. Darüber hinaus stellen das Design und die Konstruktion eines kundenspezifischen mechanischen Schleifaufbaus, der die Herstellung konischer Faserspitzen von guter optischer Qualität mit verschiedenen Konuswinkeln ermöglicht, einen wichtigen Teil dieser Arbeit dar. Eine detaillierte optische und elektrische Charakterisierung der hergestellten Optroden wird ebenfalls vorgestellt.

Die Faserspitze wird durch mechanisches Polieren eines gespaltenen optischen Faserendes unter Verwendung eines maßgeschneiderten Aufbaus gebildet, der aus einer horizontal rotierenden Polierscheibe und einer rotierenden optischen Faser besteht, die auf einem Winkeltisch platziert ist. Dies ermöglicht die Herstellung einer sich verjüngenden konischen Faserspitze mit unterschiedlichen Kegelwinkeln. Der Einfluss von Prozessparametern (z. B. Rotationsgeschwindigkeit der Schleifscheibe und Faserrotationsfaser, Bearbeitungszeit und Körnung der Polierscheiben) auf die Qualität der hergestellten Kegelfaserspitzen wird ausführlich diskutiert. Goldelektroden werden auf der zylindrischen Faseroberfläche durch eine Schattenmaske aufgebracht, ausgerichtet und auf einem maßgefertigten Faserhalter fixiert. Um mehrere Elektroden auf derselben optischen Faser zu sputtern, wird ein kundenspezifischer

Präzisions-Faserrotationsaufbau verwendet. Verfahren zur Verbesserung der Elektrodenhaftung an der Faseroberfläche werden ebenfalls vorgestellt. Um nur einen kleinen Teil der abgeschiedenen Elektroden im verjüngten Bereich freizulegen, wird ein Schrumpfschlauch angebracht, Optrode wird dann zusammengebaut, indem elektrische Kontakte zwischen den aufgebracht Elektroden und der Leiterplatte (PCB) unter Verwendung von leitfähigem Silberepoxid hergestellt werden. Die Kopplung mit einer Lichtquelle wird durch Stoßkopplung eines flach gespaltenen Optrodenendes mit einer Patch-LED-gekoppelten optischen Faser erreicht.

Emissionsprofile mehrerer Faserspitzengeometrien werden sichtbar gemacht, indem konische Fasern in ein nicht streuendes Medium, Rhodamin-6G-Lösung, gelegt werden. Zur Fluoreszenzanregung wurde grünes Licht in die Optrode eingekoppelt. Die Auswirkung des Konuswinkels der sich verjüngenden Faserspitze auf das Emissionsprofil wird im Detail diskutiert. Die Anwendung einer integrierenden Kugel ermöglichte die Untersuchung des Kegelwinkeleffekts auf die gesamte durchgelassene Lichtleistung. Eine detaillierte Analyse der Strahlform und der Abhängigkeit des Beleuchtungsvolumens vom Kegelwinkel wird erreicht, indem Strahlprofile in verschiedenen Abständen vom Ende der Faserspitze untersucht werden.

Die Geometrie abgeschiedener Mikroelektroden wird mit Rasterelektronenmikroskopie (SEM) und Profilometriemessungen untersucht. Elektrochemische Impedanzspektroskopie (EIS) wird als Werkzeug zur Charakterisierung der Aufzeichnungsfähigkeit von abgeschiedenen Elektroden angewendet. Die Auswirkung der Größe der Elektrodenfläche auf die Größe der Impedanz bei 1 kHz und der Grenzfrequenz wird im Hinblick auf die Aufzeichnungsfähigkeit der Elektrode diskutiert.

**Schlüsselwörter:** Optrode, optische Faser, optische Stimulation, elektrische Aufzeichnung, konische optische Faser



# Acknowledgements

---

First, I would like to thank Prof. Dr.-Ing. Dennis Hohlfeld, my scientific advisor at the Institute of Electronic Appliances and Circuits (IGS), for arousing my interest in this project. I am very grateful for your time, advices, and support. Many thanks for giving me the opportunity to conduct this research.

I would like to express my sincere gratitude to Prof. Dr. Maria Asplund, my thesis reviewer, for providing me with valuable information required to make this thesis complete. Thank you for invested time and very useful advices in field of electrode characterization and improvement.

My special thanks go to Dr.-Ing. Fred Lange, who was helping me with all technical issues. Without your support in laboratory and willingness to help this work would not be possible.

I would like to thank M.Sc. Henning Bathel, former master student during this thesis, for the effort he invested to analyze and improve electrode deposition process.

Further thanks goes to Dr. rer. nat. Haldor Hartwig, who gave me useful advices concerning optical characterization of fabricated optrode, and MSc. Ulrike Fitzer who helped me with german language.

I would like to thank the entire team of the Institute of Electronic Appliances and Circuits for a great professional atmosphere. Special thanks go to Dr.-Ing. Andrej Novikov for his willingness to help me with various equipment I needed to complete my research. Many thanks to Michael Otto and Britta Wederka for a fast fabrication of printed circuit boards and photomasks.

Last, but not least, my deepest and warmest acknowledgements are extended to my close family who believed in me and supported me through this process. Tihomir, thank you for being my biggest support. Without your understanding and encouragement, this academic journey would be extremely difficult.

# Table of contents

---

Prof. Dr.-Ing. Dennis Hohlfeld, .....	II
1 Introduction.....	1
1.1 Electrical stimulation and recording in neuroscience .....	2
1.2 Optogenetics .....	7
1.2.1 Light delivery tools .....	9
1.2.2 Optrodes.....	12
1.3 Research objectives and thesis outline .....	20
2 Optrode microfabrication.....	23
2.1 Fiber tip formation .....	23
2.1.1 Methods .....	23
2.1.2 Results and discussion .....	27
2.2 Electrode deposition .....	31
2.2.1 Sputtering deposition.....	31
2.2.2 Methods .....	33
2.2.3 Results and discussion .....	37
2.3 Mechanical support and electrode insulation.....	39
2.3.1 Materials and methods .....	40
2.3.2 Mechanical testing .....	43
2.4 Optrode assembly .....	45
2.4.1 Establishment of electrical contacts.....	46
2.4.2 Coupling to a light source .....	47
3 Optical characterization .....	50
3.1 Optical fibers for light delivery .....	50
3.2 Transmission measurements.....	53
3.2.1 Measurement procedure .....	53
3.2.2 Results and discussion .....	55
3.3 Emission profiles.....	58
3.3.1 Experimental procedure.....	58
3.3.2 Results and discussion .....	59
3.3.3 Estimation of emission profile in brain tissue .....	63
3.4 Beam profiles.....	67
3.4.1 Experimental procedure.....	68
3.4.2 Results and discussion .....	69
4 Electrical characterization .....	73

4.1 Electrical resistance .....	73
4.1.1 Measurement procedure .....	74
4.1.2 Results and discussion .....	74
4.2 Electrochemical impedance spectroscopy .....	75
4.2.1 Electrode interface in brain and impedance of recording electrodes.....	79
4.2.2 Measurement procedure .....	82
4.2.3 Results and discussion .....	83
5 Conclusions and outlook .....	86
5.1 Conclusions.....	86
5.1.1 Fabrication .....	86
5.1.2 Optical and electrical characterization.....	88
5.2 Recommendations and future work.....	89
5.2.1 Improvement of fabrication process .....	89
5.2.2 Improvement of characterization methods and optrode functionality .....	90
6 Bibliography.....	91

# Nomenclature

---

SYMBOL	MEANING	UNIT
$\alpha$	semi-cone angle	degree
$\beta$	cone angle	degree
$\gamma$	incidence angle at core-cladding interface	degree
$\gamma_c$	critical angle for TIR	degree
$\gamma_{max}$	divergence angle	degree
$\gamma_i$	incidence angle at core-surrounding medium interface	degree
$\theta$	polishing angle	degree
$\lambda$	wavelength	nm
$\mu_t$	extinction coefficient	$cm^{-1}$
$\mu_a(\lambda)$	tissue absorption coefficient	$cm^{-1}$
$\mu_s(\lambda)$	tissue scattering coefficient	$cm^{-1}$
$\rho_{gold}$	electrical resistivity of gold at room temperature	$\Omega m$
$\phi$	phase shift	rad
$\omega$	angular frequency	rad/s
$A_{el}$	average electrode cross section area	$\mu m^2$
<b><math>B</math></b>	magnetic field vector	-
$C_{dl}$	capacity of double layer	F
$D_0$	radius of fiber core	$\mu m$
$d_{1/2}$	taper emitting length	$\mu m$
<b><math>E</math></b>	electric field vector	-
$f$	frequency	Hz
$f_{cut-off}$	cut-off frequency	Hz
$g$	anisotropic factor for biological tissue	-
$I$	current	A
$I_0$	initial light power	$W/mm^2$
$I(z)$	light power after travelled distance z	$W/mm^2$
$K$	absorption per unit thickness (K-M theory)	$mm^{-1}$
$l$	electrode length	mm
$m$	number of TIRs in cone tip	-
$n$	refractive index of surrounding medium	-
$n_{cl}$	refractive index of fiber cladding	-
$n_{co}$	refractive index of fiber core	-
$n_b$	refractive index of brain tissue	-
$n_t$	refractive index of tissue	-
$p$	pressure	mbar
$R$	electrical resistance	$\Omega$

$R_s$	electrical resistance of electrolyte	$\Omega$
$R_{ct}$	charge transfer resistance	$\Omega$
$r$	radial distance in cylindrical coordinates	mm
$S$	scattering per unit thickness (K-M theory)	$\text{mm}^{-1}$
$t$	time	s
$U$	DC voltage	V
$V(t)$	AC voltage	V
$Z$	impedance	$\Omega$
$Z_{im}$	imaginary impedance part	$\Omega$
$Z_{re}$	real impedance part	$\Omega$
$Z_{1\text{kHz}}$	impedance at 1 kHz	$\Omega$
$z$	height in cylindrical coordinates	mm

# Acronyms

---

2D	two - dimensional
3D	three - dimensional
AC	alternating current
AFM	atomic force microscopy
CE	counter electrode
CI	cochlear implant
DC	direct current
DLC	double layer capacitance
EAP	extracellular action potential
EIS	electrochemical impedance spectroscopy
K-M	Kubelka-Munk
LD	laser diode
LED	light emitting diode
LFP	local field potential
MEA	micro electrode array
MEOA	micro electrode optrode array
NA	numerical aperture
oCI	optical cochlear implant
PBS	phosphate buffered saline
PCB	printed circuit board
PTFE	Polytetrafluoroethylene
PVD	physical vapor deposition
RE	reference electrode
SEM	scanning electron microscopy
SNR	signal to noise ratio
TIR	total internal reflection
TIS	total internal scatter
UEA	Utah electrode array
USEA	Utah slanted electrode array
UV	ultra violet
WE	working electrode



# 1 INTRODUCTION

Due to its extreme complexity, understanding the brain has always been challenging. Nervous system consists of numerous diverse types of interconnected nerve cells (neurons) forming functional circuits responsible for motoric and behavior control. Signals transmitted by the nervous system are electrical in nature. Such electrical signals travel through neuron network carrying information within central nervous system, as well as to peripheral neurons located in different body parts. Neuroscientists discovered that similar signals can be artificially induced by an electrical stimulus applied externally to the neuron. This led to a possibility of neuroscientists not only being able to monitor neural activity, but also to have control of neurons and to manipulate their activity with simultaneous observation of its effect on behavior. Further research aims to answer a very complex question: how neural circuits cooperate to produce certain behaviors as a function of external stimulus.

After discovery that neuronal activity relies on depolarization of its cell membrane, and thus can be manipulated by delivering a small current in targeted brain region, neuroscientists started experiments using implanted microelectrodes to artificially depolarize or hyperpolarize neuron's cell membrane. This approach represents the basis for application of neural prostheses, first in animals and then also successfully in humans. Neural prostheses are defined as assistive devices or systems that replace or restore sensory, motor, and cognitive functions resulting from neural damage [1, 2]. Over the past decades, these prosthetic devices have improved in terms of accuracy, reduced invasiveness, and their overall effectiveness on control of neurological disorders like epilepsy, hearing restoration, Parkinson's disease, and many others.

The possibility to genetically modify neurons, responsible for some neurologic disorders, and enable their manipulation with light opened a new era of optogenetics. Instead of using electrical current to manipulate neuron activity, it can be achieved in less invasive manner by delivering light to targeted brain region. Light is usually delivered by optical fibers or waveguides. To confirm optical neuromodulation, microelectrodes are implanted together with light delivery tool. Optogenetic devices are currently extensively used in experiments with animals, especially mice and rats. When fabricating a device for neural stimulation, biological aspects have to be taken into consideration to minimize tissue damage during implantation.

An introduction to field of optogenetics, with description of various optogenetic devices will be presented in this chapter. Mechanism of electrical stimulation and recording is described briefly providing enough information to enable reader to spot the difference between that and optical neuromodulation achieved by optogenetics, as well as to understand the mechanism of electrophysiological recording that is also used in optogenetic experiments. Detailed description of components incorporated in various designs (light delivery tools, electrode types) of reported optogenetic devices is presented to describe state-of-the-art, and provide better understanding of development achieved in this research. A broader discussion of genetic modification techniques and tools applied in optogenetics does not fall within the scope of this thesis, and thus will not be presented. Main goal of this thesis is to present a detailed engineering approach to design and fabrication of novel optogenetic device, as well as to test its functionality.



## 1.1 Electrical stimulation and recording in neuroscience

Most nervous system disorders result from lost neural functionality in sensory or motor system. Thanks to therapeutic interventions, developed in a field of neural prosthesis, some of the lost neural functions are successfully restored by selective electrical stimulation of sensory or motor pathways, or by harnessing activity recorded from remnant neural pathways [3]. Electrodes chronically interfaced to the central and peripheral nervous systems represent the basis of the current and emerging neural prostheses, with various applications including upper and lower limb prostheses for spinal cord injury and stroke; bladder prostheses; cochlear and brain-stem auditory prostheses; retinal and cortical visual prostheses; cortical recording for cognitive control of assistive devices; nerve stimulation for epilepsy and depression; and deep brain stimulation for essential tremor, Parkinson's disease, epilepsy, dystonia, and depression [4].

According to numerous experimental results, it has been shown that electrical stimulation may cause alterations in trans-membrane potential, established by the balance of intracellular and extracellular ionic concentration, of excitable cells [5–9]. Electrical potential of the neuron (measured in Volts) is created by the difference in charge between the intracellular and extracellular side of the cell membrane, whose resting potential is approximately  $-70$  mV [10]. When ion channels are opened, ions are triggered to move through ion channels, generating a measurable ion current. Compared to a membranes resting potential, generated ion current can make membrane potential more positive (depolarization), or more negative (hyperpolarization) depending on charge of flowing ions.

As an example, in response to the external electric field, neurons in resting state will experience opening of cation channels, leading to generation of ion currents, resulting in rapid depolarization followed by repolarization, hyperpolarization and finally returning a neuron in a resting state (Figure 1.1), which is usually recorded as an action potential (spike). Action potential is triggered by a small depolarization of the resting membrane potential (around  $-60$  mV). Reaching the depolarization limit leads to the opening of voltage-gate of  $\text{Na}^+$  channels ( $-55$  mV) causing a rapid influx of  $\text{Na}^+$  ions which depolarize the membrane towards  $+40$  mV. The  $\text{Na}^+$  channels inactivate (a form of closure) within a millisecond, and the voltage-gated  $\text{K}^+$  channels open causing the efflux of  $\text{K}^+$  ions leading to membrane repolarization back to  $-60$  mV or beyond to more negative potentials (hyperpolarization). Next, to reset and maintain resting potential, the mechanism of  $\text{Na}^+/\text{K}^+$  ion exchange takes place across the cell membrane through so called ion pump, but on a much slower timescale compared to a depolarization.

In a typical electrophysiological recording, signal is detected by a microelectrode which transmits the signal to an amplifier, and then to oscilloscope. Since the electrical recording represents a comparison between the electrical properties of stimulated and non-stimulated neurons, two identical microelectrodes are necessary: the recording electrode and a reference electrode (placed outside the photo-stimulated region). The signals from both, reference and recording, electrodes are equally processed. After receiving and comparing both signals (from recording and reference electrode) from amplifier, an oscilloscope displays the membrane voltage over time, which represents the major source of data output in electrophysiological recording.

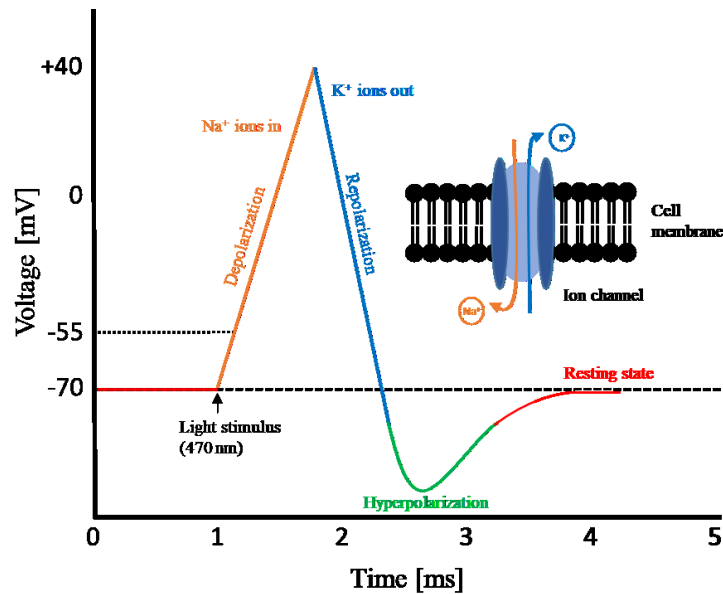


**Figure 1.1:** General representation of an action potential formation in neuron as a result of electrical stimulation.

Electrical recordings can be categorized into two main types based on the recording electrode placement in relation to the stimulated cell. First type of recording is extracellular (with the electrode positioned outside the cell of interest) and, because of simplicity, it represents the most common approach. Intracellular recording, represents the second recording type which requires a precise electrode positioning inside the cell of interest. In case of *in vivo* experiments with freely moving animals, it represents a serious limitation which makes this approach rarely used, and limited to *in vitro* experiments. Temporary difference in potential of the outer surface of activated neuron, is generated as a consequence of dramatic changes in membrane voltage occurring during action potential. Therefore, action potentials can be detected in the extracellular space near the membrane of an active neuron by measuring the potential difference between the tip of a recording electrode and a reference electrode placed in a distant extracellular position [10]. No potential difference between the extracellular recording electrode and the reference electrode points to absence of neural activity.

New generation of penetrating microelectrode array (MEA) designs [9–12], providing selective access to neurons of central and peripheral nervous system, has improved electrical stimulation and recording capabilities, and thus formed the basis for new therapies in case of nervous system disorders. Implantation of such electrode arrays enable direct communication with still-functioning parts of the sensory and motor neural pathways. Stimulation and recording from still-functioning neurons makes it possible to bypass, to a limited degree, damaged regions of the nervous system [1].

Since they can be safely inserted directly into the central or peripheral nervous system, needle-shaped microelectrodes are mostly used in microelectrode arrays (MEAs) for electrical stimulation and recording, enabling recording of spatially distributed neural activity patterns and recreating such patterns by passing temporal patterns of electrical currents through selected electrodes in the interface. The very tip of such microelectrodes is left uninsulated, enabling selective stimulation and recording from individual neural cells, as well as from the small volume containing neurons located around the electrode tip [3]. The Utah Electrode Array (UEA) [11], consisting of a hundred 1.5 mm long micro needles built on a square grid with mutual spacing of 400  $\mu\text{m}$ , represents an example of such three-dimensional (3D) neural

interface (Figure 1.2[12]). The entire array, with the exception of the very tip of each micro needle is insulated with biocompatible polymer. In order to facilitate electronic to ionic transduction, each micro needle tip is usually metalized with iridium oxide. Modification of this design, known as Utah Slanted Electrode Array (USEA), differs only in microelectrode lengths graded from 0.5 mm to 1.5 mm along the array length.

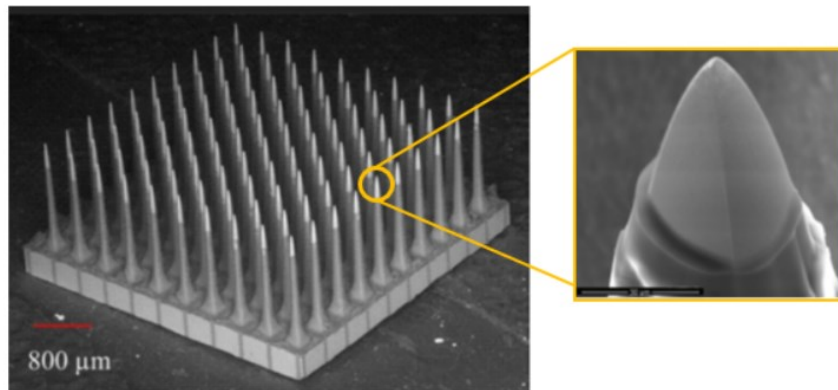


**Figure 1.2:** The Utah Electrode Array (UEA) containing a hundred of 1.5 mm long penetrating microelectrodes built on a square grid with 400  $\mu\text{m}$  spacing [12].

Efficacy of such devices (probes) is strongly dependent on size and electrical properties of implanted microelectrodes. Since electrode surface forms physical contact with electrolyte present in brain, it represents the key element in probe design. Ideally, if designed for recording purposes, an electrode should accurately record signals without the influence on its quality. Microscopic electrode surface would be ideal for high spatial resolution in stimulation and recording. However, due to limited surface area interacting with liquid, smaller electrodes are expected to have higher electrochemical impedance, and therefore require higher voltage to drive current over the interface. This may increase risks of corrosion or electrolysis.

Over past decades, researchers have produced a variety of electrode materials enabling application of very small electrodes for electrical stimulation and recording without a serious risk of a tissue damage and electrode degradation. Such electrode materials consist of corrosion-resistant stainless steel and noble metals complemented with conductive polymers, carbon materials, metal oxides and various composites [13–15]. Increasing electrode efficacy by enlargement of its electrochemically active surface, usually achieved by roughening of flat noble metal electrode surface, showed very promising results [16, 17]. Beside above mentioned requirements, to achieve longevity of electrode's function, electrode must be resilient to swelling, delamination, dissolution and corrosion.

Beside all the advantages of electrical stimulation-based prostheses, a major limitation of such devices is their low spatial resolution in delivering stimulation signals and the difficulty to locally constrain the electric field to attain accurate and precise stimulation of preferably individual single cells [18]. These limitations contribute to the inconsistent efficacy and sometimes serious side effects, such as unintended stimulation of non-targeted tissue regions [19] or stimulation of non-therapeutic cell types within the targeted tissue. Since the electrical spread into non-targeted regions is one cause of side effects, they can often be reduced or eliminated by adjusting the electrical pulse parameters [20]. Unfortunately, a reduction of side effects is frequently accomplished at the cost of decreased treatment efficacy [21], and there is

a need for a new technologies to achieve improved stimulation efficiency with minimum side effects.

Extracellular microelectrodes for in vitro and in vivo recordings of neural electrical activity are constantly being investigated and improved to increase spatiotemporal resolution and enable capturing of the dynamics of individual neurons, as well as interactions within neural networks [22–24]. High density MEAs are capable of providing long term high resolution mapping of local field potentials (LFPs) and extracellular action potentials (EAPs) from neuron population at the spatial scales below 100  $\mu\text{m}$  [25]. Spatial resolution of such MEAs can be increased by increasing the number of microelectrodes in array, and thus increasing number of available readout channels. However, to minimize invasiveness during the implantation, number and size of these electrodes needs to be carefully chosen. A wide range of electrode sizes (5-120  $\mu\text{m}$  in diameter) has been used for extracellular recording [26–30]. Optimal electrode size depends on recording requirements. A common assumption is that small electrodes (diameter < 20  $\mu\text{m}$ ) should be used for detection of EAPs from only few nearby neurons, while larger electrodes (diameter > 50  $\mu\text{m}$ ) are well suitable for recording population-wide LFPs [31]. Electrode-electrolyte interface, and the overall electrode area should also been taken into consideration [32]. Enhancement of electrode recording performance by application of novel nanomaterials show promising results [33, 34].

To understand the effect of electrode size in extracellular potential recordings, as well as to determine which electrode is more suitable for resolving details of extracellular field distribution, main characteristic of both, extracellular action potential (EAP) and local field potential (LFP), have to be considered. The feature of EAPs of individual neurons helps to understand neuron morphology. Based on previous research [32], in cortical cell cultures, peak amplitude values of EAP range from 1  $\mu\text{V}$  to 1.7 mV with a signal duration between 0.5ms and 2ms. Furthermore, due to the fact that cell cultures don't form a dense tissue layer on the electrode, potential distributions in cell cultures are more localized (fall off quickly at 20 up to 100  $\mu\text{m}$  radius from the peak) compared to those in acute brain slices (fall off within a radius of 50–150  $\mu\text{m}$  from the peak). According to the same research [32], amplitudes of LFPs are comparably larger, ranging from 0.1 mV to 1.5 mV. Spatial extension of an LFP event ranges between few hundreds micrometres and several millimetres, lasting few hundred milliseconds in brain slices. Since the presence of LFPs indicates network connectivity, they are often used to study seizures [35, 36]. It is important to mention that spatiotemporal features of extracellular potentials also depend on brain region, as well as on sample preparation in case of in vitro experiments. Electrode size may influence detection of EAP or LFP signals (Figure 1.3) and therefore, to obtain relevant information from extracellular potential, it is important to know the effect of electrode size on specific recording scenario.

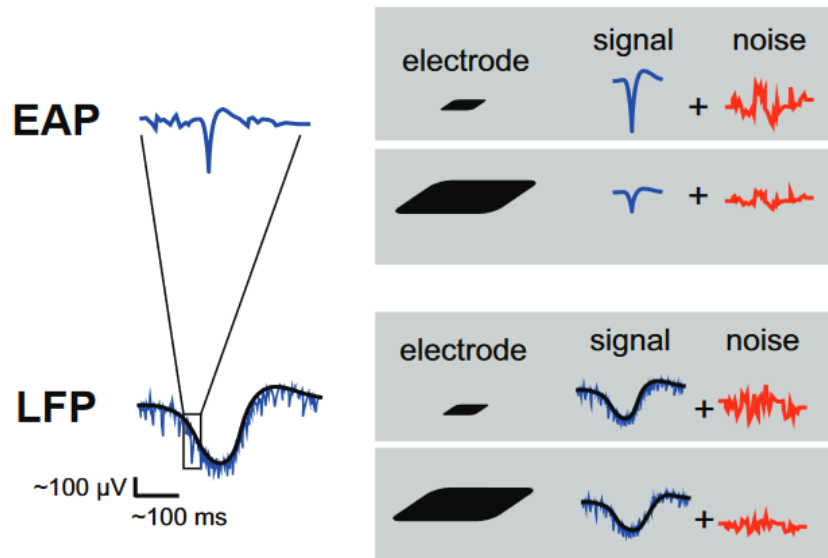


**Figure 1.3:** Microelectrodes for extracellular action potential (EAP) and local field potential (LFP) signal recording. Spatial signal averaging is affected by electrode size. Electrode size determines the capability to resolve local features of specific neurons. Image adapted from [32].

The amount of charges detected in a given environment is determined by electrode size. Therefore, larger electrodes detect potentials over a larger area, but they may also contribute to blurring highly local events due to spatial averaging (i.e., recorded signal is averaged over a comparably large surface) which also affects the peak signal amplitude [32]. Findings from a recent study [32] suggest that spatial averaging due to electrode size is highly dependent on the position of the signal source. Close positioning of recording electrode in respect to the signal source (approximately  $1\ \mu\text{m}$  distance) leads to enhancement of averaging effect in case of larger electrodes (95% reduction of signal amplitude). However, as the distance from signal source increases, spatial averaging becomes negligible. As an example, at a distance of approximately  $100\ \mu\text{m}$  from the signal source, two electrodes made of same material with a large difference in recording areas ( $1\ \mu\text{m}\times 1\ \mu\text{m}$ , and  $100\ \mu\text{m}\times 100\ \mu\text{m}$ ) provided approximately the same signal amplitudes. Furthermore, differences in relative signal amplitudes, in case of various electrode sizes, become rather small as soon as recording electrode is moved to a distance of  $18\ \mu\text{m}$  from signal source [32]. Impedance of the electrode, determined by electrode-electrolyte interface area (electrode size), represents another factor that may contribute to signal attenuation. Size dependence of signal attenuation of recording electrodes is usually obtained through electrochemical impedance spectroscopy.

Beside aforementioned electrode characteristics, another factors that may affect recorded signals are: location of the electrode in respect to neuron, presence of glial cells on the electrode surface, determination of exact location of neuronal signal source, and noise in extracellular recording. If the electrode is covered by glial cells that affect spreading, signal will be attenuated. Not being able to determine exact location of neuronal signal source may affect the amplitude of recorded signal. The probability of an electrode being at the right spot is directly related to electrode size and density [32]. As a solution, larger electrodes are used to increase the probability of electrode positioning close to the signal source. However, as already mentioned, this approach would result in increased spatial averaging. Another way represents using of dense MEAs which will avoid spatial averaging while increasing probability that at least one electrode will be at the right spot. Noise in extracellular recording represents contribution from all signals that interfere with neuronal signal of interest. Inherent thermal

noise of the electrodes, background activity and the noise of recording amplifiers represent three main types of noise that affects extracellular recorded signals. Background activity comes from electrical signals of more distant neurons that cannot be identified.

## 1.2 Optogenetics

Genetic modification of nerve cells with light sensitive ion channels brought the promising new method of optogenetics into the neuroscience [37]. In contrast to electrical stimulation, optogenetics uses light which has satisfying penetrating capability and is minimally invasive. Other practical advantages of optogenetics over electrical stimulation include minimal instrumental interferences with simultaneous electrophysiological recording as well as scalable optical tools for accessing large-scale neural networks [20]. Announced as the method of the year in 2010, optogenetics provides a unique neuromodulation technique allowing optical control of genetically targeted neurons expressing light sensitive proteins (opsins) integrated in cell membrane. The relevant light sensitive proteins generate light sensitive ion pumps or channels, and are capable of affecting membrane potential and cell function in certain neurons with specific properties. When exposed to light of a particular wavelength, these light sensitive ion channels open, allowing ion currents to flow. Thus, activity of such neurons can be manipulated with light on a precise timescale [38]. Figure 1.4 shows the main difference between electrical stimulation and optogenetics. As already mentioned, generated electrical field affects the neurons in a very broad manner, and it is impossible to achieve precise stimulation of preferably individual single cells. On the other side, optogenetics offers the possibility of stimulation genetically targeted specific neurons, without affecting the rest of the neurons in the area.

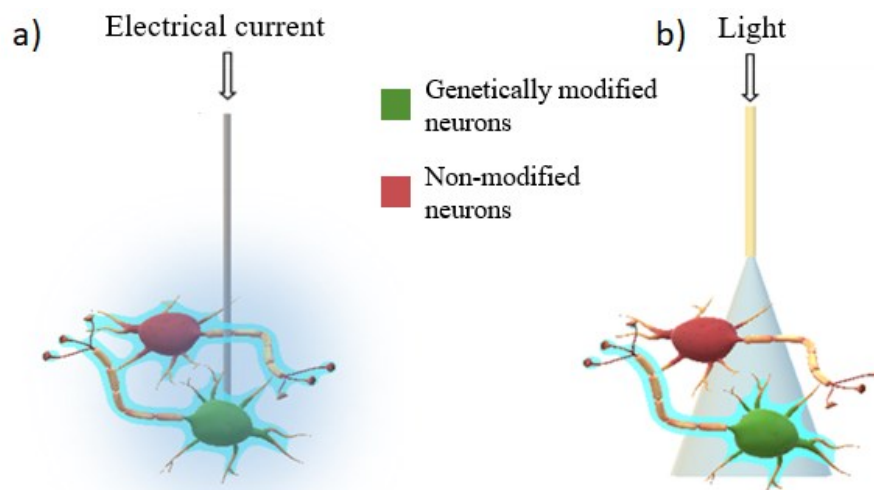


**Figure 1.4:** Difference between effects of electrical and optical stimulation on a brain region with multiple neuron types (red and green colors). Activated neurons are outlined in blue. Deep brain electrical stimulation (a) affects all neurons surrounding the electrode, while light delivered through the optical fiber (b) targets only a specific subpopulation of neurons which are genetically modified to be light-sensitive to a particular wavelength.

A very early application of optical neural stimulation was conducted in 1971 [39]. For the first time high-power blue laser light was used to accomplish targeted neural stimulation which resulted in excitation of the action potentials in Aplysia ganglia. Discovery of a light-sensitive ion channel channelrhodopsin-2 (ChR2) in 2003 [40] followed by the discovery of an optically activated chloride pump, halorhodopsin (NpHR), and a proton pump, Archaeorhodopsin (ArCh)

[41] provided new possibilities for the optical neural stimulation. Opsin genes are divided into two distinct super families: microbial opsin (type I) and animal opsin (type II) [42], and they both belong to major class of light-sensitive protein which consists of 7-transmembrane rhodopsin. Microbial opsin (Type I) induce a trans-membrane ion flux when activated with light. The optical activation leads to a change of resting membrane potential and, dependent on which kind of ion flow was induced (cationic or anionic, into or out of the cell), the cell is excited or inhibited [37]. Opsin type II allow optically controlled biochemical signaling even in non-excitabile cells. Viral vectors are mostly used to introduce the opsins into neural tissue (targeting), and the type of a virus determines the spreading area of transduced neurons [43].

Neuron that expresses these light-sensitive opsins can be depolarized (for neural excitation) or hyperpolarized (for neural inhibition) by visible light at appropriate wavelengths with millisecond temporal accuracy [44]. Multiple opsins can be expressed in a single cell so that the same cell can be selectively excited or inhibited with the corresponding light wavelength [45–47]. ChR2 which enable neurons with specific behavior (up-regulates neural activity) is switched on by blue light ( $\sim 470$  nm), while NpHR, which can silence neurons for a particular action (down-regulates neural activity) is switched on by yellow light ( $\sim 570$  nm) [48]. Thus, neurons can instantly be switched from activation to inhibition or *vice versa* by changing the light wavelength (blue or yellow) [38]. The capability to activate certain neurons while inhibiting others at the same time is a prominent aspect of optogenetics. Many light-sensitive proteins, bio-engineered to control brain activity, were developed in the last decade. Most of them are activated by blue light (like ChR2), but nowadays light-sensitive proteins absorption spectra covers much of the visible spectrum.

Integration of optics and genetics opens a new door for neural prosthesis application. In the past decade scientists focused on development of light-gated microbial opsins [43, 44, 49, 50]. Recent advance of highly sensitive ChR2 and NpHR makes relatively low-intensity optical neuro-modulation possible [50, 51]. According to the latest studies, the radiant flux density required for activation of ChR2 and NpHR is  $1 \text{ mW/mm}^2$  and  $7 \text{ mW/mm}^2$  respectively. This improvements opened a new possibilities for neuroscientists to study Parkinson's disease [52], epilepsy [53], brain mapping [54], retinal prosthesis [55], and depression [56]. Over the past decade, a lot of research has been carried out in an attempt to design optogenetic devices that would perform simultaneous light delivery and electrophysiological recording, while being minimally invasive. Such device consist of implanted light source, or implanted light guiding structure (optical fiber or waveguide) connected to external light source, and a single or multiple microelectrodes.

Light absorption leads to tissue heating, which represents a big concern in each optogenetic experiment. Beside the possibility of tissue damage, heat-induced neuronal activation, that leads to a non-targeted neuron stimulation, is also possible [57, 58]. Approximately 30% increase in firing rates of the neurons that do not express any opsin was observed during light stimulation (532 nm) with commonly used radiant flux of  $5 \text{ mW}$  [57]. It has been demonstrated that, proportionally to radiant flux density, any light absorption in neural tissue leads to a heat generation and its dissipation into the outlying non-illuminated tissue by a combination of heat convection and diffusion [59]. However, since absorption coefficients are wavelength dependent and are approximately ten times higher for 475 nm than 630 nm, heating effect also depends on a wavelength used in optogenetic experiment [60]. A number of research studies [57, 58, 61, 62] have shown that continuous brain illumination with a radiant flux of  $10 \text{ mW}$  increases a temperature for  $1\text{--}4^\circ\text{C}$  across a large volume of tissue, which is sufficient to induce

physiological and behavioral changes, alter blood flow, and to cause a local neuronal firing rates. Tissue heating can be reduced by carefully choosing the size of light delivery tool and a wavelength of light used for stimulation.

The experimental potential of optogenetics is demonstrated by its extensive application in neuroscience. Beside the extensive use in research focused on revealing information about brain function (e.g., investigation of sleep and wakefulness [63], mapping of the motor cortex [64], information processing [65], study of cognition and behavior [66], the role of the hypothalamus in aggression [67]) [37], optogenetics is also applied as an approach for pathological brain investigation including Parkinson's disease [52, 68], psychiatric disorders [69, 70], and epilepsy [71, 72]. Furthermore, optogenetic approach is also involved in cardiac research [73], and optical control of spinal cord [74]. The ideas for future application of optogenetics in therapies for humans with including retinal prostheses [55], restoration of hearing [75, 76], and even a stroke recovery [77] is widespread. However, the fact that target cells have to be genetically altered points the necessity of long-term investigations to realize and verify the full impact of optogenetics [37].

### 1.2.1 Light delivery tools

Light source usually determines optrode functionality, and thus represents the most important part of any optogenetic device. Various approaches for integration of a light source on optogenetic device will be presented in next section.

#### **Light sources**

Selection of a light source and light delivery method depends on requirements of a particular optogenetic experiment. Depending on stimulation requirements, light source has to deliver appropriate parameters that are not affected by its position in respect to the tissue of interest (wavelength, waveform, frequency, and amplitude). However, light intensity delivered to the particular tissue volume is strongly influenced by the position of implanted light source or delivery site of a light guiding structure in relation to that volume. In very rare scenarios, when the wavelength required for neural stimulation is such that attenuation in tissue allows the light to reach non-superficial targets, light sources can be placed on top of the tissue directly illuminating it. This non-invasive approach is mostly used for peripheral nervous stimulation, while in case of brain stimulation, at least the skull has to be removed in order to obtain sufficiently high light intensities for optogenetic stimulation [37]. Furthermore, sufficiently high power (more than  $11 \text{ mW/mm}^2$ ) could be obtained at the brain surface illuminated with light emitting diodes (LEDs) [78, 79].

In first *in vitro* optogenetic experiment, light emitted from a xenon lamp (300 W) was filtered to blue (450-490 nm) and with a microscope objective focused on cells expressing ChR2 opsin [37, 44]. Such broadband light sources (xenon, halogen, mercury arc lamps) are mostly used in *in vitro* optogenetic studies for investigation of cell structures and brain slices, and they usually require appropriate narrowband spectral filters in order to deliver the light of an adequate wavelength for opsin activation.

More often, light sources such as LEDs or laser diodes (LDs), with a narrow spectrum are used. Beside the fact that they are compact and portable, they also allow simple coupling of glass fibers by FC/PC connectors which enables light guiding to the target tissue. Due to their simpler



structure and more robust performance compared to LDs, LEDs are the most used light delivery sources in optogenetics [80]. Compared to LEDs, that have a lambertian emission profile of non-coherent light with a coupling limited only to a multimode optical fibers and waveguides, LDs have a much narrower spectral width (Gaussian) and can be coupled to both, single mode and multimode optical fibers and waveguides [81]. However, commercial availability limits the use of LDs as an implantable light sources in optogenetics. Compared to package size of LDs that exceeds several millimeters in diameter and length [37], LED packages are commercially widely available in the millimeter and sub-millimeter range. In *ex vivo* optogenetic experiments, LEDs are usually assembled in arrays [82].

When an in depth stimulation is required, depending on stimulation requirements, light source can be either implanted or external (coupled to an implanted light guiding structure). However, when it comes to light source implantation, the options for light sources become very restricted. Size and weight, power supply, and heating of the light source have to be minimized while maintaining adequate light intensities [37]. Low in weight and very small light sources are good candidates for integration on implantable substrate. A size reduction is mostly followed by power reduction, thus in some optogenetic experiments an effective coupling between an implantable light guiding structure and external light source is required in order to deliver the light with sufficient power to the targeted volume. In these cases, most common external light sources are fiber coupled LDs or LEDs.

Beside the weight and size requirements, an implantable light source has to be protected from the aqueous body environment, which makes it easier to place the light source on the extracorporeal part of the optogenetic device. This approach leads to development of a portable, in some cases wireless, light delivery tools with implantable light guiding structure (optical fiber or waveguide) coupled to external light source placed on outer (not implantable) part of the optrode. A good example of implantable light source for optogenetic stimulation consists of micro LED ( $\mu$ LED) array integrated on an implantable probe [83]. Furthermore, optical cochlear implant (oCI) for hearing restoration represents a non-invasive approach for light stimulation of genetically modified cochlear neurons, consisting of around hundred  $\mu$ LEDs integrated on a curved flexible substrate and implanted in a cochlear spiral-shaped cavity [84, 85].

### Optical fibers and waveguides

In a situation when light source implantation is not possible, light guiding to a distant site (located deep in a tissue) is achieved using optical fibers and waveguides coupled with external light source. Both, optical fibers and waveguides, are typically composed of at least two phases, the core, guiding the light, and the surrounding cladding, ensuring that the light is trapped in the core due to total internal reflection. Therefore, the refractive index of the core ( $n_{co}$ ) has to be higher than the one of cladding ( $n_{cl}$ ). The angle of the light cone coupled in or out of the optical fiber or waveguide is defined by the value of numerical aperture (NA), influenced by the difference in the refractive indices of core and cladding. Light power delivered to a distant site depends on light scattering and absorption inside optical fibers and waveguides, as well as on losses arising from light coupling between external light source and optical fiber or waveguide.

A distinction is drawn between single-mode and multimode optical fibers and waveguides. A small core diameter ( $2\mu\text{m}$ - $10\mu\text{m}$ ) and a slight difference between refractive indexes of core and cladding, which leads to a very small NA (0.10 - 0.2) are characteristics of single-mode optical

fibers and waveguides. Multimode waveguides and fibers have a large core diameter (10 $\mu\text{m}$  -1500 $\mu\text{m}$ ), and a larger NA (0.2 - 0.5) which makes light coupling easier, but with reduced signal quality. Since the optogenetic application doesn't depend on dispersion and the beam profile quality, while the high importance is given to effective light coupling, multimode optical fibers and waveguides are widely used as light delivery tools in optogenetic experiments [37].

Because of their excellent light guiding, with losses smaller than 0,2 dB/km, glass fibers are very suitable for optogenetic application [37], and until now they are used in most optogenetic studies. Without compromising the movement, glass fibers with diameters up to 300  $\mu\text{m}$  for mice and up to 400  $\mu\text{m}$  in rats can be implanted [86]. Since the very thin glass fibers are not suitable for standalone insertion, due to their brittleness, typical glass fiber diameters used in optogenetic application range from 125  $\mu\text{m}$  to 400  $\mu\text{m}$  [20, 86, 87].

Although optogenetic techniques have lately improved, a widely used optrodes in neuroscience labs are still based on flat cleaved optical fibers [20, 88–94]. Beside the fact that the geometric profile of flat cleaved fibers substantially damages tissue and, in the tissue, induces glial activation around the device even long after the implantation [95–97], this widely used approach also encounters important limitations when it comes to illumination within the tissue of interest. Since the spatial extent of illumination within the neural tissue cannot be controlled and adjusted using flat cleaved fibers, a precise spatiotemporal control of neural processes, which is a main goal of optogenetics, is very difficult to achieve.

Compared to flat cleaved fibers, that offer a spatially heterogeneous illumination in a relatively small and fixed brain volume near the fiber facet, optical fibers with tapered tips can be used for illumination of spatially restricted or large brain volume (Figure 1.5). In addition to being less invasive than flat cleaved fibers, tapered fibers offer a great advantage for *in vivo* control of neural activity in different animal models. Recently, the application of a tapered fiber based optrode provided a wide-volume illumination in the motor cortex and in the striatum of both free-moving and head restrained mice [96], as well as in the Frontal Eye Field of nonhuman primates [98]. The main characteristic of the tapered fiber tips is the cone angle and it determines the light delivery pattern, which will be discussed in more details in this thesis.

When a different requirements on the device, such as mechanical properties, geometry, or a necessity of light delivery to multiple sites are of higher importance, a variety of materials can be used to act as a waveguide. However, it is unlikely to reach the extraordinarily good light guidance capability like in case of glass fibers. Silicon-based waveguides, consisting of 0.2 to 9  $\mu\text{m}$  thick and 28  $\mu\text{m}$  wide core made from silicon nitride ( $\text{Si}_x\text{N}_y$ ) or silicon oxy-nitride ( $\text{SiO}_x\text{N}_y$ ) with tunable refractive index and silicon oxide as a cladding material, have been integrated on a silicon shanks in form of one or multiple waveguides [99–102]. Large thickness variations of waveguide dimensions can be achieved in waveguides with polymer core usually made of negative photoresist SU-8, and a cladding made of silicon dioxide or borosilicate glass [37]. These waveguides, structured to deliver the light to multiple sites, are mostly integrated on either silicon-based [103–105], or polyimide-based substrates [106]. Compared to a silicon-based waveguides (propagation losses of 3.1 dB/cm for  $\text{SiO}_x\text{N}_y$  core 20 x 9  $\mu\text{m}^2$  [99]), SU-8 waveguides of the same size have considerably higher propagation losses (6.4 dB/cm [103, 106]) at 470 nm.

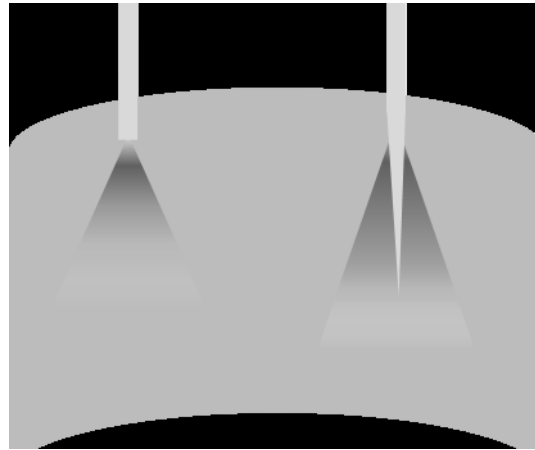


*Figure 1.5: Schematic representation of a difference in light delivery through flat and tapered optical fibers.*

### 1.2.2 Optrodes

To achieve light delivery, and to perform simultaneous electrophysiological recording from the nervous system, scientists and engineers designed dual optical and electrical probes. The combination of optical and electrical elements in one single probe represents the device called optrode. In such optrodes light is mostly delivered through flat or cleaved optical fiber or waveguide, while electrophysiological recording is obtained with assembled wire microelectrodes or conductive coatings. A common practice in such devices is to integrate a discrete light source (LD or LED) on an implantable substrate, but not on penetrating part, making sure that a sufficiently good coupling to a light-guiding structure (waveguide or optical fiber) is achieved. This approach enables fabrication of wireless optrodes. However, there are still approaches that rely on external fiber-coupled light source for light delivery to an implantable waveguide or optical fiber. A sufficiently good coupling between the optical fiber, connected to the external light source, and an implantable fiber or waveguide is crucial to ensure that a required light power is delivered to stimulation sites. Optrodes with implantable light sources, that don't require a light guiding structure, are becoming very popular.

Recording electrodes have to be positioned in a defined distance to the light-emitting sites to enable recording from the light-activated neurons. Single microelectrode, as well as bundles of microelectrodes (for example tetrodes) are usually assembled with one or multiple optical fibers in fiber-based optrodes, while metal coatings, deposited on the implantable substrate, are often used in waveguide-based optrodes. Different assemblies of light delivery and electrical recording sites led to development of various optrodes with variety of stimulation and recording possibilities.

To be applicable in optogenetic experiments, an optrode has to meet critical requirements such as: biocompatibility, minimal invasiveness, and low tissue heating. In order to avoid inflammation reactions, implanted optrode must be biocompatible with the tissue. Providing protection of optical and electronic components from the moist environment, as well as from the salts and enzymes is essential to ensure the longevity of the implanted optrode. Packaging and coating approaches depend on the optrode design, and they are mostly realized through the application of biocompatible polymers, glasses, and ceramics.

In order to meet the requirements for activation of the target tissue volume containing genetically modified neurons, optrode has to provide a sufficient light power. Beside the

parameters that can be controlled with the light source (wavelength and input light intensity), for the successful optogenetic experiment, one needs to obtain the change in radiant flux density and the spatial distribution with distance from the implanted light delivery site. Optical properties of the medium strongly affect the distribution and change in radiant flux. Therefore, light power measured at a certain distance in air is dramatically different from the power value measured at the same distance in tissue where light distribution from the source is dictated by wavelength-dependent scattering and absorption. Furthermore, tissue optical properties can also vary between different regions. In case of targeting a small tissue volume, light power is not the limiting factor. However, as the tissue volume increases, the peak light power required to achieve efficient activation 100  $\mu\text{m}$  or more away from the center of illumination can become a limiting factor, especially when using flat-cleaved optical fibers [60].

To achieve necessary irradiance at membrane of opsin-expressing neuron in optogenetic experiment, spectral flux density emitted from optical fiber or waveguide has to be estimated. As a light beam travels through a medium, its radiant flux density is attenuated by absorption and redistributed by scattering. Light propagation in a turbid medium such as neural tissue is strongly affected by both of these phenomena [107, 108]. According to estimation based on a presence of small blood vessels in the brain tissue, light absorption leads to spectral flux density attenuation ranging from 60% (in striatum) to 86% (in olfactory bulb) within 1mm depth in case of ChR2 excitation wavelength (470 nm) [60]. Moreover, the dramatic light attenuation would occur if a large blood vessel passes through beam path [109]. In addition, coagulated blood around an optical implant can strongly absorb applied light. Since particles of various sizes, ranging from phospholipids of cell membranes over cellular organelles like mitochondria to entire cell bodies, are present in tissue, beside absorption, light scattering also takes place, and it is responsible for a change in photon's direction, causing light beam to disperse leading to reduction in radiant flux density [110].

Prior to fabrication, Monte-Carlo-based simulations are often used to predict the optical performance of the optrode. Absorption and scattering coefficients, as well as tissue refractive index represent wavelength-dependent tissue properties that are used as an input parameters for simulation. Prior estimation of overall optrode performance enables time saving and fabrication of a functional device.

### **Optrodes with integrated light sources**

If the light source is integrated on a penetrating part (implanted in a tissue) of a substrate, there is no need for light guiding structure (optical fiber or waveguide). To minimize invasiveness and reduce tissue damage, size of implantable light sources has to be reduced as much as possible. An example of such optrode consists of four  $\mu\text{LEDs}$  (450 nm) that can be activated independently, and a platinum microelectrode with active area of  $400 \mu\text{m}^2$  (Figure 1.6 a) [83]. Due to a very small size of each  $\mu\text{LED}$  ( $50 \times 50 \times 6.4 \mu\text{m}^3$ ) four of them in linear array were required to achieve output overall flux density of  $28 \text{ mW}/\text{mm}^2$  at the surface of  $\mu\text{LEDs}$ . In order to achieve a sufficient flux density ( $1 \text{ mW}/\text{mm}^2$  at the  $\mu\text{LED}$  surface) from even smaller implanted  $\mu\text{LEDs}$  ( $10 \times 15 \times 0.5 \mu\text{m}^3$ ), four shank probe with 12 integrated  $\mu\text{LEDs}$  and 32 recording sites was fabricated on silicon substrate (Figure 1.6 b) [111].

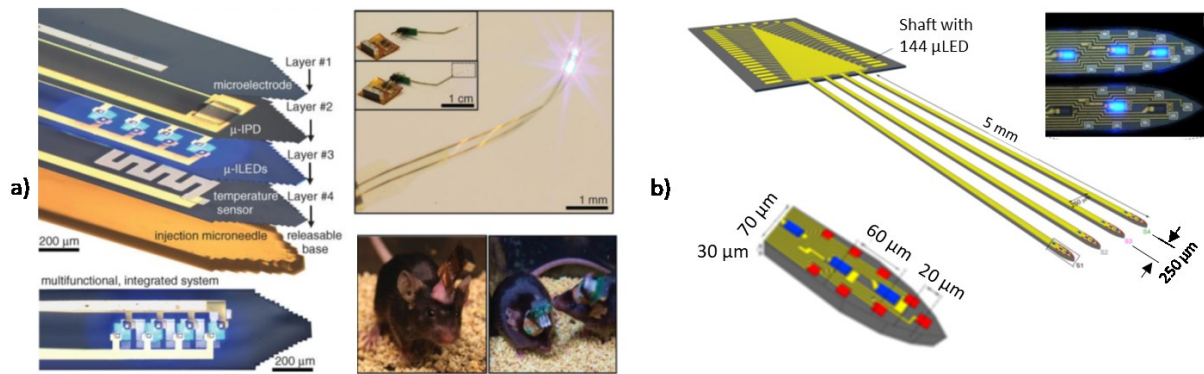


**Figure 1.6:** Examples of optrodes with implantable light sources: a) optrode containing 4 implantable GaN  $\mu$ LEDs integrated on a substrate, and a platinum microelectrode with active area of  $400 \mu\text{m}^2$ , image adapted from [83], b) four shank probe with 12 integrated implantable InGaN  $\mu$ LEDs and 32 electrical recording sites, image adapted from [111].

Another example of such device represents an optical cochlear implant (oCI) (Figure 1.7). This type of implant, based on electrical stimulation, exists for a long time and represents the most successful neuroprosthetic device with more than 400.000 implanted systems [112]. Implanted in human cochlea, and used to electrically stimulate spiral ganglion neurons, this device is proved to partially restore hearing. Furthermore, when implanted in very young age (6 months) helps with early development of hearing and speaking capabilities [113]. Despite all the advantages in hearing restoration, patients mostly encounter the main drawback of such CIs, which is the limited frequency resolution due to wide current spread [84, 114]. Although modern CIs have been improved in terms of frequency resolution, offering patients a reasonable comprehension of speech, individuals with good result in hearing restoration are rarely able to conduct conversation in noisy environment or to enjoy the music [84]. Optogenetics offers a promising approach to overcome above described limitations of classical CI based on electrical stimulation [115].

Cochlear implants for optical stimulation, promising neural stimulation with improved spatial resolution, consist of linear arrays of  $\mu$ LEDs integrated on bendable probe allowing implantation in curved cochlear cavity. An example of such oCI consisting of  $380 \mu\text{m}$  wide and  $15 \mu\text{m}$  thick highly flexible polyimide substrate comprising a linear array of 15  $\mu$ LED chips ( $150 \times 150 \mu\text{m}^2$  emission area) controlled in groups of five [116] (Figure 1.7 a). An attempt to increase number of light delivery sites (from 15 to 140) and to improve thermo mechanical behavior of implantable device by replacing polyimide substrate with an epoxy layer, led to development of novel more flexible oCI [84] (Figure 1.7 b).

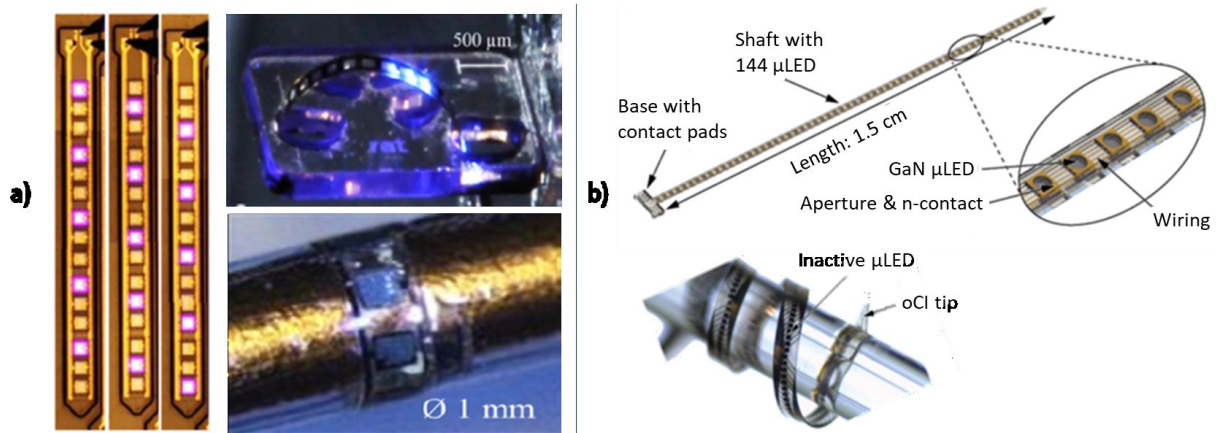


**Figure 1.7:** Examples of optical cochlear implants (oCI) a) 380µm-wide probe comprising  $3 \times 5$  LEDs with  $150 \times 150 \mu\text{m}^2$  emission area, image adapted from [116] b) Schematic of the oCI probe base carrying contact pads and a 1.5 cm long shaft comprising 144 µLEDs, image adapted from [84].

### Waveguide-based optrodes

When a simultaneous light delivery to different stimulation sites is required, integration of waveguides into an optrode is the most common approach. Polymer waveguides can be fabricated with very small dimensions, similar to those of glass fibers, enabling good coupling to a light source. As they often come along with high propagation losses, it is beneficial to ensure that coupling to a light source is as close as possible to targeted tissue volume. Since in most optrodes waveguides are integrated on stiff substrate (mostly silicone), their main advantage of being flexible and hence reducing the invasiveness is rarely used [37].

A multi-waveguide optrode, fabricated in the form of a 360 µm wide array of 12 parallel rectangular (20 µm wide and 9 µm thick) silicon oxy-nitride (SiON) multimode waveguides on silicon substrate, capable of independently delivering light to multiple targets along the probe axis is presented on Figure 1.8 (a) [99]. Using a standard micro-fabrication techniques, rectangular cores were coated with 3µm thick SiO<sub>2</sub> cladding. Furthermore, each waveguide can be independently coupled to a light source, enabling control of light delivery to various stimulation sites, resulting in 33% of the input source optical power delivered to a stimulation site. Aluminum corner mirrors are integrated at the end of each waveguide enabling efficient light deflection away from the probe axis. However, recording electrodes are not integrated in this design, and they should be separately implanted in targeted tissue volume.

The requirement for tissue damage reduction led to a modification of such optrode by integrating electrical recording sites on silicon substrate. An example of such optrode design incorporates 12 miniaturized silicon nitride (SiN) waveguides (cross section of  $6 \times 12 \mu\text{m}^2$ ) placed symmetrically next to 24 titanium nitride recording micro electrodes (cross section of  $10 \times 10 \mu\text{m}^2$ ) on a narrow 100 µm wide silicone shank (Figure 1.8 b) [102]. Maximum overall output flux density was reported to be higher than 50 mW/mm<sup>2</sup>, which is above optogenetic requirements. Although this optrode design overcomes previous limitations, lack of possibility to individually couple discrete light source to each waveguide represents the major disadvantage of this device.

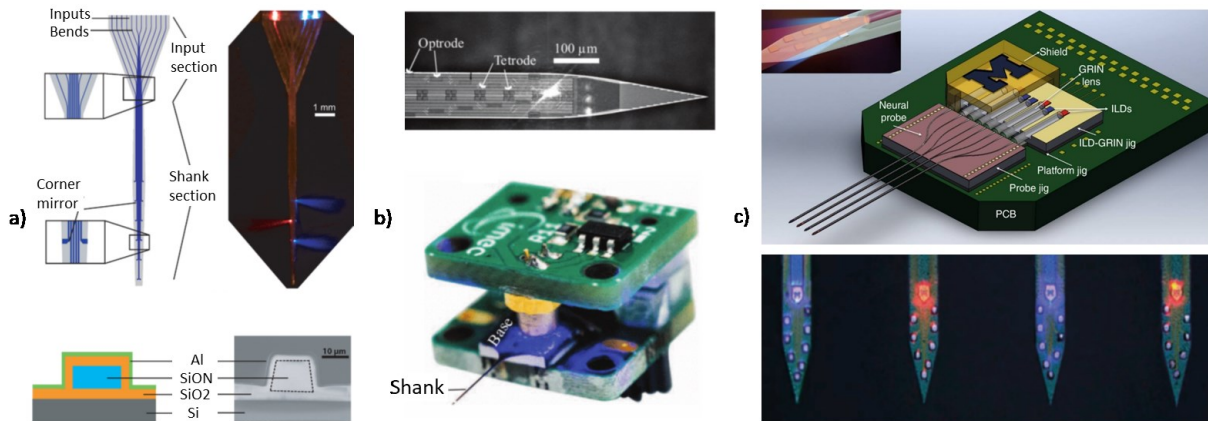


**Figure 1.8:** Examples of silicon nitride waveguide-based optrodes: a) multi-waveguide probe, consisting of 12 parallel rectangular ( $20\ \mu\text{m}$  wide and  $9\ \mu\text{m}$  thick) multimode waveguides without electrical recording sites, capable of independently delivering light to multiple targets along the probe axis, image adapted from [99], b) optrode incorporating 12 miniaturized waveguides (cross section of  $6 \times 12\ \mu\text{m}^2$ ) placed symmetrically next to 24 titanium nitride recording micro electrodes (cross section of  $10 \times 10\ \mu\text{m}^2$ ) on a narrow  $100\ \mu\text{m}$  wide silicone shank), image adapted from [102], c) four-shank multicolor optrode containing an optical mixer waveguide (cross section of  $7 \times 30\ \mu\text{m}^2$ ) and eight iridium recording sites on each shank, image adapted from ) [100, 117].

Further development of a SiN waveguide-based optrodes led to fabrication of a four-shank (each shank is  $70\ \mu\text{m}$  wide,  $22\ \mu\text{m}$  thick, with inter-shank pitch of  $300\ \mu\text{m}$ ) multicolor optrode containing an optical mixer waveguide (cross section of  $7 \times 30\ \mu\text{m}^2$ ) and eight iridium recording sites on each shank (Figure 1.8 c) [100, 117]. Coupling of compact LDs to a SiN optical mixer waveguide on a silicon probe through grade-index (GRIN) lenses allows multicolor light delivery at a common waveguide port, and thus enables multicolor modulation of the same neuronal population.

Beside waveguides with SiN core, polymer-based waveguides are also used as optrode optical components. Epoxy-based negative photoresist SU-8 is widely used as a core material for fabrication of waveguides integrated on either silicone- or polyimide-based substrates. An early approach to fabrication of a polymer waveguide-based optrode consisted of a single SU-8 core waveguide integrated on silicon shank containing 16 iridium electrodes (Figure 1.9 a) [105]. Since the light is coupled to a waveguide from an optical fiber, U-groove is formed on substrate to ensure accurate alignment and minimize coupling losses.

An idea to incorporate a fluidic channel on the polyimide shaft containing a single SU-8 waveguide, coupled to an optical fiber, and nine electrode sites led to a fabrication of an optrode that enables simultaneous light delivery, electrical recording and genetic modification of neural cells by gene delivery vector through microfluidic channel (Figure 1.9 b) [106]. Even though these single waveguide-based optrodes were reported to deliver the light power sufficient for optogenetic stimulation, they cannot be used for stimulation at multiple sites. In order to overcome this limitation, multi-shank optrode was fabricated using standard Micro-electro-mechanical system (MEMS) fabrication procedure.

Simultaneous optical stimulation of different tissue regions can be achieved by integrating SU-8 based waveguides on multi-shank array. Such optrode was fabricated containing four shanks (each  $86\text{-}\mu\text{m}$  wide and  $30\text{-}\mu\text{m}$  thick) of different length (from 3 to 6 mm), each containing a single SU-8 core waveguide ( $20\ \mu\text{m}$  wide,  $15\ \mu\text{m}$  thick) for light delivery and eight microelectrodes for electrophysiological recording (Figure 1.9 c) [103]. Multiple Y-shaped

optical splitters are also integrated on a substrate to guide light from optical fiber to multiple stimulation sites.

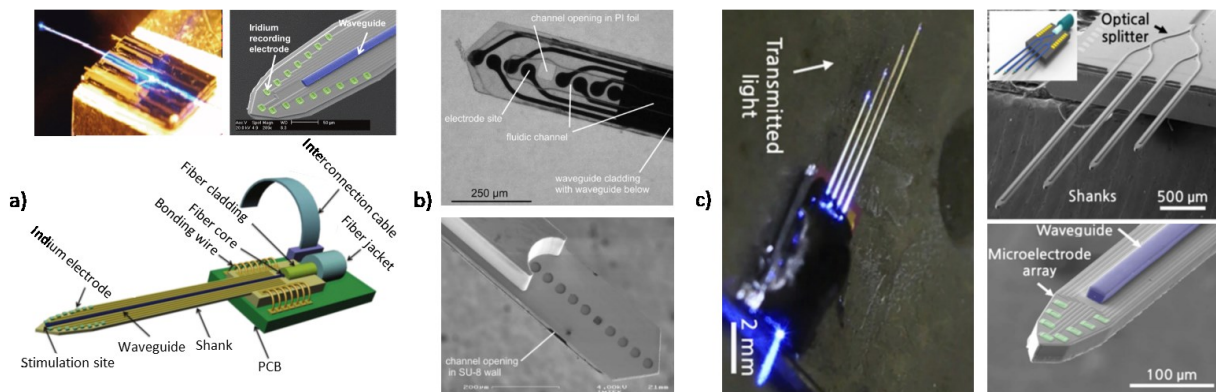


**Figure 1.9:** Examples of polymer waveguide-based optrodes: a) single waveguide with SU-8 core integrated on silicon shank containing 16 iridium electrodes, image adapted from [105]., b) optrode with a single SU-8 waveguide integrated on a polyimide shaft together with nine recording electrodes and microfluidic channel, enabling simultaneous light delivery, electrical recording and genetic modification of neural cells, image adapted from [106], c) four shank waveguide-based optrode with a single SU-8 core waveguide on each shaft for light delivery and eight microelectrodes for electrophysiological recording, image adapted from [103].

### Fiber-based optrodes

An early approach to fiber-based optrode represents a simple combination of commercial optical fiber ( $\sim 200\ \mu\text{m}$  outer diameter) and commercial tungsten microelectrode ( $\sim 125\ \mu\text{m}$ ) [52, 118]. In this approach, a microelectrode was glued to a flat cleaved optical fiber and used as an implantable probe (Figure 1.10 a) [118]. This kind of optrode is very often used in *in vivo* experiments for simultaneous light delivery and electrical read out [119–122]. More sophisticated design incorporates multiple light delivery and electrical recording sites in different assemblies, such as presence of multiple optical fibers, each glued to a bundle of four microelectrodes (Figure 1.10 b) [123], or a combination of multiple separated optical fibers and microelectrodes in one optrode (Figure 1.10 c) [124]. The recent modification of previous design is presented as an optrode with flat cleaved optical fiber ( $\sim 200\ \mu\text{m}$  outer diameter) in the centre, surrounded with eight tetrodes (Figure 1.10 d) [94].

Previously described optrode designs represent only a few examples of a numerous existing approaches based on the same idea of incorporating a single or multiple light delivery and recording sights in various assemblies. Therefore, all of these devices can be categorized as a multi-tip optrodes, and their invasiveness during the insertion into a brain tissue depends on a size and geometry of implantable tips. Use of a tapered optical fibers as a light delivery tool, and a metal coating as a microelectrode minimizes the tissue damage, while maintaining the optrode functionality. However, so far there were only a few attempts to fabricate such fiber-based one-tip optrode consisting of a single tapered whole or half gold-coated optical fiber [86, 125]. This approach would drastically minimize the tissue damage and offer a reliable light delivery as well as electrical read out. For an optimized optogenetic setup, light source must be chosen carefully, taking into a count the irradiance profile that rises from the fiber tip geometry. Optical fiber can be coupled to LED or LD, depending on the light stimulation needs, and all the components in the light path, that are likely to induce optical losses, must be considered when choosing the optimal output power. Furthermore, fiber diameter is also a key parameter



for minimizing tissue damage during the optrode insertion, since it was demonstrated [126] that fibers with a diameter larger than 300  $\mu\text{m}$  can cause excessive neuronal loss. However, simulation studies [57] reported increased tissue heating near the fiber tip, which leads to a conclusion that a compromise between the possible mechanical and thermal tissue damage has to be found.

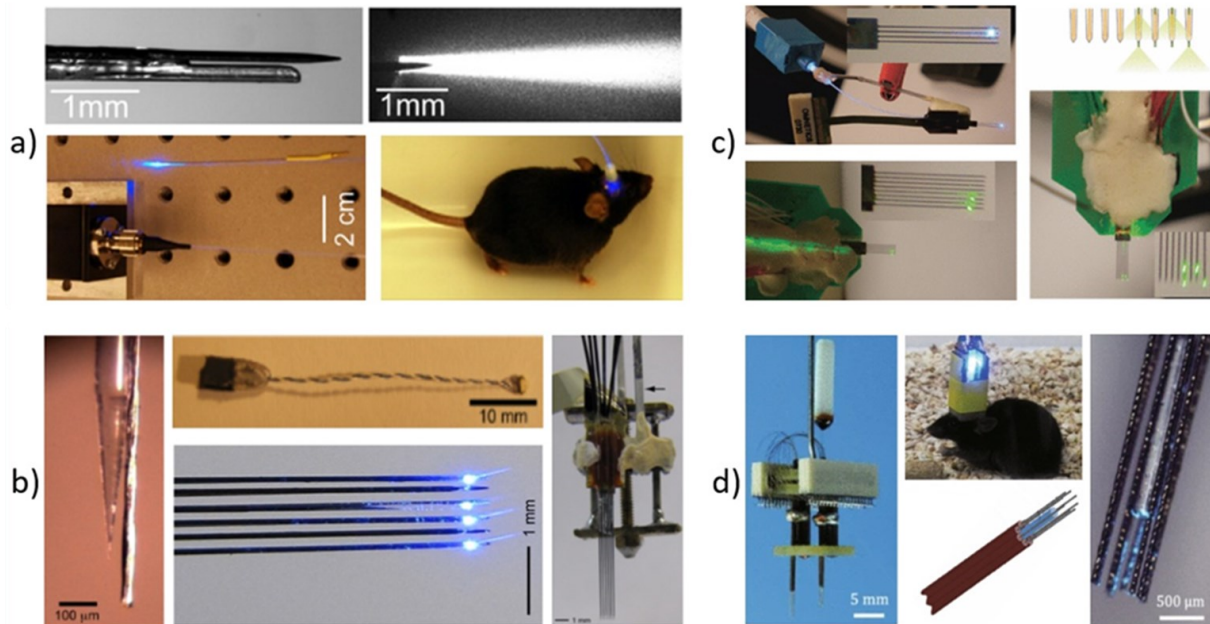


**Figure 1.10:** Various optrode designs: a) optrode made by simple gluing of the flat cleaved optical fiber and tungsten microelectrode, image adapted from [118], b) tetraode-based optrode consisting of multiple tapered optical fibers, each glued to a bundle of four microelectrodes (tetraodes), image adapted from [123], c) combination of multiple separated optical fibers and microelectrodes in one optrode, image adapted from [124], d) optrode incorporating a single flat cleaved optical fiber surrounded by eight tetraodes, image adapted from [94].

### Micro electrode optrode arrays (MEOAs)

Inspired by UEA (Figure 1.2), engineers developed 3D optrode arrays containing together assembled light delivery tools and multi electrode arrays (MEAs). An early approach to such device represents modification of well-known UEA containing three-dimensional multi electrode array (100 electrodes) made of 10 x 10 grid of 1 mm long tapered microelectrodes integrated on 0.2 mm thick silicon substrate with inter-electrode distance of 400  $\mu\text{m}$  [86] (Figure 1.11 a). With help of ablative laser machining and drilling tools, hole (diameter of approximately 203  $\mu\text{m}$ ) was created on silicon substrate in the center of UEA, which resulted in removing one of microelectrodes in 3D array. Tapered optical fiber, with tip aligned in plane with tips of microelectrodes, was mechanically fixed through that hole with UV curable epoxy. Another example of such device consists of 6x6 multi-electrode array with one electrode being replaced by gold coated tapered optical fiber [127] (Figure 1.11 b). Compared to previous device, optical fiber is not positioned in the middle of silicon substrate.

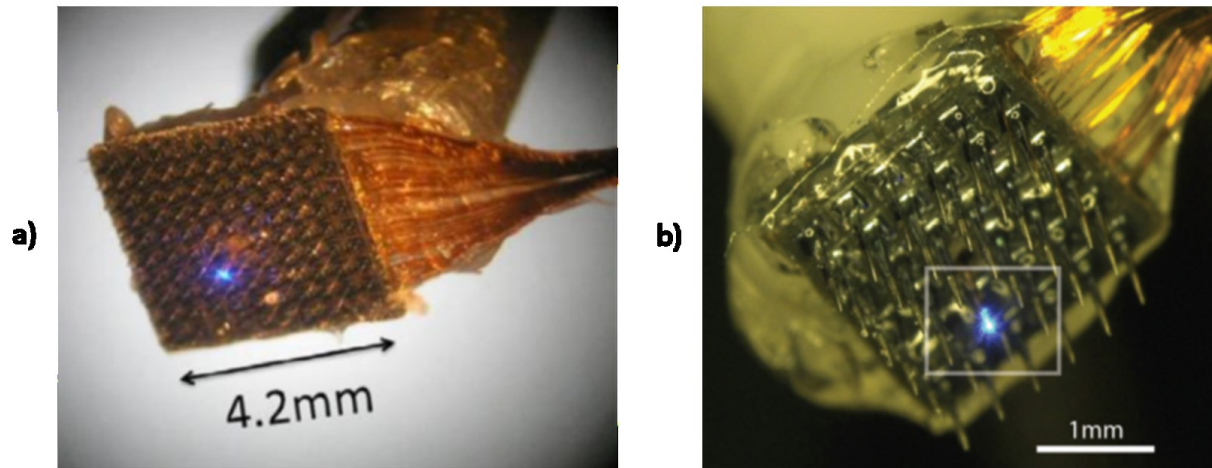


**Figure 1.11:** Examples of optrode-MEA device. a) Optrode coupled to MEA through a laser drilled hole, replacing one of the silicon microelectrodes, image adapted from [86], b) Image of the  $6 \times 6$  multi-electrode array device with one element being replaced by an optrode. Spacing between neighbor electrodes is  $400 \mu\text{m}$  and electrode shank length is  $1 \text{ mm}$ , image adapted from [127].

Further development of 3D optrode-MEA devices led to fabrication of novel  $8 \times 8$  multi-electrode-optrode-array (MEOA), consisting of titanium nitride (TiN) electrodes and silicon nitride (SiN) waveguides, for in vitro optogenetic application [128]. This device integrated optical stimulation array of 64 waveguide-based optrodes in rectangular  $8 \times 8$  configuration, with one microelectrode ( $60 \mu\text{m}$  diameters) next to each waveguide (Figure 1.12). To enable recording of the response of stimulated cell, distance between waveguide and electrode is kept very small (ranging from 6 to  $27 \mu\text{m}$ ). Half of the waveguides are designed such to deliver light of  $450 \text{ nm}$ , while other half delivers light of  $590 \text{ nm}$ . Those two groups, each containing 32 waveguides and 32 microelectrodes, can be controlled separately. Total output power from 32 waveguides was  $12 \mu\text{W}$ , recalculated to flux density of  $87 \text{ mW}/\text{mm}^2$ , which is more than enough for optogenetic stimulation of ChR2. It is important to mention that neither waveguides nor electrodes incorporated in this device are implantable, which makes it applicable only in experiments with cells positioned on device stimulation/recording surface.

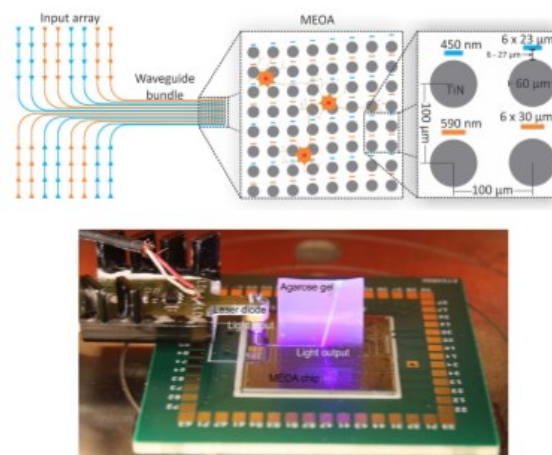


**Figure 1.12:** MEOA based device for in vitro optogenetic experiments containing optical stimulation array of 64 waveguide-based optrodes in rectangular  $8 \times 8$  configuration, with one microelectrode ( $60 \mu\text{m}$  diameters) next to each waveguide. Image adapted from [128].

First generation of glass ( $\text{SiO}_2$ ) optrode arrays of penetrating waveguides for optogenetic stimulation, fabricated by micromachining of fused silica discs is presented on Figure 1.13. The device consists of  $10 \times 10$  grid of 2 mm long glass waveguide arrays with inter-waveguide distance of  $400 \mu\text{m}$ . Glass waveguides, set upon 1 mm thick backplane, have rectangular shape with pyramidal tips [129]. This design doesn't incorporate microelectrodes, and thus can only serve for stimulation purposes. However, separate implantation of microelectrodes is always possible, and in this case would enable also electrophysiological recording from stimulated neurons. Developed procedure allows fabrication of such optrode arrays with waveguide length in range from 0.5 to 2 mm.

Different optrode designs presented in this chapter were developed to enable optical stimulation and, in most cases, simultaneous electrophysiological recording. Device size, number and shape of stimulation and recording sites, as well as degree of invasiveness differ among different approaches.

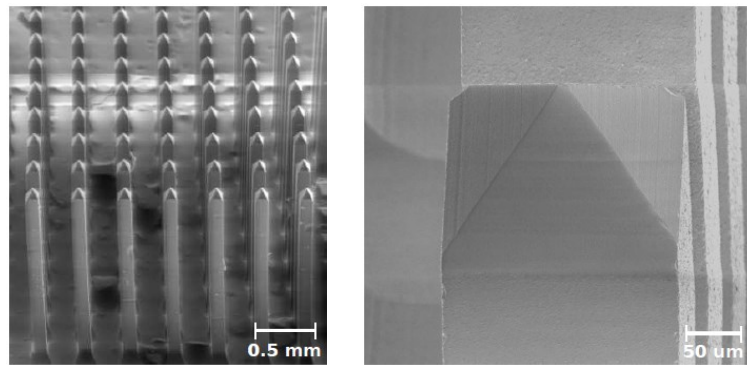


**Figure 1.13:** First generation of glass ( $\text{SiO}_2$ ) optrode arrays without recording electrodes consisting of  $10 \times 10$  grid of 2 mm long glass waveguide arrays with inter-waveguide distance of  $400 \mu\text{m}$ . Image adapted from [129].

### 1.3 Research objectives and thesis outline

Most of modern fiber-based optrodes consist of cleaved or tapered optical fiber and multiple separate micro-wire arrays (tetrodes) [93, 94, 130], which gives the possibility of light delivery and simultaneous electrophysiological recording. However they are configured as multiple – tips optrodes which can cause tissue damage during insertion.

In this thesis, a single tip fiber-based optrode is proposed as an efficient approach to minimize the tissue damage while enabling simultaneous light delivery and electrical recording. The establishment of the fabrication process, as well as the investigation of optical and electrical properties of the fabricated optrode will be presented in following chapters. Schematic illustration of the optrode concept is presented on Figure 1.14.

Single tip fiber-based optrode, fabricated in this work, consists of approximately 5 cm long tapered multimode optical fiber (FG200UEP ThorLabs) with two equidistant  $60 \mu\text{m}$  wide gold electrodes deposited along the fiber. However, optrode length can be easily reduced depending on application requirements.

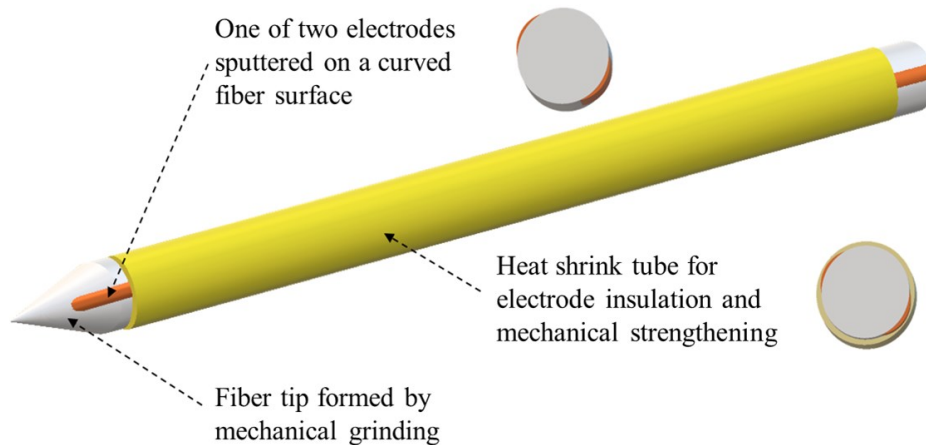


**Figure 1.14:** Schematic representation of the single tip fiber-based optrode fabricated within this project. Optrode consists of tapered optical fiber with two deposited microelectrodes on its surface. To control exposed surface of microelectrodes and also improve optrode mechanical stability, heat shrink PTFE tube is applied.

Fiber tip is formed by mechanical polishing of a flat cleaved optical fiber end using a custom made setup, developed as a part of this work, enabling the fabrication of a tapered conical fiber tip with a wide range of cone angles, thus providing a possibility of different light intensity distribution in targeted tissue. Metal electrodes are deposited on the cylindrical fiber surface through a shadow mask, aligned and fixed on custom made fiber holder. Custom made rotation and alignment setup allows angular and lateral control of the electrode position.

Insulation of a deposited electrodes is achieved through application of heat shrink tube or epoxy coating. Precise tube positioning prior to shrinking enables control of the exposed electrode region which serves as a recording site. In addition to control of exposed electrode area, heat shrink tube increases optrode flexibility and prevents fiber breaking during the insertion, as well as during the *in vivo* optogenetic experiments. Deposited electrodes are electrically connected to a printed circuit board (PCB), such that a further electrical connection required for electrophysiological recording setup can be established.

This thesis covers two main parts: (I) Establishment of a fabrication procedure for single tip fiber-based optrode and (II) Evaluation of the optical and electrical properties of the fabricated optrode. Basic principles of optical stimulation and electrical recording, as well as various up-to-date optrode designs are presented in introduction chapter.

In **Chapter 2** the focus lies on fabrication steps leading to development of fiber-based optrode consisting of cone fiber tip and two deposited microelectrodes. Custom made grinding setup for fiber tip shaping, and a precise alignment setup specially designed for electrode deposition on fiber surface are presented. Details of process steps along with occurring problems and their solutions, as well as the influence of process parameters on the final product are discussed. Furthermore, improvement of optrode mechanical performance and an approach for electrical contact establishment are also presented in this chapter. Coupling to a light source (fiber-coupled LED) represents very important part of optrode assembly, and is also presented in this chapter.

**Chapter 3** is dedicated to optical characterization of optrode performance. The effect of tip geometry on light transmission, output beam profiles and emission profiles is discussed in detail. Based on models describing light propagation in brain tissue, tissue irradiance profiles

corresponding to different cone angles of fiber tip are obtained and compared to those recorded in experiments. Analysis of intensity distribution on beam profiles at various distances from tip enables estimation of illumination volume and its comparison among tips with different cone angles.

Results of electrical resistance measurements, as well as conclusions deduced from electrochemical impedance spectroscopy are presented in **Chapter 4**. Based on these results, potential performance of optrode in electrophysiological recording is evaluated.

The results of this study, and the outlook about possible future work objectives are summarized in **Chapter 5**. Suggestions about device improvement in terms of electrical and optical performance are presented together with ideas of improved device design and performance.

## 2 OPTRODE MICROFABRICATION

Fabrication of fiber-based optrode can be described as a two-step procedure consisting of fiber tip shaping followed by electrode deposition on surface of the optical fiber. Prior to optrode fabrication, a multimode optical fiber (FG200UEP ThorLabs) with core diameter of 200  $\mu\text{m}$  and cladding thickness of 10 $\mu\text{m}$  is cut in 8 cm long pieces. In the first fabrication step, tapered fiber tip is created using a custom-made mechanical grinding setup which gives the possibility of achieving different cone angles. Deposition of two separate equidistant microelectrodes along the optical fiber, as well as on the fiber tip represents the second fabrication step which involves a physical vapour deposition (PVD) method. Details of each fabrication step, as well as a discussion about fabrication outcome are described in this chapter. Improvement of optrode mechanical performance by application of heat shrink tube or polymer coating, as well as an establishment of electrical contacts between deposited electrodes and printed circuit board (PCB) are presented at the end of this chapter.

### 2.1 Fiber tip formation

As already mentioned in Chapter 1.2.1, beside the minimal tissue damage, tapered optical fibers offer the possibility to control spatial extent of illumination within the tissue, and thus enable precise spatiotemporal control of neural processes. Fiber tips are usually tapered employing heat and pull method or chemical etching procedure. The heat and pull method is mostly used to obtain very small smooth cone angles ( $\sim 4^\circ$ ), while chemical etching allows producing reproducible fiber tips with a variety of cone angles. Compared to chemical etching, fiber tips developed using heat and pull method have a lower throughput power due to simultaneous reduction of the fiber cladding and core along the tapered region. Although chemical etching allows obtaining highly reproducible taper geometries, the sensitivity of the tip shape to environmental influences during the etching leads to large non-smooth taper angles whose rough surface causes the reflection of the guided light in the tapered region [131, 132]. In this chapter, a novel approach for development of reproducible smooth tapered fiber tips with various cone angles, using a custom made mechanical grinding setup, is presented.

#### 2.1.1 Methods

Custom made setup for fiber tip formation by mechanical grinding is presented on Figure 2.1. Grinding technique relies on the concept of synchronized spinning of the optical fiber, fixed in the fiber rotator placed on an angular stage, and a horizontal grinding disc. In order to produce fiber tips with symmetric cone, two direct current (DC) motors are used to simultaneously drive grinding disc and the fiber rotator. Controlling the driving current to DC motors enables the speed adjustment of both, grinding disc and fiber rotator. The process of fiber tip formation by mechanical grinding can be divided into three steps: positioning and alignment of the optical fiber, setting the process parameters (stage angle, rotation speed of fiber rotator and grinding disc), and starting the grinding process with subsequent grinding disc substitution.

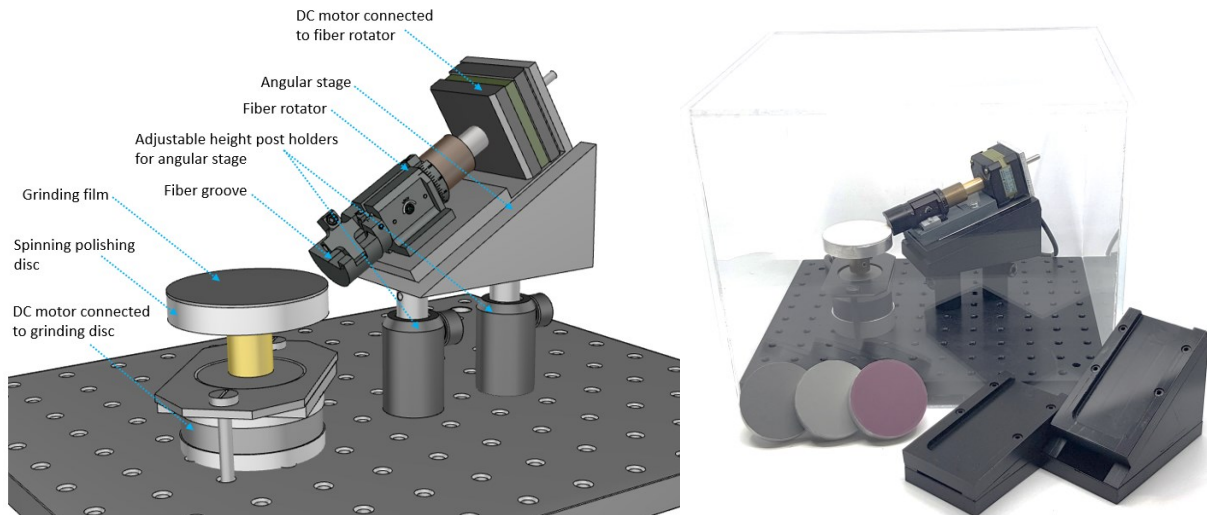


**Figure 2.1:** (Left) Schematic representation of custom made setup for fiber tip formation by mechanical grinding. The setup consists of a horizontal spinning disc with grinding film on top and a fiber rotator positioned on an angular stage; (Right) Actual image of custom made mechanical grinding setup with four exchangeable grinding discs and different angular stages.

Positioning and alignment of the optical fiber in a V-groove of fiber rotator is the first and the most important step in whole tip fabrication process. Fiber rotator (HFR007, ThorLabs), connected to a DC motor (Figure 2.2) is fixed on a horizontal metal plate which can be easily mounted on different angular stages. In addition to high-precision rotation, another important advantage of aforementioned fiber rotator is the presence of swing arm that holds the optical fiber, loaded into the rotator's V-groove, using a strong magnetic force. Incorrect alignment and positioning of optical fiber in a V-groove leads to fiber wobbling during rotation which would result in asymmetric cone tip.

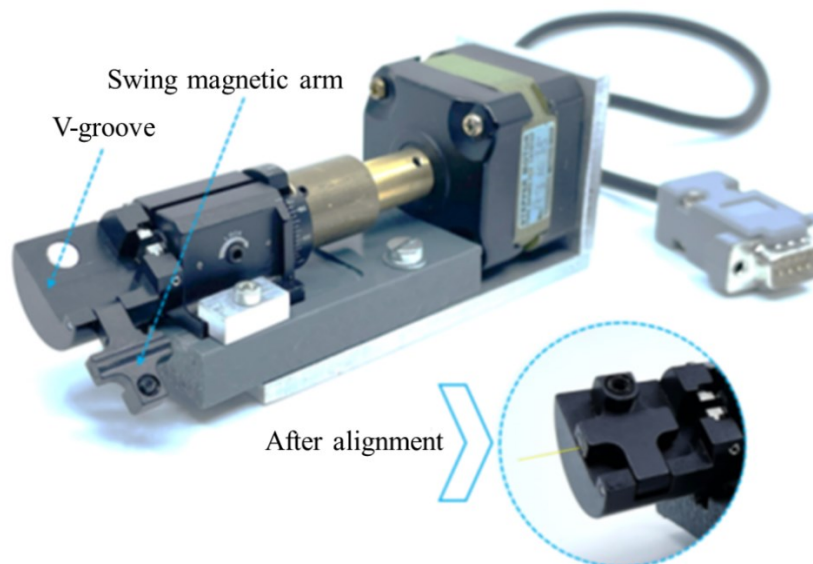


**Figure 2.2:** Fiber rotator (HFR007, ThorLabs) connected to DC motor. Optical fiber is loaded in a V-groove present on fiber holder and held by swing magnetic arm. Proper positioning of optical fiber in a V-groove of fiber rotator is crucial for formation of symmetrical cone tip.

After proper fiber placement in a V-groove, fiber rotator, connected to a DC motor and fixed on a metal plate, is mounted on an angular stage. Next, angular stage containing fiber rotator is

positioned and fixed using post holders with adjustable height (PH40, ThorLabs). During the height adjustment, digital microscope camera is used for observation of mutual position between the flat cleaved fiber end and the surface of horizontal grinding disc. This is a crucial step in fiber positioning, and the height of angular stage has to be adjusted such that the edge of flat fiber end is touching the grinding disc without bending. Fiber bending after positioning the angular stage means that too much pressure is applied which would result in fiber breaking during the grinding process. Figure 2.3 shows a moment during the grinding process of a correctly positioned optical fiber and angular stage.

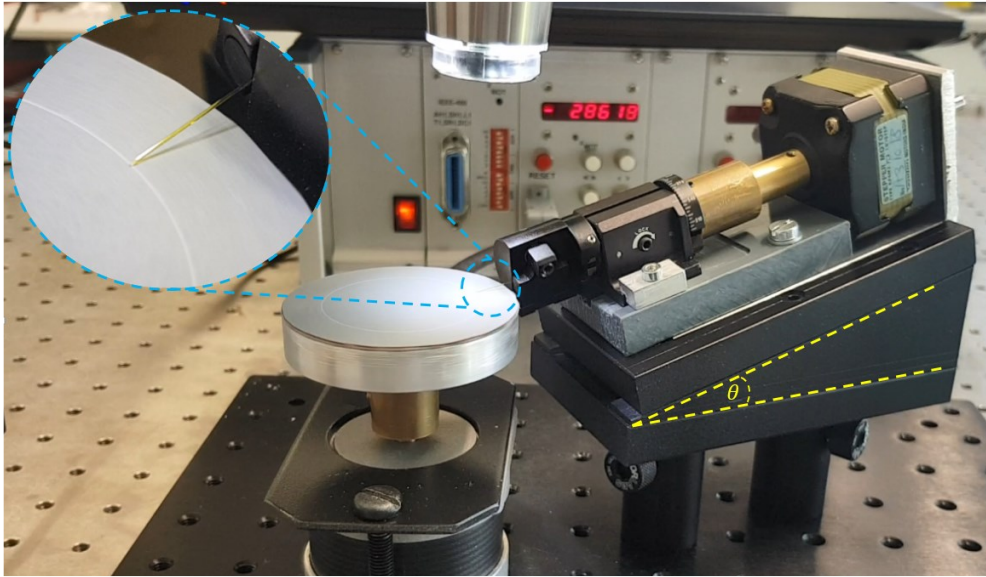


**Figure 2.3:** Grinding process of flat cleaved fiber tip. Fiber rotator placed on an angular stage. Adjustment of stage height influences mutual position of optical fiber and horizontal grinding disc.

Above described setup consists of multiple angular stages that can be easily exchanged by removing the existing and placing the new one on the post holders. This allows adjustment of the polishing angle ( $\theta$ ) between the fiber longitudinal axis and the surface of grinding disc (Figure 2.4) and enables the control of the cone angle ( $\beta$ ):

$$\beta = 2\theta \quad (2.1)$$

When first step is accomplished, meaning that fiber is properly placed in a V-groove and precisely positioned in relation to the grinding disc, process parameters have to be set. Based on many trials and errors in this work, the optimal rotation speed of grinding disc and fiber rotator is determined to be 40 rpm and 20 rpm, respectively (Figure 2.5).

To reduce time required for grinding process, one may increase the rotation speed of grinding disc and/or fiber rotator. However, a compromise between the process timing and the quality of produced fiber tips has to be made, which will be discussed later in the next section of this chapter.



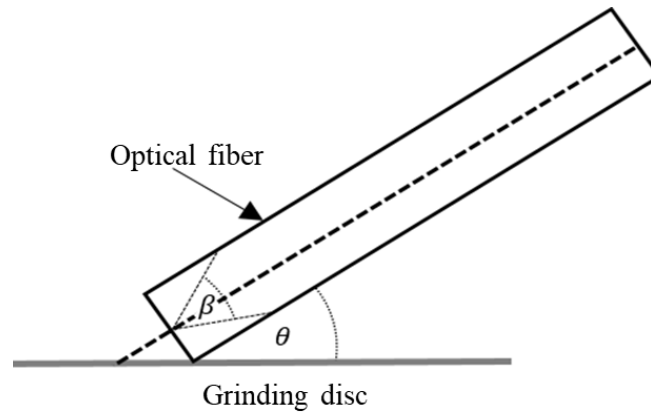


**Figure 2.4:** Mutual position of the optical fiber and horizontal grinding disc. The polishing angle ( $\theta$ ) determines the cone angle ( $\beta$ ).

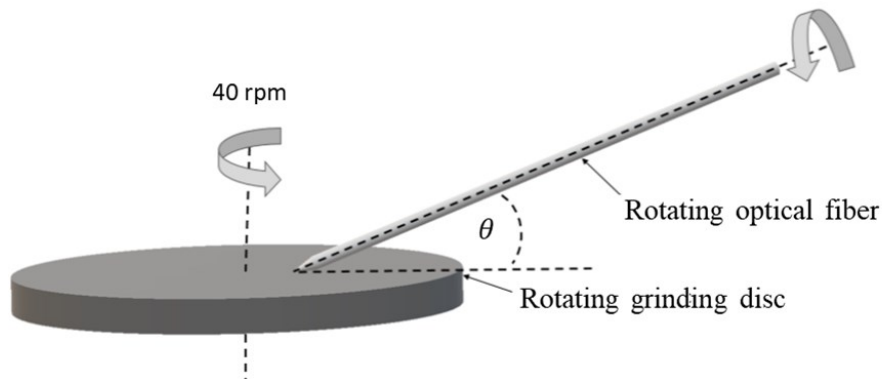


**Figure 2.5:** Directions of Simultaneous rotations of the optical fiber and horizontal grinding disc.

Grinding process starts with simultaneous rotation of both, grinding disc and fiber rotator. To achieve best surface quality, four grinding discs with decreasing grit size are used subsequently. After processing the fiber tip using silicon carbide films of 2500 and 4000 grit size each for 10 minutes, respectively, a polishing discs with an aluminum oxide film of 1  $\mu\text{m}$  and 0.3  $\mu\text{m}$  are used subsequently each for further 10 minutes to achieve a smoother surface of tapered fiber tips. For lubrication purposes, a drop of water is dripped periodically onto the grinding film fixed on the surface of the spinning grinding disc. Figure 2.6 illustrates initial tip formation process by using grinding disc with silicon carbide film of 2500 grit size. When changing grinding disc, angular stage with mounted fiber rotator has to be lifted and after disc substitution, lowered to initial position. The overall duration of grinding process, including preparation, required to create one cone-shaped fiber tip is estimated to be approximately one hour.

It is important to mention that commercial optical fiber (FG200UEP ThorLabs), used for optrode fabrication in this research, contains a 50  $\mu\text{m}$  thick protective polyimide coating deposited on cladding surface. This coating prevents the fiber breaking during bending and enables performing previously described mechanical grinding process. In another words, fiber tips are formed on fibers containing a protective polyimide coating, which is later removed before electrode deposition.

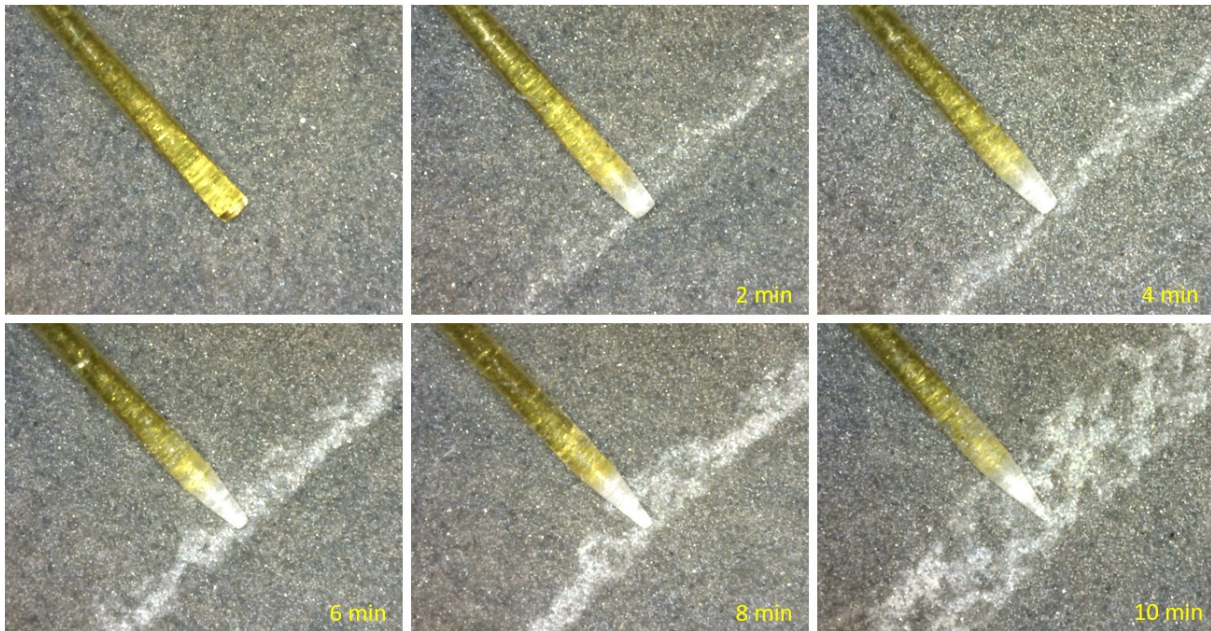


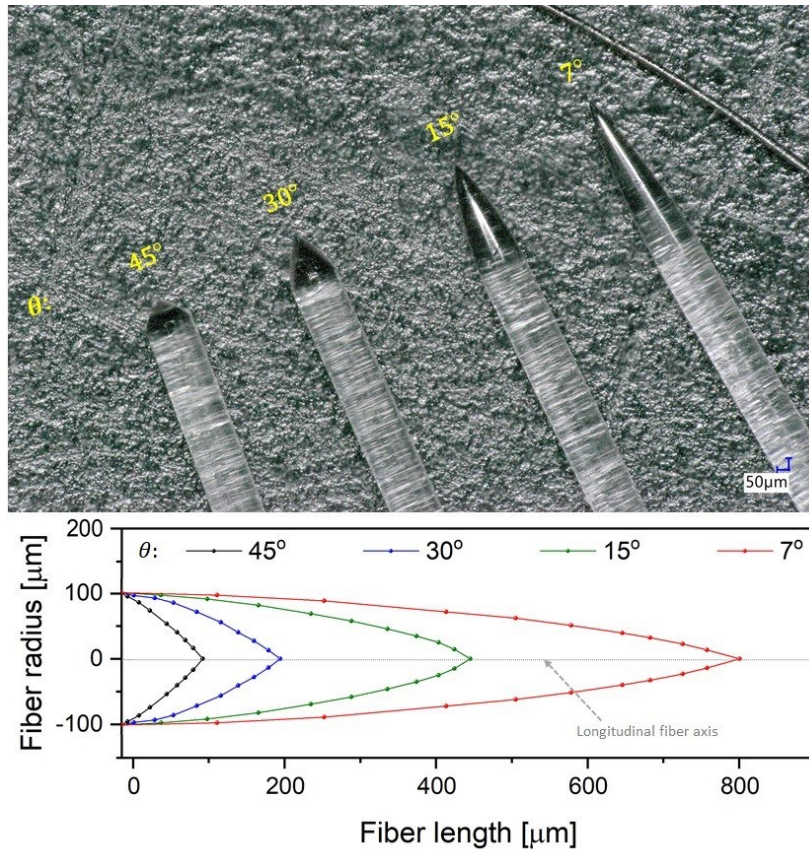
**Figure 2.6:** Fiber tip formation by mechanical grinding of optical fiber containing a protective polyimide coating. Starting from a flat cleaved fiber tip, the image shows fiber tip shape after each two minutes during initial grinding process with silicon carbide film of 2500 grit size.

### 2.1.2 Results and discussion

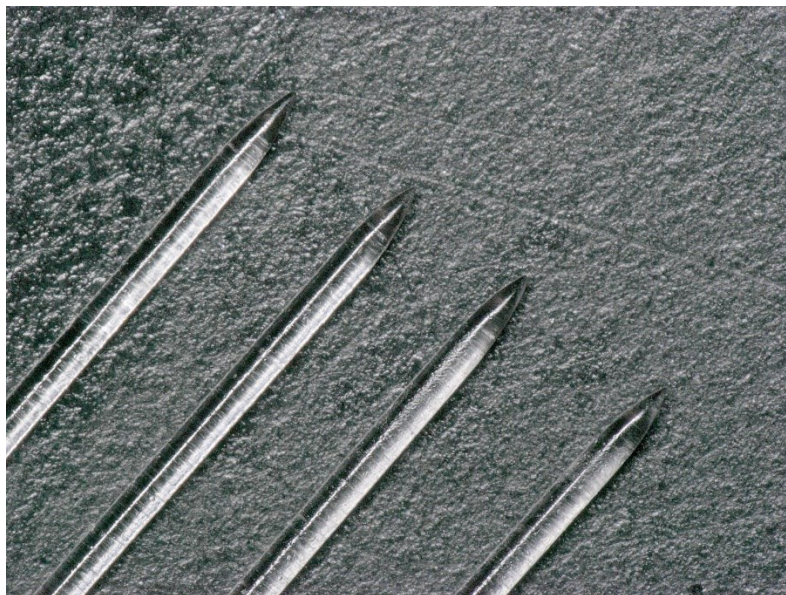
Using previously described procedure and applying different angular stage for each fiber, good optical quality fiber tips with four different cone angles were produced (

Figure 2.7). Fiber tip profiles of different cone angles (Figure 2.7), obtained by measurements performed using scanning electron microscope (SEM), suggest that polishing angle not only determines the cone angle (according to Eq. 2.1), but also affects the shape of the tapered conical fiber tip.

It can be noted that, in case of large cone angles, fiber tip radius decreases linearly along the axial fiber direction, whereas the convex shape, as well as increased radius reduction rate towards tip end are characteristics of fiber tips with small cone angles. Nonlinear radius reduction of the conical fiber tips in case of small polishing angles is probably due to minor fluctuation in polishing angle caused by small mechanical vibrations between the optical fiber and grinding disc. Reducing the speed of booth, grinding disc and fiber rotator would result in a less curved tip shape, but longer processing time. Another factor that may affect cone shape is the subsequent change of grinding discs which requires lifting the fiber, and placing it again on another grinding disc. Although a precise fiber positioning relative to the grinding disc is achieved by using a digital microscope camera before each grinding process, as well as after each grinding disc substitution, minor fluctuations in fiber positioning are possible. To demonstrate fabrication repeatability, four fiber tips are processed using the above-described method with a polishing angle of  $15^\circ$  (Figure 2.8).



**Figure 2.7:** (Above) Optical microscope image of four conical fiber tips with different cone angles formed by using different angular stages (7°, 15°, 30° and 45°) and four grinding discs (silicon carbide film of 2500 and 4000 grit size, and an aluminum oxide film of 1 µm and 0.3 µm) with following process parameters: grinding disc rotation speed of 40 rpm, fiber rotation speed of 20 rpm, processing time 40 min (each grinding disc was used for 10 min); (Below) Fiber tip profile diagrams based on SEM measurements of four fiber tips with different cone angles.



**Figure 2.8:** Optical microscope image showing four equally processed fiber tips by mechanical polishing of flat-ended cleaved optical fiber with 15° polishing angle. Tips are created using the following process parameters: grinding disc rotation speed of 40 rpm, fiber rotation speed of 20 rpm, processing time 40 min (each grinding disc was used for 10 min).

Measurements performed with SEM confirm relation between polishing angle (of angular stage) and cone angle of created tips given by (2.1). For better visualization of tip surface, SEM image of above mentioned four fiber tips with various cone angles is presented on Figure 2.9.

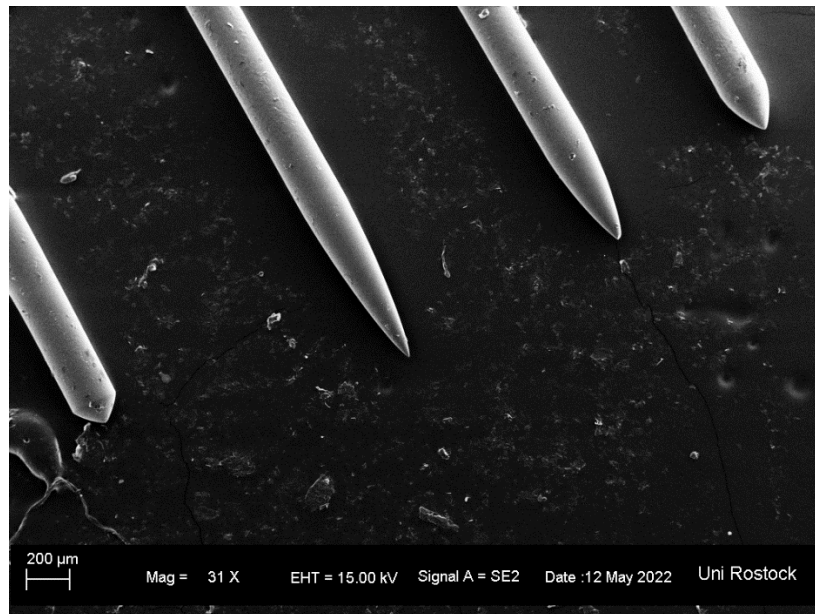


**Figure 2.9:** SEM image of four tapered fiber tips with different cone angles ( $14^\circ$ ,  $30^\circ$ ,  $45^\circ$ , and  $90^\circ$ ) created using mechanical grinding setup. Cone angles of created fiber tips correspond to polishing angles (2.1).

Although, an increase in rotating speed of grinding disc and/or fiber rotator can accelerate fiber tip formation and save time, more importance needs to be given to a tip surface quality. For example, doubling the rotation speed of grinding disc (from 40 to 80 rpm), and reducing a processing time to half (from 10 to 5 min for each grinding disc) results in a fiber tip with noticeable surface roughness (Figure 2.10, left), which would affect its optical performance. In attempt to avoid a convex shape of the cone tip, which can be caused by subsequent change of grinding discs which requires lifting the fiber and placing it again on another grinding disc, grinding process was conducted using only two grinding discs (silicon carbide film of 2500 and 4000 grit size) with the process parameters described in Chapter 2.1.1. The result of such process is presented on Figure 2.10 (right). Due to high surface roughness, an optical performance of such fiber tips would be far from acceptable.

Pervious examples (Figure 2.10) demonstrate the importance of a proper establishment of process parameters when shaping a fiber tip. However, even if the process parameters allow development of a high-quality cone tips, there is another factor that may affect their quality. When placing the fiber in a V-groove of fiber rotator, one needs to pay a special attention that fiber is properly centered and aligned in the groove. Misalignment of the optical fiber would lead to asymmetric cone shape (Figure 2.11). To ensure a proper fiber placement in a groove, usage of micromanipulators and a constant observation of alignment process with microscope is advised. In addition, when assembling above described setup for fiber tip shaping, horizontal spinning disc needs to be well balanced, and the whole setup should be positioned on a vibration isolation table.

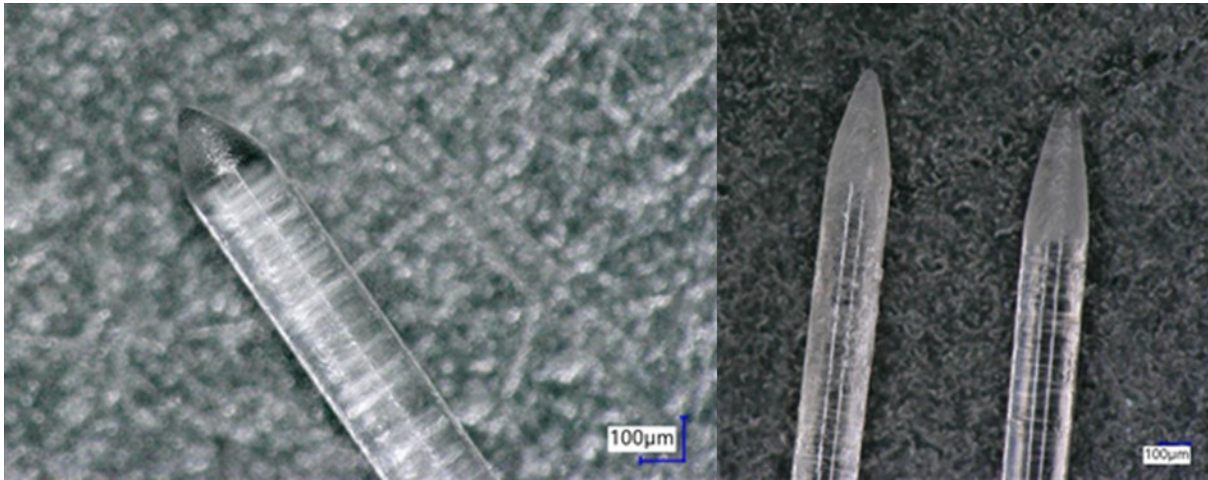


**Figure 2.10:** (left) Fiber tip created using four grinding discs (silicon carbide film of 2500 and 4000 grit size, and aluminum oxide film of 1  $\mu\text{m}$  and 0.3  $\mu\text{m}$ ) with following process parameters: angular stage of 30°, grinding disc rotation speed of 80 rpm, fiber rotation speed of 20 rpm, processing time 20 min (each grinding disc was used for 5 min). A noticeable surface roughness is a result of insufficient grinding and polishing time; (right) Fiber tips created using two grinding discs (silicon carbide film of 2500 and 4000 grit size) with following process parameters: angular stage of 15°, grinding disc rotation speed of 40 rpm, fiber rotation speed of 20 rpm, processing time 20 min (each grinding disc was used for 10 min). Very high surface roughness is a consequence of not using aluminum oxide polishing films.



**Figure 2.11:** Optical fiber with asymmetric cone shape, created using mechanical grinding setup, caused by misalignment of the optical fiber in the V-groove of fiber rotator.

## 2.2 Electrode deposition

In order to perform electrophysiological recording, while delivering light, metal micro-electrodes represent important components of each dual-function optrode. In most fiber-based optrodes (see chapter 1.2.2) one or more single microelectrodes, or electrode bundles (usually tetrodes) are inserted together with the optical fiber into the tissue of interest. This approach represents a multi-tip optrode with a risk of tissue damage during the insertion. However, using a metal coating on the optical fiber would allow electrical recording with minimal invasiveness. In case of optrode fabricated in this research, two separate equidistant metal lines deposited on optical fiber surface have a role of microelectrodes. This approach leads to development of a single-tip optrode enabling simultaneous light delivery and electrophysiological recording, while minimizing the tissue damage. Electrode deposition was achieved by sputtering through a shadow mask, which is a common PVD method for structured thin films.

### 2.2.1 Sputtering deposition

Sputtering deposition is achieved by bombarding a solid surface (target) with energetic ions. The collision between the surface atoms and energetic particles can be explained by thermal vaporization or momentum transfer theories. Thermal vaporization theory suggests that due to the bombardment with energetic ions target surface is heated enough to be vaporized, while the momentum transfer theory explains that the surface atoms of the target are emitted due to the kinetic momentum transfer from the incident particles to target surface. Since the sputtering is caused by interactions of the incident ions with the target surface, the quality of the sputtered films is influenced by the type and structure of the target material, as well as by the energy and angle of incident ions. The target has usually the disc shape and it is made of a metal or an alloy. Sputtering is an efficient process and the most of the power input to the system is transferred to the target, which leads to its heating. Targets are usually mounted on a water-cooled plate. The condition of the target strongly influences the quality of the sputtered thin film. Thickness distribution of the sputtered film strongly depends on angular distribution of sputtered particles and the collisions of sputtered particles with the gas molecules.

The most used sputtering system is a direct current (DC) sputtering (Figure 2.12). This system is composed of a pair of planar electrodes, cathode and anode. The front surface of the cathode is covered with the target material to be deposited, while the substrate material is placed on anode. The sputtering gas (usually argon) fills the sputtering chamber. Application of DC voltage between the electrodes maintains the glow discharge. Argon ions generated in the low discharge are accelerated at the cathode (target) which results in deposition of the thin film of the cathode target on the substrate [133]. In DC sputtering system, the target is composed of a metal since the glow discharge (current flow) is maintained between the metallic electrodes.

The deposition rate can be increased by lowering the sputtering pressure, which is achieved with magnetron-type discharge (Figure 2.13). In the magnetron sputtering system, a magnetic field is superposed on the cathode, parallel with the cathode surface. The electrons in the glow discharge show cycloid motion with the orbit center drifted in a direction of  $\mathbf{E} \times \mathbf{B}$  with a drift velocity of  $\mathbf{E}/\mathbf{B}$ , where  $\mathbf{E}$  and  $\mathbf{B}$  represent the electric field in the discharge and a superposed transverse magnetic field, respectively [133]. The orientation of the magnetic field is such that these drift paths for electrons form a closed loop. Described electron trapping effect increases

the collision rate between the electrodes and the sputtering gas molecules, which gives a possibility of lowering the sputtering gas pressure to approximately 0.5 to 1 Pa [133].

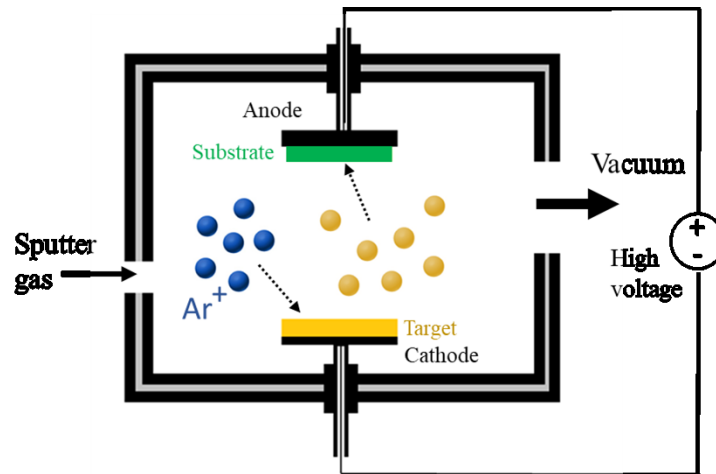


*Figure 2.12: Schematic representation of direct current (DC) sputtering system.*

In magnetron sputtering system magnetic field increases the plasma density leading to a higher current density at the cathode target, which increases the sputtering rate at the target. Due to the low gas pressure, the sputtered particles travel through the discharge space without collisions, which results in a high deposition rate. Low pressure sputtering is one of the most promising techniques for the production of thin film devices ensuring the little film contamination with high deposition rate. For the metal deposition pure Argon gas is introduced through a variable leak valve. Using a reactive gas, such as Oxygen, makes possible the deposition of a metal oxides from a metal target, which is known as reactive sputtering.

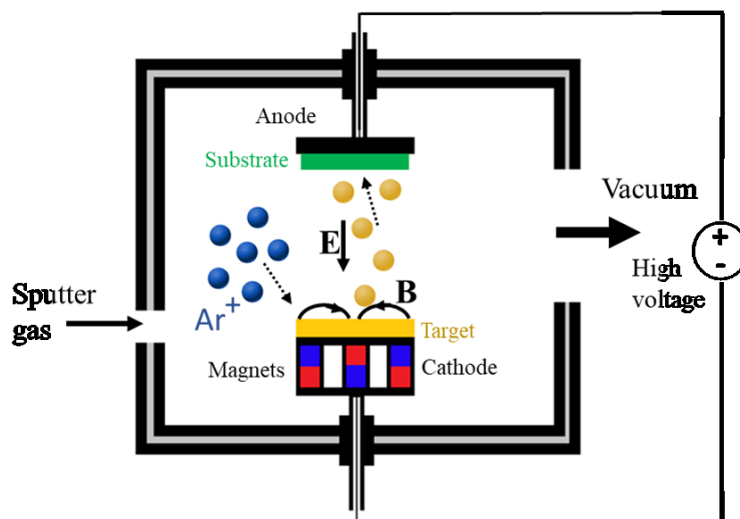


*Figure 2.13: Schematic representation of magnetron sputtering system.*

The growth of a thin film is a statistical process of nucleation, surface diffusion-controlled growth of the three-dimensional nuclei and formation of a network structure and its subsequent

filling towards a continuous film. The nucleation and growth process depend on thermodynamic parameters of the deposit, as well as on the substrate surface. Chemical nature, cleanliness, and the microscopic topography of the substrate surface have a strong effect on the adhesion of the film to the substrate. The adhesion of the film can be improved by providing more nucleation centers on the substrate by using a fine-grained substrate, or a substrate pre-coated with suitable materials.

### 2.2.2 Methods

Details of electrode deposition using magnetron sputtering approach will be presented in next section. Surface cleaning represents very important step prior to deposition of metal film. The effect of surface treatment procedure on adhesion of thin film will be also discussed.

#### Surface cleaning

When fiber tip is formed, polyimide protective coating is removed from the optical fiber using hot sulphuric acid (130 °C). This procedure is associated with health hazards and should be performed in chemical laboratory environment. Open flame is another, safer, way to remove polyimide coating from the optical fibers, but it tends to increase glass surface brittleness. Since the optrode strength and elasticity are important, this approach was not applicable in optrode fabrication process.

After polyimide is removed from optical fiber surface, pre-cleaning of the fiber surface is conducted with acetone using ultrasonic support. Prior to electrode deposition, in order to promote the adhesion, 10 nm thick titanium layer is deposited on surface of glass fiber. A very poor adhesion is observed, expressed in film inhomogeneity and delamination (Figure 2.14, left). Therefore, more thorough physical treatment is required. A plasma oven (Femto, version D, Diener electronic Plasma-Surface-Technology GmbH) is used to activate the surface and promote adhesion by removing organic contaminants. Oxygen plasma surface treatment is performed for 10 minutes under following conditions: pressure  $p = 0.3$  mbar, power 90%, chamber temperature  $T = 100$  °C.

Bare glass fibers, previously cleaned with acetone and rinsed with deionized water, are placed between electrodes in a vacuum chamber of the device for plasma surface treatment. After a vacuum has been created, using the pump, small amount of oxygen is injected into the chamber. Next, free electrons are accelerated by the electric field between electrodes, and their collisions with gas molecules create more free electrons and ions. As these free electrons and ions interact with glass surfaces of optical fibers placed in chamber, molecular bonds of the first few surface layers become broken, which creates chemically reactive sites and improves the adhesion of sputtered thin film. During plasma treatment, inorganic and microbial surface contaminants that form due to exposure to air are turned into a vapor and removed leaving no residues on the glass substrate. Such contaminants usually reduce quality of adhesive bonding by forming a weak intermediate layer. Adhesion is much improved after plasma surface treatment, resulting in a homogeneous thin film without delamination (Figure 2.14, right).



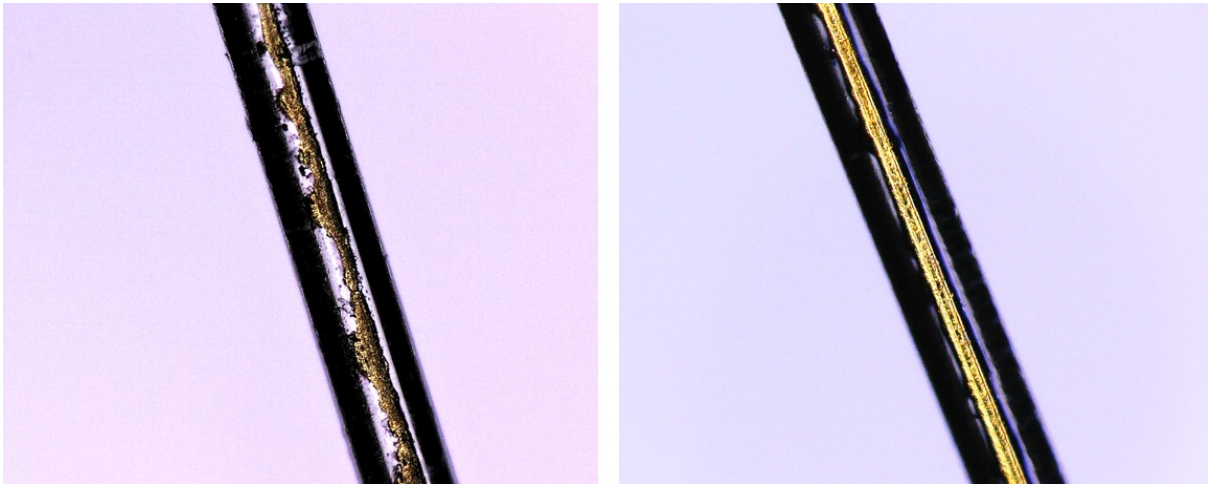


**Figure 2.14:** (left) Microscope image of electrode deposited on the surface of optical fiber after cleaning with acetone using ultrasonic support; (right) Microscope image of electrode deposited on optical fiber surface after plasma surface treatment which was an additional surface cleaning procedure after cleaning with acetone. In both cases, a very thin (10 nm) titanium layer is deposited prior to gold deposition.

### Electrode deposition

Following plasma surface treatment, optical fiber with cone tip is placed in a rectangular groove of custom fiber holder, and a 50  $\mu\text{m}$  thick stainless steel shadow mask, featuring a 50  $\mu\text{m}$  wide and 7 cm long laser cut slit opening, was aligned and fixed on the fiber holder with temperature resistant polyimide tape (Figure 2.15). Precise alignment of the shadow mask to the centre of fiber groove was done using optical microscope. Fiber holder contains a rectangular 7.5 cm long groove with the opening cross section  $230 \times 230 \mu\text{m}$ . When placed inside the groove, optical fiber is unlikely to move or rotate during the sputtering process, which leads to deposition of the straight electrode with uniform width. Since the fiber has a conical tip, micromanipulators are used together with microscope to achieve precise alignment of the fiber tip to the mask opening, which enables electrode deposition on the fiber tip.

Following mask and fiber alignment, fiber holder is mounted on a substrate holder and placed in a substrate transport device in a lock chamber of magnetron sputtering equipment (Von Ardenne LA 320S). Substrate is then moved from a lock into evacuated sputtering chamber, with a titanium and polycrystalline gold sputtering targets (99.99% purity), where the high vacuum ( $5 \cdot 10^{-6}$  mbar) is generated in order to minimize the partial pressures of all background gasses and possible contaminants. This procedure takes approximately 30 minutes.

After high vacuum has been established, sputtering gas (Argon), which comprise the plasma, is flowed into the chamber and total pressure is regulated using a pressure control system. As already described, in a magnetron sputtering system, a very strong magnetic field confine the electrons in the plasma near the target surface which increases the deposition rate and makes it possible to achieve gold films with good morphology, and also prevents the damage which would be caused by direct impact of electrons with the growing film. The substrate transport device is designed such that the substrate, mounted on a substrate holder, hangs upside down in sputtering chamber and is sputtered from below. The equipment offers a possibility of a manual setting of sputtering time and power, which gives the possibility to control film thickness and morphology.

Position of the optical fiber relative to the slit opening during the sputtering deposition is presented on Figure 2.16. Substrate holder, designed to fit in substrate transport device of sputtering equipment, while enabling placement of above described fiber holder is presented on Figure 2.17. Fiber holder is placed on a substrate holder such that slit opening of shadow mask faces sputtering target. Heat resistant polyimide tape is used to fix fiber holder and prevent its movement during sputtering process.

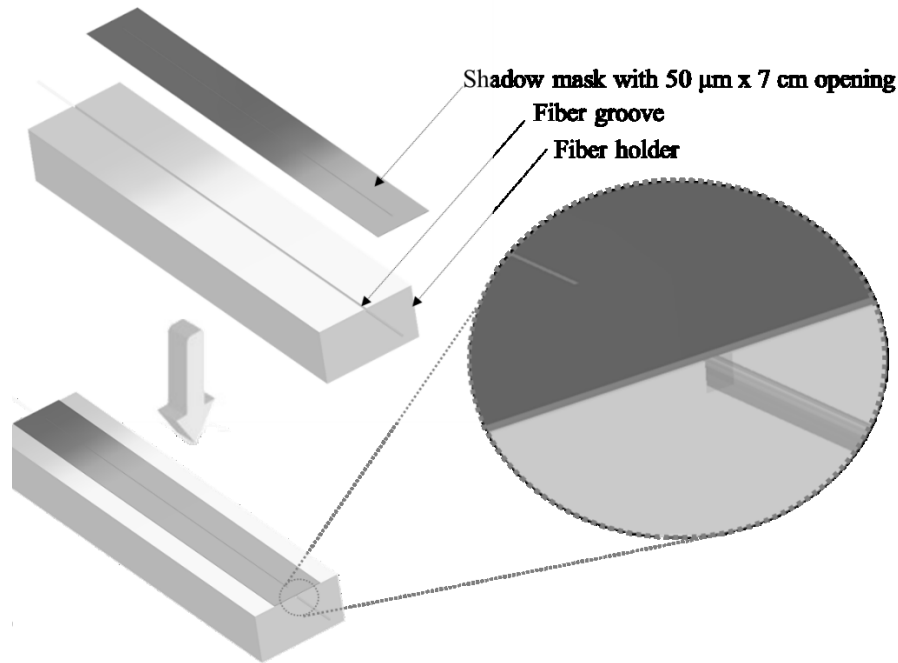


*Figure 2.15: Custom made fiber holder with aligned shadow mask for electrode deposition on the optical fiber surface.*

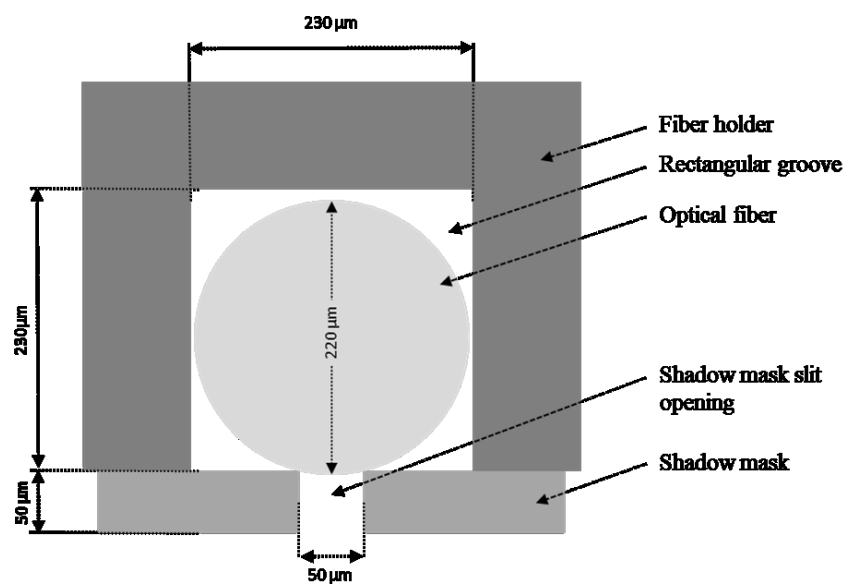


*Figure 2.16: Schematic representation of the position of optical fiber inside rectangular groove during sputtering process.*

Prior to gold sputtering deposition, a thin titanium film (10 nm) is deposited on the fiber glass surface as an intermediate layer to enhance gold adhesion. Deposition time of 600 seconds and a DC power of 200 Watts are used to deposit a first gold microelectrode. When the sputtering process is finished, fiber holder together with the optical fiber is removed from sputtering equipment.

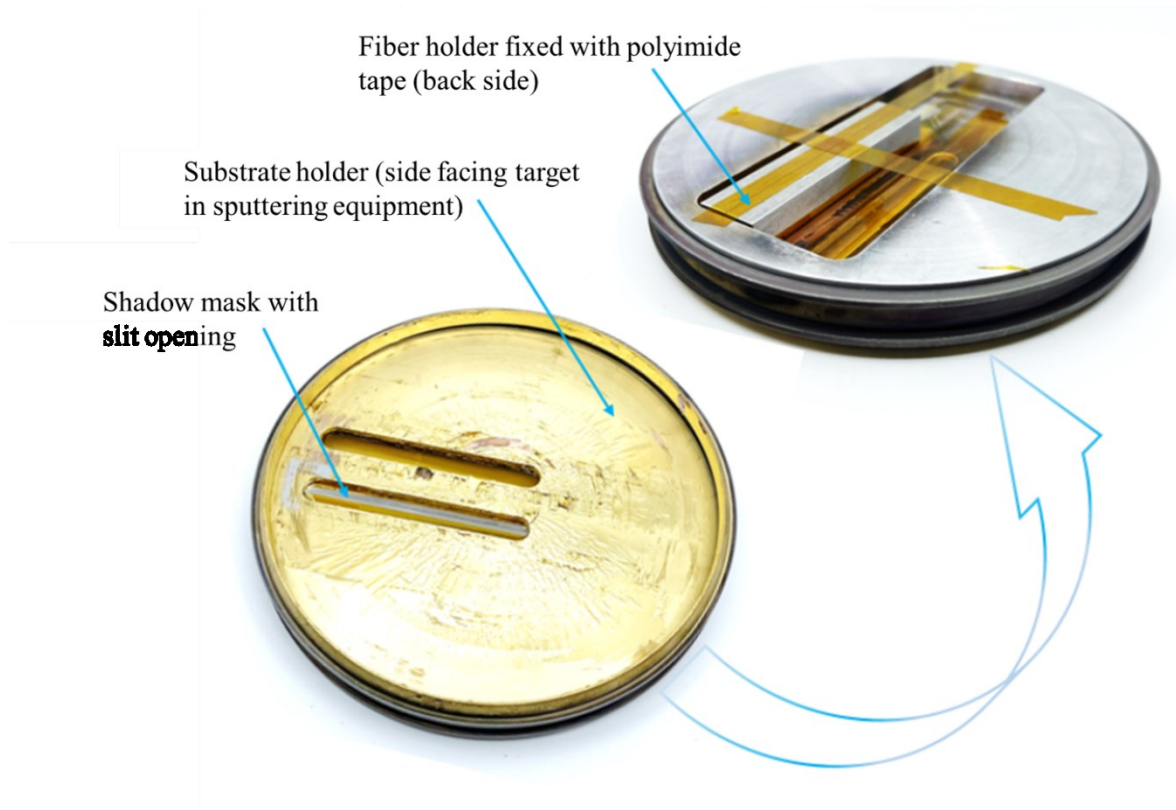


**Figure 2.17:** Substrate holder designed to fit in substrate transport device of the sputtering equipment. Fiber holder is placed and fixed on substrate holder such that slit opening of the shadow mask faces the sputtering target.

To sputter second electrode on same optical fiber, precise rotation and alignment setup, consisting of micromanipulators and fiber rotator is used (Figure 2.18). Since shadow mask was fixed on fiber holder with temperature resistant tape, there is no need for a new mask alignment. Fiber holder together with optical fiber is placed on micromanipulator on the left side of alignment setup, such that one end of optical fiber is close enough to be fixed in fiber rotator positioned on opposite micromanipulator on the right side. After fixing its one end in fiber rotator, optical fiber is rotated while still being in a groove of fiber holder with aligned mask. Since the goal is to achieve two separate equidistant gold microelectrodes on same optical fiber, a rotation angle of  $180^\circ$  after first sputtering is required. After rotation for  $180^\circ$ , fiber holder is again placed in the sputtering equipment and sputtering process is repeated. To ensure a very precise alignment, especially of fiber tip, whole alignment process is observed with digital microscope.

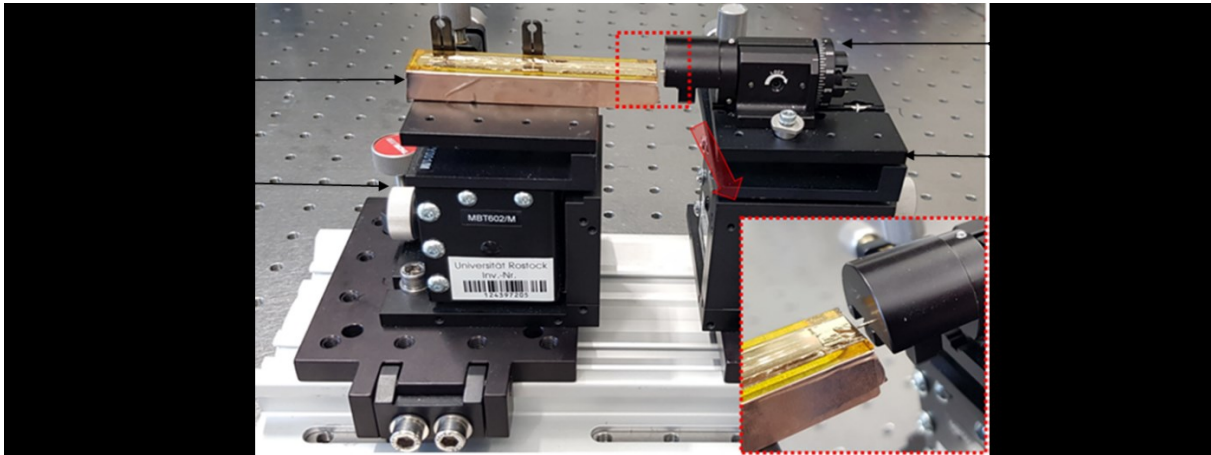


**Figure 2.18:** Custom precision fiber rotation setup for multiple electrode deposition on the same fiber with controlled angular orientation.

### 2.2.3 Results and discussion

Detailed structural study of deposited microelectrodes was conducted using scanning electron microscope (SEM) (Supra 25, Carl Zeiss AG). In order to study a cross section of the optical fiber with two deposited electrodes, a special sample preparation is required. Optical fiber with deposited gold electrodes was cut in  $\sim 1$ cm long pieces which are fixed in vertical position and embedded in epoxy. Curing is achieved after 24h at a room temperature. After the epoxy cured completely, it was grinded and polished into a disc shape (Figure 2.19). Upper disc surface is sputtered with a very thin gold layer ( $\sim 5$ nm) and placed on a sample holder in SEM.



**Figure 2.19:** Sample preparation for obtaining a cross-section image of optical fiber using SEM.

Microscopic cross-section image of optical fiber with two deposited gold electrodes (600 seconds deposition time, 200 W DC power) is presented on Figure 2.20 (left). For a better understanding of electrode shape and thickness, magnified SEM image of a single gold electrode deposited on a fiber glass surface is presented on Figure 2.20 (right). It can be noted that electrode thickness decreases towards both ends in the same manner. This effect is probably due to a curved fiber surface, and it is correlated to an increase in spacing between the fiber surface and the slit opening starting from the centre towards both ends of slit opening width. Precise alignment of fiber cone tip relative to the slit opening on shadow mask enables sputtering deposition of electrode on the cone tip (Figure 2.21). An increased electrode width on cone tip is due to a larger under sputtering effect caused by increased distance between fiber tip surface and slit opening of the shadow mask.

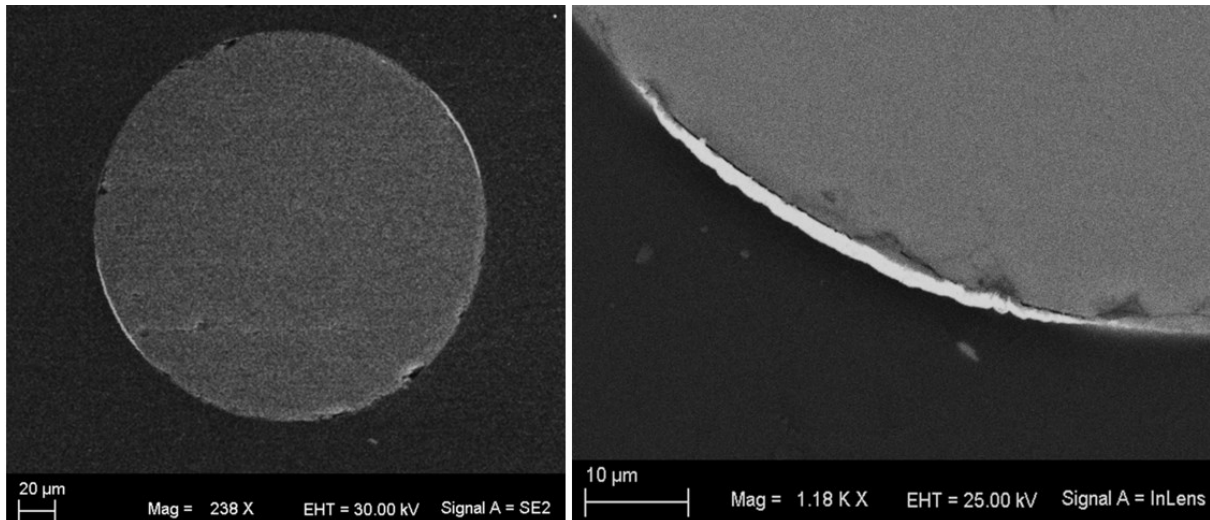


**Figure 2.20:** (left) Cross-sectional SEM image of an optical fiber with two equally spaced gold electrodes (600 s deposition time, 200 W DC power); (right) Magnified SEM image of a single gold electrode deposited on a glass surface of optical fiber.



**Figure 2.21:** Microscope image of gold microelectrode deposited on cone tip of the optical fiber.

Thickness of deposited microelectrode can be controlled by controlling parameters of sputtering deposition process (DC power and sputtering time). However, some processes during deposition affect thickness uniformity of the resulting layer in magnetron sputtering. The effect of geometric parameters, such as distance between target and substrate, ionic energy, target erosion area, gas pressure, and substrate temperature influence thickness uniformity of deposited thin films. Furthermore, surface homogeneity of the target plays significant role in film thickness distribution.

Reliable and accurate thickness measurement, based on step height measurements and 2D surface roughness characterization, of electrodes fabricated in this work are conducted using surface profiler (DektakXT stylus, Bruker). Since such measurements are limited to flat substrates, gold microelectrodes are sputtered on flat glass surface after plasma surface treatment, using the same shadow mask and process parameters (600 seconds processing time,

200 W DC power) as in case of electrode deposition on optical fiber surface. To ensure a direct contact between the shadow mask and a glass substrate, mask is fixed on a glass substrate using temperature resistant polyimide tape. Thickness profile of such 60 mm long gold microelectrode deposited on a flat glass substrate is presented on Figure 2.22.

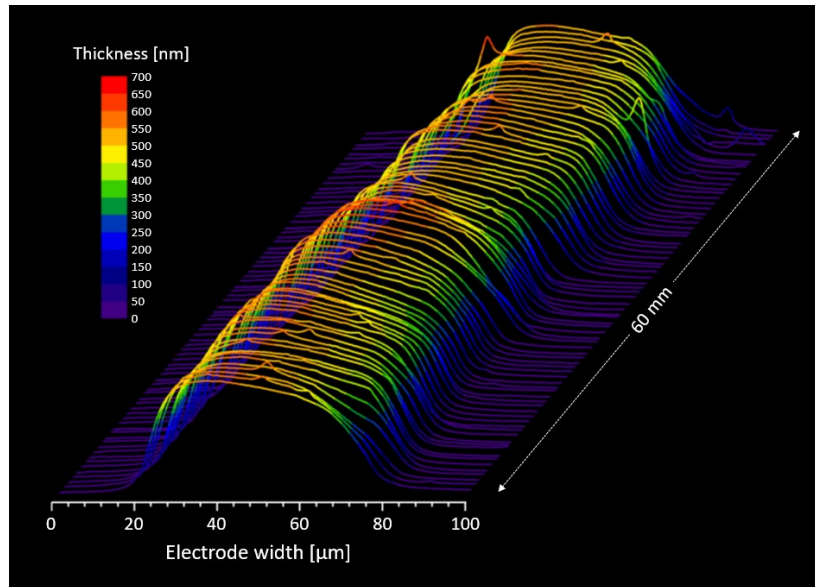


**Figure 2.22:** Thickness profile of 60 mm long gold microelectrode deposited by DC magnetron sputtering (600 s deposition time, 200 W DC power) on a plasma treated flat glass surface through a 100  $\mu\text{m}$  thick stainless steel shadow mask featuring a 50  $\mu\text{m}$  wide and 7 cm long laser cut slit opening.

Maximum electrode thickness is estimated to be around 700 nm, with approximately 150 nm thickness variation at the electrode surface. Measured electrode width is around 15  $\mu\text{m}$  larger compared to width of the shadow mask slit opening. Even though a very close direct contact between the shadow mask and glass substrate is achieved, there is always a small spacing between the slit opening and a substrate surface. This small spacing causes a shadowing effect resulting in slightly larger electrode width compared to the width of the slit opening on the shadow mask [134]. Another factor that may influence the electrode width is a thermal expansion of the shadow mask material due to an increase in temperature during the sputtering process.

## 2.3 Mechanical support and electrode insulation

Due to its brittleness, bare optical fiber with a cone tip and two deposited microelectrodes would face a serious mechanical issues leading to its breaking during the insertion. Moreover, even if a breaking could be avoided by a careful insertion, this optrode wouldn't be applicable to any in vivo experiments with a moving animals. To avoid optrode breaking, and to improve its overall mechanical stability, two approaches for application of thin biocompatible coatings are included in optrode fabrication process. First approach refers to the application of Polytetrafluoroethylene (PTFE) heat shrink tube, while second approach represents dip-coating procedure using biocompatible UV-curable epoxy. In addition to mechanical support, applied coatings have a role of electrode insulation and its protection from the moist body environment. Precise application of heat shrink tube or epoxy coating would allow to control exposed

electrode area in the tip region, which affects impedance magnitude and is crucial for electrode recording performance. The details of both procedures, as well as a discussion on mechanical performance based on results of three-point bending test will be presented in this chapter.

### 2.3.1 Materials and methods

#### Heat-shrink tube

Following electrode deposition, optical fiber is inserted in a PTFE heat shrink tube (PTFE Sub-Lite Wall®, Zeus Industrial Products, Inc.) with a diameter slightly larger than that of optical fiber. To make sure that optrode would be able to perform electrical recording, a small portion of deposited microelectrodes in the fiber tip region needs to remain exposed, which is achieved by precise positioning of the heat shrink tube. To ensure that the tube shrinks evenly, after insertion of optical fiber in a thermoplastic tube and its positioning, shrinking process takes place in oven at 350 °C for 5 minutes. A very good adhesion between the tube and optical fiber is observed with SEM, and tube thickness after curing is estimated to be approximately 40 μm (Figure 2.23).

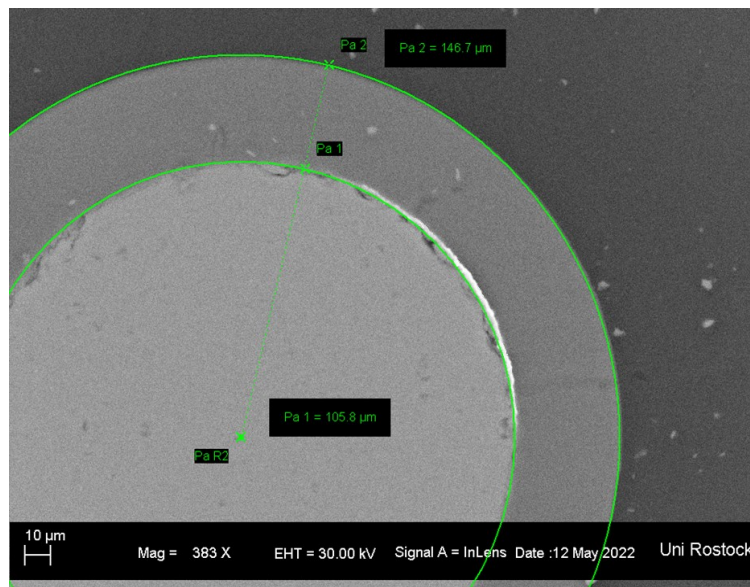


**Figure 2.23:** Cross section SEM image of a PTFE shrink tube around optical fiber with deposited electrodes. Heat shrinking is achieved in a furnace at 350 °C for 5 minutes. Tube thickness after curing is estimated to be approximately 40 μm.

To enable control of the exposed electrode length, the extent of tube length reduction needs to be determined. Since the product datasheet contains only information about radial shrinking, an extent of tube length reduction is estimated manually by repeating shrinking procedure at the same temperature (350°C). After a few repetitions of shrinking process in case of 5 cm long PTFE tube, length shrinkage of approximately 500 μm was observed on both ends of the tube. This information provided the possibility to control the exposed portion of the deposited microelectrodes that would serve as electrical recording sites.

Since the electrical recording in optogenetic experiment should be locally constrained to the activated volume, a small portion of 60 μm wide electrode would be sufficient to perform such measurements. To achieve that, optical fiber with a cone tip and deposited electrodes is placed

inside the 5 cm long PTFE tube such that distance between electrode onset and tube onset is approximately 1 mm (Figure 2.24, left). Microscope image of optrode containing shrink tube, such that a small portion of microelectrodes ( $\sim 500 \mu\text{m}$  long) in the tip region is exposed, is presented on Figure 2.24 (right). This is just an example of the possibility to control exposed electrode area. Exact size of exposed electrode area, as well as the effect of exposed electrode area on recording performance of deposited electrodes will be discussed later in terms of electrical characterization. On the other end of the optrode, a bit larger portions of the deposited electrodes are exposed in order to establish the electrical contacts.

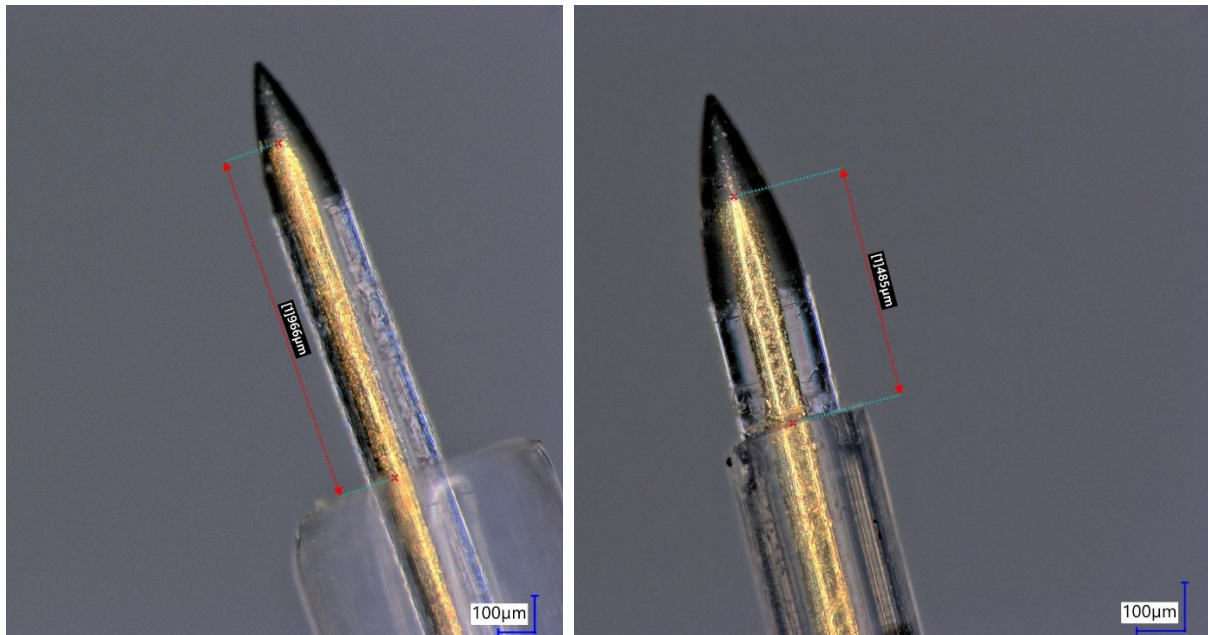


**Figure 2.24:** Control of exposed electrode area by application of heat shrinking of PTFE tube. (left) positioning of PTFE heat shrink tube on optical fiber with deposited gold microelectrode. (right) outcome of the shrinking procedure (at  $350^\circ\text{C}$  for 5 minutes).

The PTFE Sub-Lite-Wall<sup>®</sup> tube, used in this research, represents the thinnest biocompatible heat shrink tube currently available on the market. Being sterilizable and fully biocompatible (certified USP Class VI biocompatibility) makes them suitable for application in medical and clinical devices. USP class testing is the most common testing method for determination of materials bio-compatibility. There are six classes, VI being the most rigorous. Class VI testing is aimed to certify that there are no harmful reactions or long-term bodily effects caused by chemicals that leach out of plastic materials. Furthermore, having the lowest friction coefficient compared to any polymer, makes these tubes ideal for application as optrode encapsulation material which is supposed to be implanted directly in the tissue.

### Dip coating

Since it was not possible to acquire biocompatible heat shrink tube with diameter, and a wall thickness less than that of PTFE Sub-Lite-Wall<sup>®</sup> tube, dip-coating method, using biocompatible UV-curable epoxy (NOA81, Thorlabs) is applied to produce thinner optrode coating.

Dip coating, is a popular way of achieving a thin and uniform coating on flat or cylindrical substrates. In this process, the substrate is dipped into a container filled with coating material, which is normally of a low viscosity to enable the coating to run back into the bath as the



substrate emerges. This technique consists of several consecutive steps. In the first step, the substrate has to be immersed in a solution containing coating material with a constant speed. After remaining inside the solution for some time, the substrate with a thin layer of material is pulled up, at a constant speed. The film properties and film thickness depend on a number of parameters, such as: immersion time, pulling speed, number of dipping cycles, solution composition, concentration and temperature, and environmental humidity [135].

To perform a dip coating on an optical fiber, linear stage with modified sample holder is used. Optical fiber is positioned vertically, such that one end is fixed in a sample holder, while another end with a cone tip faces a container filled with epoxy. Fiber is immersed in an epoxy by constant speed movement of linear stage, and left for 60 seconds. After the constant pulling speed is set, fiber is pulled up out of the container. Remaining in a vertical position, fiber is then transferred to oven, where the baking process takes place at 90°C for 10 minutes. When baking process is finished and the fiber is cooled down, to remove the epoxy from the fiber tip region, approximately very small portion of fiber length starting from the fiber tip is immersed in a container filled with developer (mr-Dev 600, micro resist technology GmbH) and left inside for 10 minutes. Since the baked polymer layer was not exposed to UV light, prior to immersing a coated fiber tip in a developer, polymer coating on the region immersed is soluble in developer, and it is washed away by wet chemical development process.

Following the development process, fiber is placed in a UV-exposure equipment for 2 minutes. The cross section of coated fiber is observed with SEM, and a coating thickness is estimated to be approximately 9.5  $\mu\text{m}$ . Schematic representation of dip coating procedure containing steps for controlled exposure of electrode area is presented on Figure 2.25. Above described procedure enables fabrication of thin epoxy coating on optical fiber with possibility of controlling exposed electrode area. As in case of PTFE shrink tube, very good adhesion between glass surface of optical fiber and epoxy coating would protect insulated electrode portion from humid environment, which is crucial to ensure accurate electrophysiological recording.

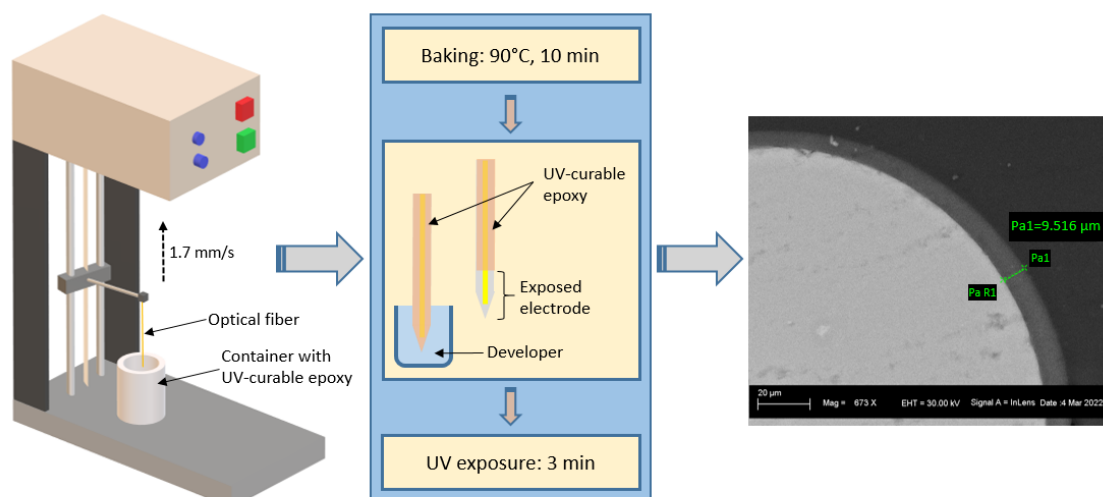


**Figure 2.25:** Dip coating procedure in case of tapered optical fiber. Coating is achieved with UV curable biocompatible epoxy.

To achieve a continuous thin film on fiber surface, pulling speed is determined based on numerous trials. The best result is achieved when using a pulling speed of 1.7 mm/s or lower. Higher speed results in non-continuous layer on the fiber surface, not covering the whole fiber length (Figure 2.26). The same procedure can be applied for dip coating of optical fiber with various biocompatible polymers. However, exact process parameters (pulling speed, number of dip cycle, UV exposure time, and duration of development) have to be determined separately for each coating material. It is important to mention that prior to dip coating, fiber surface was cleaned with acetone using ultrasonic support, and then treated with plasma, as in case of surface cleaning prior to electrode deposition. Proper surface cleaning is crucial, since it increases adhesion between optical fiber and epoxy coating.

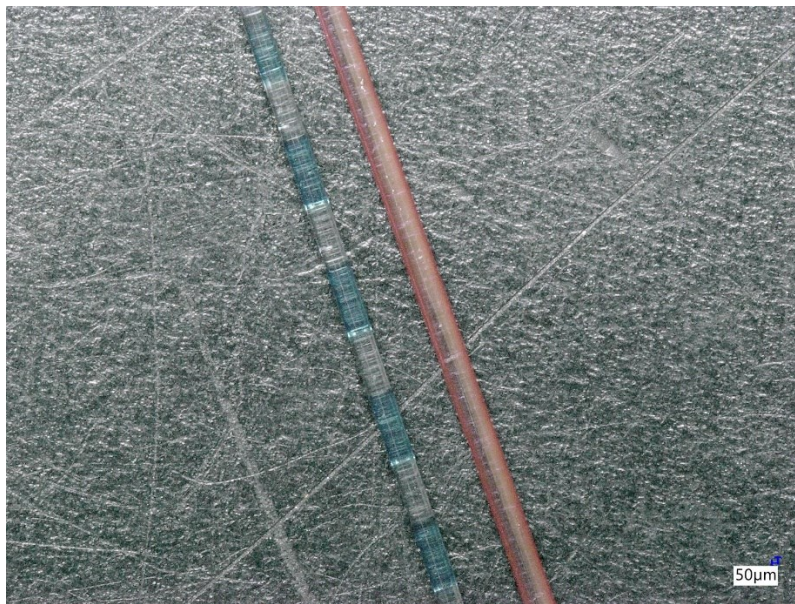


**Figure 2.26:** Determination of pulling speed in dip coating procedure. Higher pulling speed (than 1.7 mm/s) results in non-continuous fiber coating (Blue). Colored epoxy serves only for visualization purposes.

### 2.3.2 Mechanical testing

To characterize and compare mechanical behavior of bare and coated optical fibers, three-point bending tests are carried out by applying the force perpendicular to the longitudinal fiber axis. Such tests are performed using the equipment designed for testing the mechanical strength of bonding in electrical circuits (XYZTEC, Condor 70).

Being the most frequently performed bending test, three-point bending involves a sample of certain length placed on two support cylindrical pins positioned to a fixed distance (support width), and a test probe (having also a cylindrical shape) moving down to contact the sample halfway between two support pins. During the testing procedure, cylindrical test probe moves down slowly at a constant speed and loads the sample with increasing force until it deforms or breaks. The maximum load exerted during the bending test is called breaking force. During the test, applied force, distance moved by the probe and the time are recorded and graphically presented. Depending on mechanical characteristics of tested sample, different force-deflection responses can be observed. Strong and stiff samples show higher forces, while brittle samples break prior to any plastic deformation. In case of brittle samples, highest force (on force-

deflection graph) is usually assumed as sample strength. The total area (prior to breaking point) under the force-deflection graph represents the energy to failure and determines the toughness of the tested sample. Another characteristic of bending tests with brittle materials is the fracture deflection which describes the greatest possible sample deflection shortly before the fracture. Since the fracture deflection depends on support width, when comparing the toughness of few samples, it is necessary to keep it constant.

Since the equipment used to perform three-point bending tests in this work is originally made for other purposes, the setup adapted for this kind of testing differs from the previously described standard, but relies on the same principle. **Fehler! Verweisquelle konnte nicht gefunden werden.** (left) schematically illustrates the setup used for three-point bending tests performed on bare and coated optical fibers. Two support cylindrical pins are fixed on horizontal moving plate, and the optical fiber is placed on the horizontal plate in a way presented on Figure 2.27 (right). Cylindrical test probe with sensor is fixed vertically in the middle of support width very close to the optical fiber. During the testing, horizontal plate moves and pushes the optical fiber against the test probe until it reaches a breaking point. Bare optical fiber, as well as optical fibers containing heat-shrink PTFE tube and epoxy coating are submitted to three-point bending test with the same parameters, and force-deflection graphs are plotted based on recorded data.

Figure 2.28 shows load-displacement curves obtained from three-point bending tests in case of bare optical fiber, fiber dip-coated with UV-curable epoxy, and fiber with heat-shrink PTFE tube. By comparing load-displacement curves for all three optical fibers, it is clear that they exhibit similar flexural behavior. All three optical fibers show an elastic behavior with load increasing linearly up to breaking point. When the breaking occurs, load drops severely. Compared to bare optical fiber, coated fibers tolerate higher maximum load until breaking. According to load-displacement curves obtained from three-point bending tests, 35% increase in load tolerance is achieved in case of epoxy coated fiber, while PTFE shrink tube application leads to more than 100% increase in load tolerance.

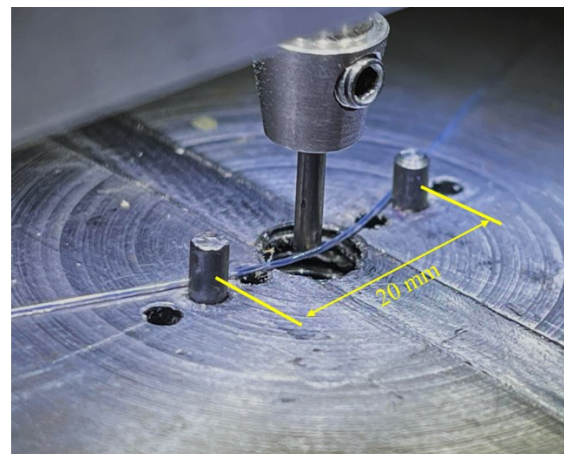
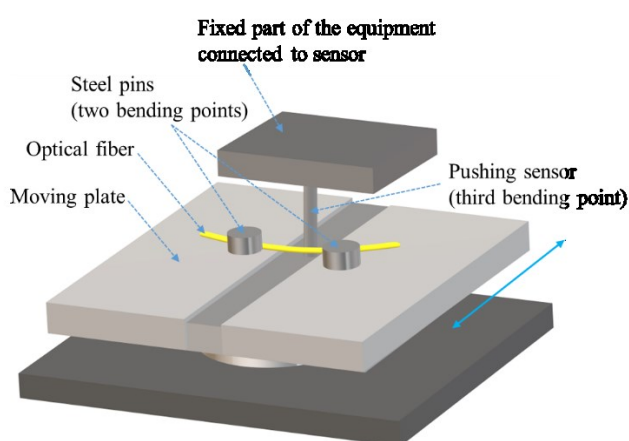


**Figure 2.27:** (left) Schematic representation of three-point bending test for bare and coated optical fibers, (right) Optical fiber during three point-bending test.

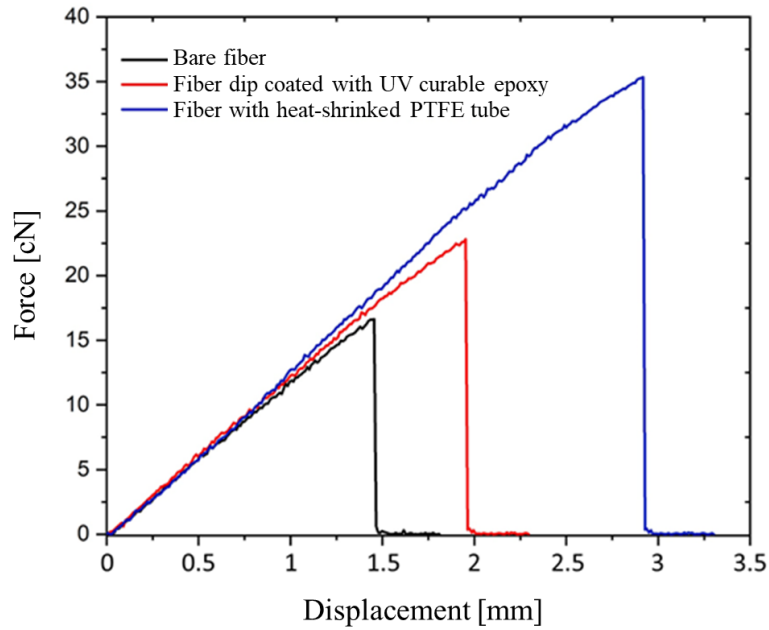


**Figure 2.28:** Comparison of the results of 3 point bending tests in case of bare and coated optical fiber.

## 2.4 Optrode assembly

Fabrication process of cone fiber tips with various angles using mechanical grinding setup, as well as electrode deposition methodology are previously explained in detail. To enable optrode implantation without fracture, mechanical protection is applied in form of heat-shrink tube or epoxy coating. Turning an optrode into a functional device for optogenetic experiments requires additional assembly procedure. To enable electrophysiological recording, deposited electrodes must be electrically connected to PCB. Furthermore, light delivery can only be achieved if fiber-based optrode is coupled to an external light source. Schematic representation of optrode assembly is presented on Figure 2.29.

FR4 (flame retardant) substrate (1.5 mm thick), with deposited copper layer on one side, is cut in square pieces (10 x 10 mm<sup>2</sup>). After drilling of a small hole (300 μm diameter) in the middle of FR4 substrate, 100 μm wide and 500 μm deep groove is formed such to pass through hole centre and divide copper layer into two separate parts. Optrode with heat shrink tube is positioned perpendicular to the surface of FR4 substrate, and moved through the hole until the copper covered substrate surface reaches the end of heat shrink tube near flat cleaved end (opposite to the cone tip). Optrode is then rotated such that position of deposited microelectrodes corresponds to the position of copper layers on FR4 substrate. When properly positioned, in respect to FR4 substrate, optrode part containing heat shrink tube is fixed to uncoated FR4 substrate surface using UV-curable epoxy. Next, conductive silver epoxy is applied on the interface between microelectrodes and copper layer on FR4 substrate. After curing of the conductive silver epoxy, UV-curable epoxy is applied over the conductive silver epoxy, and ceramic ferrule is placed around bare part of optical fiber. UV exposure leads to fixing of the ceramic ferrule to the PCB. The rest of the bare fiber sticking out of the ceramic ferrule is then cut and polished. Butt-coupling between flat cleaved optrode end placed in ceramic ferrule and optogenetic patch fiber is achieved using mating sleeve.

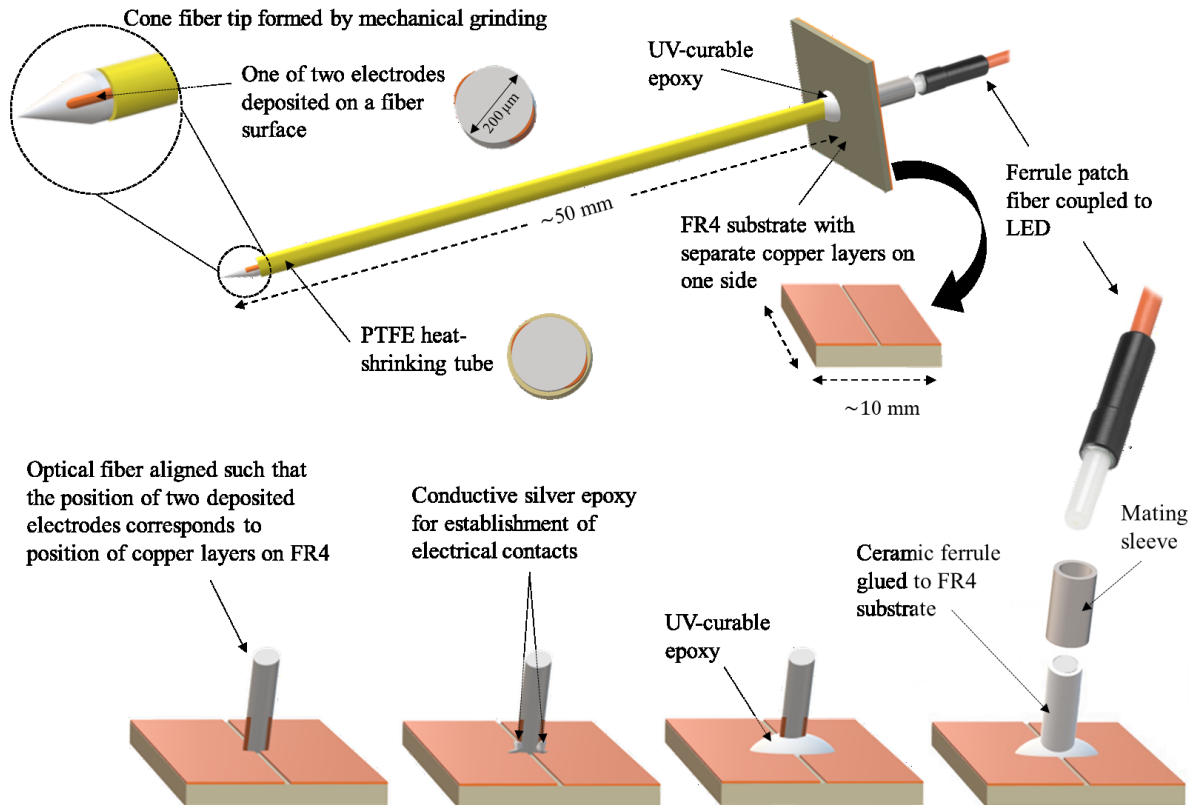
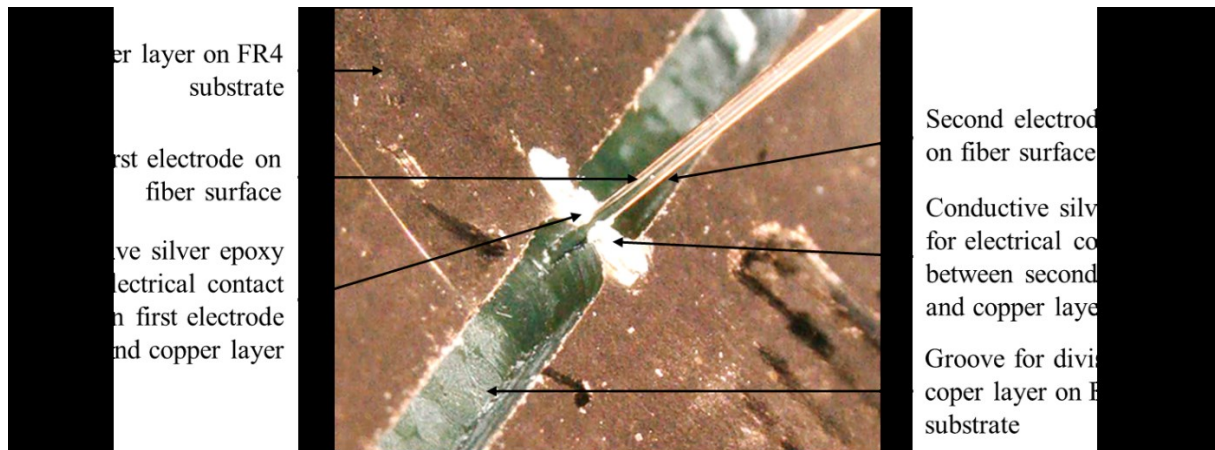


Figure 2.29: Detailed schematic representation of optrode assembly.

### 2.4.1 Establishment of electrical contacts

To enable electrophysiological recording from nervous system, electrical contacts between deposited microelectrodes and an oscilloscope need to be established. Due to a very small size of optical fiber and microelectrodes, soldering is not possible. A solution that will be presented in this chapter consists of a PCB containing 2 separate copper electrodes, such that their position corresponds to the position of 2 electrodes on fiber surface when the fiber is positioned and fixed perpendicular to the PCB surface. Electrically conductive, silver-filled, one-part epoxy adhesive with a low cure temperature (9400, MG Chemicals) is used to electrically connect electrodes on fiber surface to electrodes on PCB (Figure 2.30).

Micro manipulators are used to position optical fiber perpendicular to the PCB surface. When positioned, UV-curable epoxy is used to fix the optical fiber to the opposite PCB surface that doesn't contain electrodes. Using a micro-needle fixed on micro manipulator, a small portion of conductive silver epoxy is precisely applied to connect the electrode on fiber surface to the one on PCB. The same process is applied for establishment of electrical contacts in case of both electrodes. After application, conductive silver epoxy is cured for 30 minutes in preheated oven at temperature of 80°C. Application of silver conductive epoxy is a very sensitive process and should be done with constant microscope observation.



**Figure 2.30:** Establishment of electrical contacts between two electrodes deposited on the surface of optical fiber and two separate copper layers on PCB by application of one component silver conductive epoxy.

When applying conductive silver epoxy, it is crucial to use micro needles as applicators to ensure that only a small portion of conductive epoxy comes in contact with optical fiber. Application of larger amount of conductive epoxy will result in larger contact area between conductive epoxy and optical fiber, which usually leads to spreading of the conductive epoxy around optical fiber and mutual electrical connection of two deposited electrodes.

## 2.4.2 Coupling to a light source

To enable light delivery through above presented optrode, optical fiber needs to be coupled to a light source. As previously discussed, in case of non-implantable light sources, light source delivering light to guiding structure (optical fiber or waveguide) can be either integrated on optrode, or external. Above described assembly approach consists of external light source (fiber-coupled LED). In this case patch fiber guides light from external LED to optrode. Coupling between optrode and patch fiber is achieved by using mating sleeve (Figure 2.31). Mechanical connection between optrode and patch fiber is very tight, which would enable performing short-term optogenetic experiments in vivo in laboratory environment. However, animal movement would be limited, depending on the length of patch fiber.

Development of another approach towards integrating light source on optrode is started as a part of this work, but still needs to be completed and further improved. This approach consists of light delivery from LD through ball lens (Figure 2.32). Ball lens would enable light focusing into flat cleaved end of optical fiber (optrode). First stage of this approach is completed in this work and consists of assembly of ball lens to LD. To achieve that, small hollow cylindrical structure fitting the size of LD on one side and accepting ball lens on another is fabricated from epoxy resin. Development of such epoxy structure required designing special epoxy mold according to the width of LD (3.6 mm). Epoxy mold is fabricated by drilling small holes (diameter: 5 mm) on 5 mm thick aluminum sheet. After being fabricated, these drilled holes are filled with epoxy resin and a small iron ball, with a diameter similar to that of ball lens (5 mm), is placed on top of each hole filled with epoxy (Figure 2.33). After epoxy curing for 24h, small iron balls are removed and cylindrical epoxy structures are taken out from the mold. To enable light propagation from LD to ball lens, small hole (diameter: 3.6 mm) is drilled through these cylindrical epoxy structures. It is important to mention that prior to filling the mold with epoxy, silicon oil has to be applied on walls of holes, as well as on iron balls, to prevent sticking of the

epoxy. Length of cylindrical epoxy structure can be varied, depending on the size and focal length of ball lens.

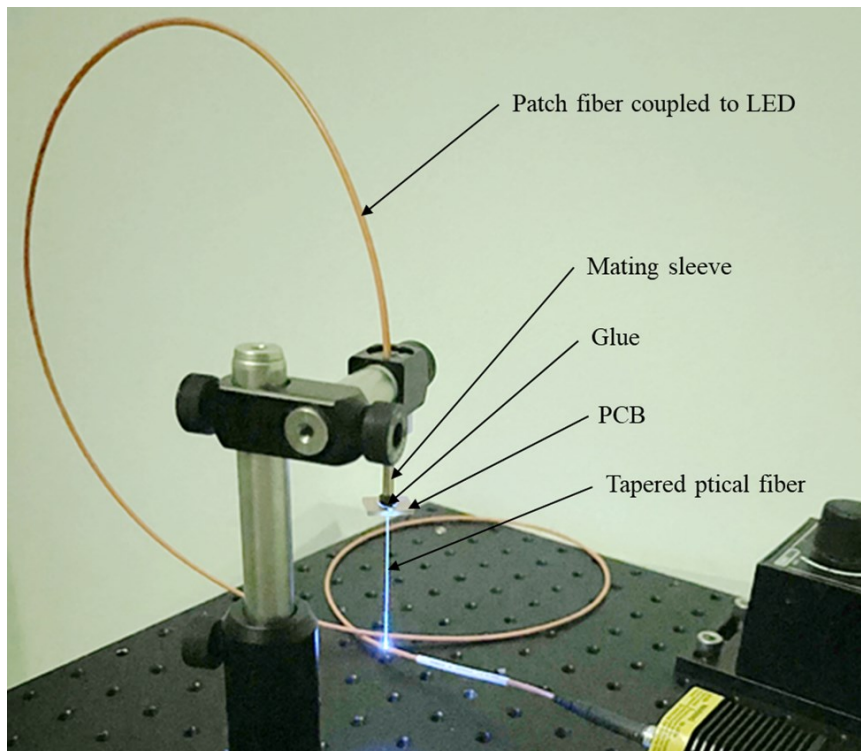


**Figure 2.31:** Fiber-based optrode, fabricated in this work, coupled to an external light source (fiber coupled LED). Coupling between flat cleaved optrode end and patch fiber is established by application of mating sleeve.

After fabrication of above described epoxy structure, it was first attached to LD. To ensure tight contact between laser diode and ball lens, diameter of hole drilled through cylindrical epoxy structure was a bit smaller than diameter of laser diode. Heating of epoxy structure enabled its expanding and placing on laser diode. Cooling led to epoxy shrinking, which resulted in very tight contact between epoxy structure and laser diode.

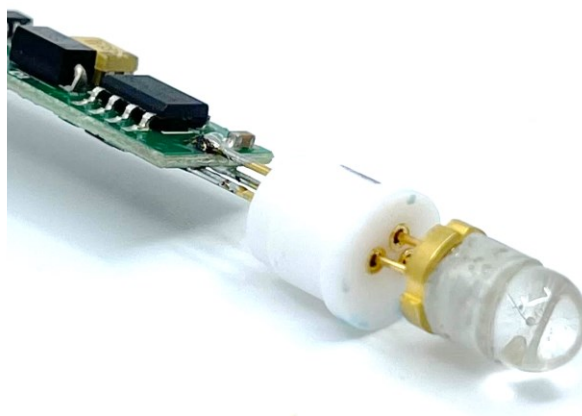


**Figure 2.32:** Ball lens attached to LD with custom fabricated hollow cylindrical epoxy structure.

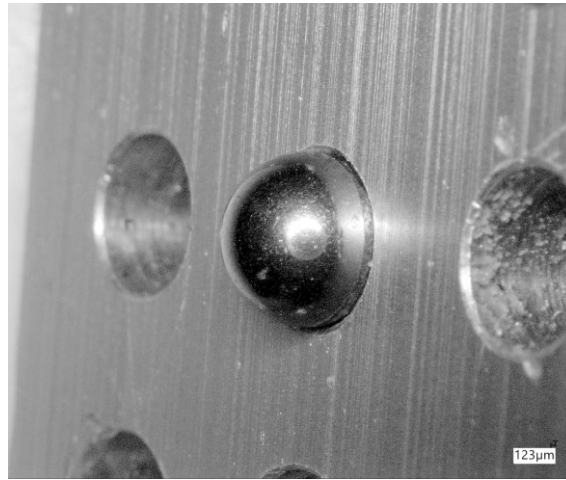


**Figure 2.33:** Epoxy mold for development of cylindrical structure for attachment of ball lens to laser diode.

When cylindrical hollow epoxy structure has been positioned on laser diode, ball lens is fixed to epoxy structure using small amount of UV curing optical adhesive. Optical adhesive is applied on the edges of curved surface (shaped with small iron balls) and after precise placement of ball lens, it is exposed to UV light for approximately 1 minute. This procedure resulted in tight fixed ball lens on defined distance from emitting site of LD. Shape of epoxy structure, positioning of ball lens, as well as whole assembly with LD are presented on Figure 2.34. This approach has to be further investigated and improved to enable precise light coupling with optrode. Furthermore, structure accepting ball lens has to be fabricated on optrode depending on focusing feature provided by ball lens.

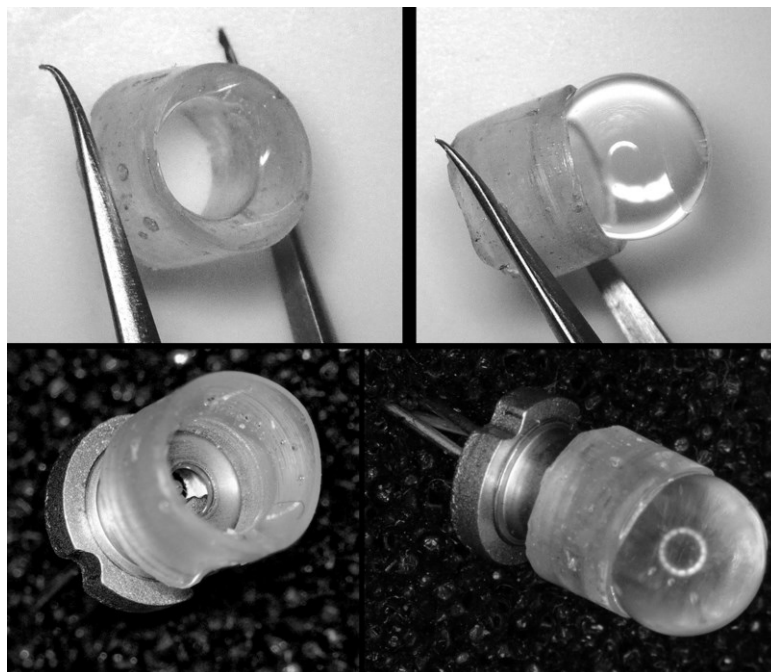


**Figure 2.34:** Epoxy structure fabricated to ensure tight fixture of ball lens to laser diode. Various images show shape of cylindrical hollow epoxy structure, ball lens positioning and assembly of the ball lens glued to epoxy structure on laser diode.



## 3 OPTICAL CHARACTERIZATION

As discussed in previous chapters, optogenetics provides the possibility to control neural activity of neurons expressing light-gated ion channels. Precise and flexible light delivery with non-invasive devices would be an ideal solution for any optogenetic experiment. However, in a typical optogenetic experiment light is delivered to targeted brain region using flat cleaved optical fiber implanted in tissue and on another end coupled to a light source. In addition to increased tissue damage, another major limitation of such approach is the lack of spatiotemporal control of light delivery. Application of tapered optical fibers as light delivery tools in optogenetic devices enables light delivery over either large tissue volumes or spatially confined sub-regions, while being less invasive than flat cleaved optical fibers.

Since requirements for spatial light distribution and light power are dependent on experimental goals, there is a need for customizable light-delivery tools. Custom made grinding setup, used for fiber tip formation in this research, provides the possibility to form tapered fiber tips with various cone angles. Customizable tapered fiber tips represent promising resource for neuroscientists looking for a new techniques to control spatial distribution of light delivered in optogenetic experiment. Fabrication process of tapered fiber tips with various cone angles is described in Chapter 2.1. In this chapter, detailed optical characterization of light delivered through cone fiber tips will be presented. The effect of cone angle on light emission profile, as well as on intensity distribution will be discussed in detail.

Prior to discussion on optical properties of tapered fibers with cone tips developed in this research, background information on light propagation through optical fiber, and the effect of tip shape on light emission profile will be presented.

### 3.1 Optical fibers for light delivery

In addition to their extensive use for light transmission in fiber-optic communication, optical fibers are also used for illumination and imaging in medical sciences. Optical fibers typically consist of inner core surrounded by cladding material with lower refractive index. A slight difference between refractive indexes of core and cladding enables total internal reflection which is responsible for light confinement inside fiber core. Modal properties of optical fiber are determined by size of core and cladding, as well as by the nature of the interface between them. Compared to a single-mode optical fibers, that enable propagation of only one type of light mode (transverse mode) at a time, multi-mode optical fibers can simultaneously propagate multiple light modes. Fiber core diameter represents the main structural difference between single-mode and multi-mode optical fibers. Core diameter of a typical single-mode optical fiber lies between 5 and 11  $\mu\text{m}$ , while cladding diameter is approximately 125  $\mu\text{m}$ . Multi-mode optical fibers have very large core diameter ranging from 50 to 200  $\mu\text{m}$ . Based on the nature of refractive index change on the core-cladding interface, optical fibers can be classified as step-index or graded-index fibers. Sharp change of the refractive index between high-index core and low-index cladding is the characteristic of step-index optical fibers, whereas gradual transition of the refractive index between core and cladding is the main feature of graded-index fibers [136].

In this work, a step-index multimode optical fiber with core diameter of 200  $\mu\text{m}$  and a cladding thickness of 10  $\mu\text{m}$  (FG200UEA ThorLabs) is used. Large core diameter enables easier coupling to a light source and, gives the possibility to achieve various illumination profiles by shaping the fiber tip using previously described mechanical grinding setup. Biocompatibility is another important feature of this optical fiber, since it consists of pure silica core surrounded by fluorine-doped silica cladding.

As long as an optical fiber has a core diameter many times larger than the carried light wavelength, simple model considering light as rays can be applied to calculate fiber properties. Until it reaches fiber tip, light is guided through optical fiber core by total internal reflection (Figure 3.1), meaning that all rays impinge core-cladding interface with incidence angle ( $\gamma$ ) equal or higher than critical angle ( $\gamma_c$ ). Knowing the refractive index of fiber core ( $n_{co}$ ) and cladding ( $n_{cl}$ ) it is possible to determine the condition for total internal refraction:

$$\gamma \geq \gamma_c = \arcsin \frac{n_{cl}}{n_{co}} \quad (3.1)$$

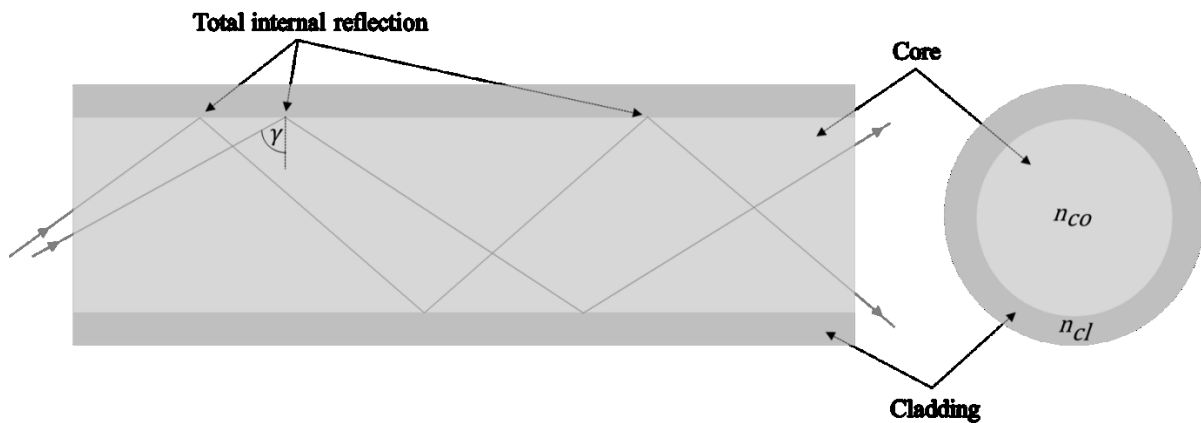


**Figure 3.1:** Light propagation through optical fiber. Requirement for total internal reflection on core-cladding surface is satisfied if light incidence angle  $\gamma$  has a value equal or higher than the critical angle ( $\gamma_c$ ).

Difference in refractive indexes of core and cladding determines not only the critical angle for total internal reflection, but also affects fiber's numerical aperture (NA). Numerical aperture is a dimensionless number that gives the information about the range of angles over which the optical fiber can accept or emit light. An optical fiber will only guide light that enters the flat cleaved fiber end within a certain range of angles, known as the fiber's acceptance cone. The half-angle of the acceptance cone is called the acceptance angle ( $\gamma_{\max}$ ) and represents the maximum incident angle, with respect to the fiber axis, for a total internal reflection in the fiber core. When it comes to light emission from flat cleaved fiber tip, NA determines maximum output angle, in respect to fiber axis, of the light exiting the fiber. Therefore, light will exit the optical fiber in a cone shape with a cone angle determined by the value of NA (Figure 3.2). Numerical aperture can be calculated based on the difference in refractive indexes between fiber core and cladding:

$$\text{NA} = \sqrt{n_{co}^2 - n_{cl}^2} \quad (3.2)$$

Refractive index of medium surrounding optical fiber doesn't affect the value of NA, but it affects the maximum input angle. In case of step-index multimode optical fiber in a given

medium, the acceptance angle, as well as the half-cone angle of the emitting light, is determined by refractive indexes of core, cladding and the surrounding medium ( $n$ ):

$$\gamma_{max} = \sin^{-1} \frac{\sqrt{n_{co}^2 - n_{cl}^2}}{n} = \sin^{-1} \frac{NA}{n} \quad (3.3)$$

The equation (3.3) is valid for straight fibers only. In case of bent fibers, more complex approximation containing bending radius can be applied. In optogenetic experiment, implanted optical fiber is fixed to be straight, thus the equation (3.3) can be applied when designing a fiber-based optrode.

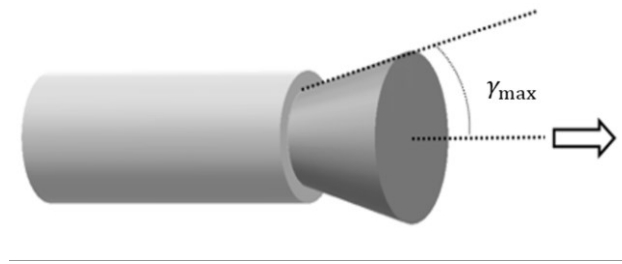


**Figure 3.2:** Light exiting flat cleaved optical fiber. Numerical aperture determines half-cone angle of exciting light.

Since numerical aperture determines capability of optical fiber to gather and/or to emit light, it represents the important characteristic when it comes to application of optical fibers for tissue illumination in optogenetic experiments. Commercial availability of multi-mode step-index optical fibers suitable for optogenetic application is limited to numerical aperture value of 0.39. To illuminate larger tissue volume, higher value of numerical aperture is required. Shaping the fiber tip represents the most convenient method for increasing numerical aperture [137, 138]. In order to achieve desired tissue illumination by shaping the fiber tip, it is crucial to understand the effect of tip geometry on cone angle of exiting light.

Prior to reaching cone tip region, light is guided through optical fiber core by total internal reflection. According to an in-depth geometrical analysis [139], there is a connection between cone angle and number of total internal reflections taking place in tapered fiber tip. Any ray entering tapered tip must impinge the interface between the fiber core and surrounding medium at an incident angle  $\gamma_i$ , which for the limit case in (3.1) becomes:

$$\gamma_i = \gamma_c - \alpha \quad (3.4)$$

Where  $\alpha$  represents the semi-angle of cone tip, measured with the respect to the fiber optical axis. Depending on the value of  $\alpha$ , the incident ray entering the tapered region can suffer either a simple refraction (without any total internal reflections), or undergoes one or multiple total internal reflections (Figure 3.3). Based on the analytical study in case of step-index multi-mode optical fiber presented in [139], the light ray impinging the cone shaped surface will not experience any total internal reflection in the tapered tip region if:

$$\alpha > \arcsin \frac{n_{cl}}{n_{co}} - \arcsin \frac{n}{n_{co}} \quad (3.5)$$

where  $n$  stands for refractive index of the medium that surrounds the cone fiber tip. In case of one or more total internal reflections, the range of  $\alpha$  values is determined according to [139]:

$$\left(\arcsin \frac{n_{cl}}{n_{co}} - \arcsin \frac{n}{n_{co}}\right)/(2m + 1) < \alpha \leq \left(\arcsin \frac{n_{cl}}{n_{co}} - \arcsin \frac{n}{n_{co}}\right)/m \quad (3.6)$$

Where  $m = 1, 2, 3 \dots N$  represents the number of total internal reflections in the cone region with semi-cone angle  $\alpha$ .

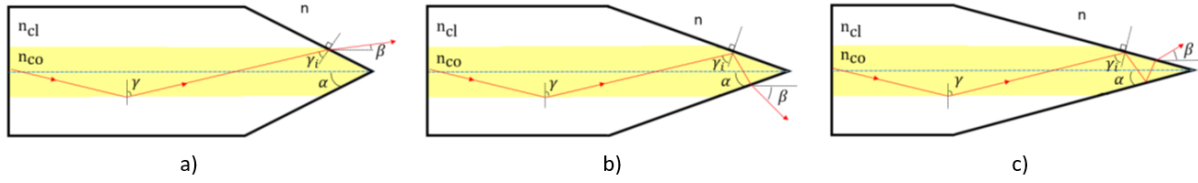


**Figure 3.3:** Incident ray entering the tapered fiber tip. Based on a size of incident angle ( $\gamma_i$ ), incident ray on the cone-shaped surface can suffer: a) simple refraction, b) one total internal reflection, c) multiple total internal reflections

According to previously presented analytical study [139], numerical aperture, as function of semi-cone angle, and can be written as:

$$NA(\alpha) = n \cos \left\{ \alpha + \arcsin \left[ \frac{n_{co}}{n} \sin \left( \arcsin \frac{n_{cl}}{n_{co}} - (2m + 1)\alpha \right) \right] \right\} \quad (3.7)$$

As already mentioned, tissue heating may alter brain function and it has to be taken into an account when choosing the optical fiber as a light delivery tool in optrode. For a given light power, optical fiber with a larger diameter reduces induced heat at the fiber tip due to an effective reduction in radiant flux density [140]. Absorption is higher for shorter wavelengths, therefore the illumination with a wavelengths above the action spectrum peak even with a higher light power is advisable, since lower tissue absorption causes a lower peak temperature increase. Furthermore, pulsed, instead of continuous, illumination dramatically reduces the induced heat in the brain tissue [57].

## 3.2 Transmission measurements

Since shaping of fiber tip leads to a change in illumination profile of emitted light compared to flat cleaved optical fiber, there is a need for power measurements independent on beam uniformity and shape, divergence angle, and entrance angle. Measurements of radiation power transmitted through flat cleaved optical fiber, as well as through optical fibers with various cone tip are carried out using an integrating sphere. This chapter provides a brief information about the concept of integrating sphere, and focuses on discussion of the effect of cone angle on overall transmitted radiant flux.

### 3.2.1 Measurement procedure

To perform measurements of the transmitted radiant power through optical fibers with cone tips, created using previously described grinding setup, integrating sphere photodiode power sensor (S140C, ThorLabs) was used. Aforementioned integrating sphere is designed and recently calibrated for wavelength ranges from 350 to 1100 nm. The operating principle of an integrating sphere relies on even spreading of incoming light by multiple reflections over the entire inner sphere surface. Incoming light strikes the reflective walls inside integrating sphere

and undergoes multiple diffuse reflections. After numerous reflections, light becomes uniformly dispersed at the sphere walls. The resulting integrated radiant power is directly proportional to the initial radiant power, and it is easily measured by the detector. Integrating sphere is an ideal instrument when it comes to power measurements of unconventional beam shape and uniformity, which is the case with cone fibers tips fabricated in this research.

To enable measurements of transmitted radiant power through optrodes with various cone angles, bare optical fiber adapter (S140-BFA, ThorLabs) has to be assembled with an integrating sphere (Figure 3.4). Bare optical fiber adapter contains V-groove for precise fiber placement, and magnetic swing arm for its reliable fixing. The adapter is fixed in contact with an integrating sphere such that one end of the optical fiber positioned in a V-groove faces the opening of integrating sphere. Fiber has to be positioned in a V-groove such that two millimetres of fiber length, measured from the cone tip end, stick out of the fiber adapter on the side facing integrating sphere, meaning that these two millimetres of the optical fiber including fiber tip are positioned inside the integrating sphere. To enable accurate and reproducible measurements, fiber positioning needs to be done the same way in each measurement. Other flat cleaved end of optrode is butt-coupled to fiber with the similar core diameter and NA (M137L02, ThorLabs) that is coupled to LED (M530F2, ThorLabs).

Fiber-coupled LED is connected to LED driver (LEDD1B, ThorLabs) that enables adjustment of output light power. In order to perform measurements of transmitted light power, integrating sphere is connected to power meter interface with external readout (PM100USB, ThorLabs). To enable precise coupling between optrode and light source, integrating sphere with bare fiber adapter is fixed on one micro block, while optical fiber coupled to LED is fixed in fiber holder and placed on another opposite micro block (Figure 3.5). Butt-coupling between flat cleaved optrode end and LED-coupled optical fiber is done with constant observation using digital microscope camera. To obtain accurate measurements, and to draw important conclusions about the effect of a cone angle on transmitted light power, coupling process needs to be reproducible. Contribution of an ambient light to measurement is avoided by performing the measurement procedure in a dark room atmosphere.

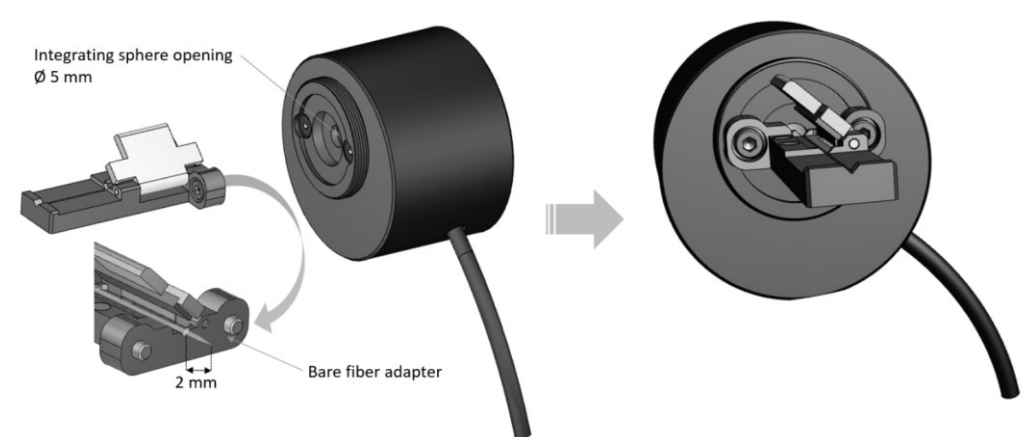


**Figure 3.4:** Mounting procedure for transmission measurements through optrodes with various cone tips using an integrating sphere. Bare fiber adapter is first mounted and fixed to the integrating sphere. Following, optrode with cone tip is placed in a V-groove of bare fiber adapter such that 2 mm of the optrode length, starting from tip end, is placed inside integrating sphere.

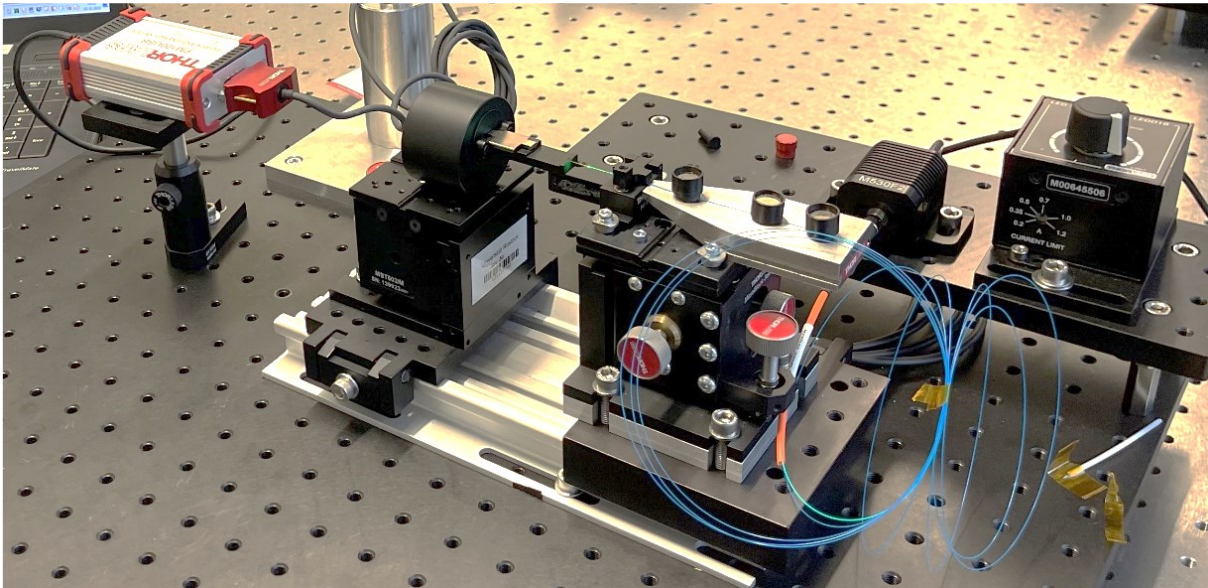


**Figure 3.5:** Custom assembled setup for transmission measurements in case of optrodes with various cone angles. Setup consists of an integrating (with mounted bare fiber adapter) sphere mounted on one microblock and LED-coupled fiber placed in a fiber groove mounted on another opposite microblock. Optrode to be tested is positioned in V-groove of bare fiber adapter such that 2 mm of optrode length (starting from tip end) are placed inside integrating sphere. Another flat cleaved optrode end is butt coupled to LED-coupled optical fiber.

Measurements were performed in case of four tapered optical fibers with cone angles ( $14^\circ$ ,  $30^\circ$ ,  $60^\circ$ , and  $90^\circ$ ) developed using previously described grinding setup with application of different polishing angles ( $7^\circ$ ,  $15^\circ$ ,  $30^\circ$ , and  $45^\circ$ ). Prior to transmission measurements, LED-coupled optical fiber is placed on a bare fiber adapter with its flat cleaved end positioned 2 mm inside an integrating sphere. By adjusting the current on LED driver, light power recorded with integrating sphere is set to 1 mW. Once adjusted current on LED driver, and thus the light power delivered with flat cleaved fiber connected to LED, is kept constant throughout the measurement procedure.

First transmission measurements are performed in case of optrode containing flat cleaved fiber tip. Following measurements are conducted with optrodes containing cone fiber tips with different angles ( $14^\circ$ ,  $30^\circ$ ,  $60^\circ$ , and  $90^\circ$ ). In case of each cone angle, as well as in case of optrode with flat cleaved fiber tip, measurements are performed on 3 different samples. To enable comparison between obtained results in case of different cone angles, each optrode is positioned the same way on bare fiber adapter. Furthermore, identical butt-coupling between the optrode and fiber connected to LED was ensured by microscope observation.

### 3.2.2 Results and discussion

Results obtained from measurements of transmitted light power using an integrating sphere are presented in Table 3.1. As already mentioned, prior to any measurement, light power transmitted through flat cleaved optical fiber coupled to LED is set to be 1 mW. Since the materials and dimensions (core and cladding) of the optical fiber coupled to LED are similar to those of optical fiber used for optrode fabrication, light transmitted through optrode with flat cleaved fiber tip can be compared to output light power from the flat cleaved fiber connected to LED. In measurement performed using a flat cleaved optrode, butt-coupling between the optrode and optical fiber connected to a light source was required. Based on measurements

performed on three different flat cleaved fiber optrodes, an average transmitted light power is estimated to be 0.714 mW. Compared to a light power delivered through optical fiber directly connected to a light source (1 mW), difference in transmitted light power is approximately 0.286 mW.

**Table 3.1:** Transmitted light power (measured with integrating sphere) in case of flat cleaved optrode, and optrodes with various cone angles: 14°, 30°, 60°, and 90°.

Samples	Transmitted light power [mW]				
	Flat cleaved fiber tip	Fiber tips with different cone angles:			
		14°	30°	60°	90°
1	0.710	0.331	0.327	0.396	0.469
2	0.702	0.304	0.359	0.407	0.462
3	0.731	0.315	0.341	0.391	0.475
Average value	0.714	0.317	0.342	0.398	0.468

Based on the results presented in Table 3.1, it can be noted that, compared to the flat cleaved optical fiber, transmitted light power decreases exponentially with cone angle reduction. According to data graphically presented on Figure 3.6, relationship between cone angle and transmitted light power can be approximated by exponential function.

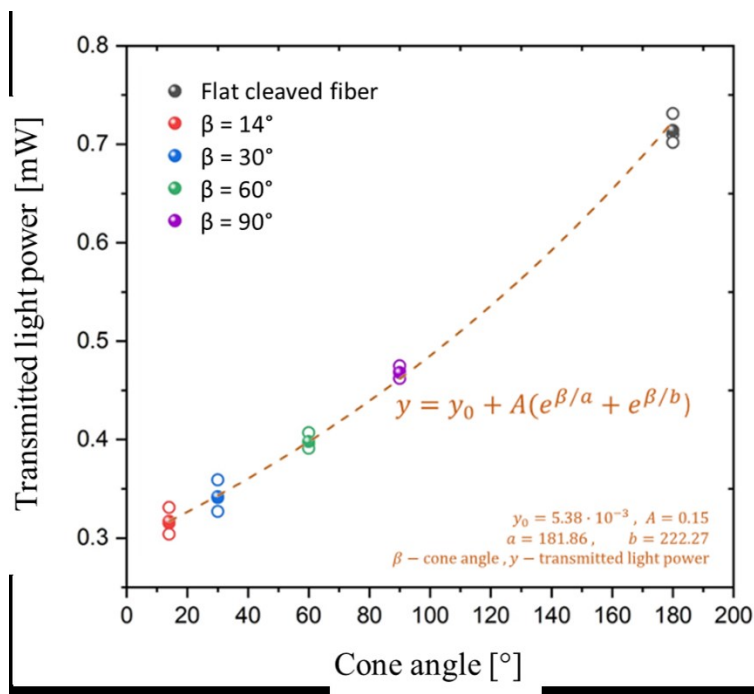


**Figure 3.6:** Dependence of overall transmitted light power on cone angle. Compared to flat cleaved optrode, an exponential decrease of transmitted light power with reduction of cone angle from 90° to 14° can be observed.

Reduction of cone angle leads to increased number of total internal reflections inside the cone tip region [129, 139, 141], which leads to shift in starting point of light emission along the fiber

axis and may contribute to reduced power of emitted light. Another factors that is may influence overall transmitted light power through optical fiber with cone tip are Fresnel reflection, surface scattering, and back reflection. Contrast between refractive index of Silica glass fiber and air results in Fresnel reflection at the optrode backside, as well as at the cone tip. Successful reduction of Fresnel reflection at the optrode back side is achieved by filling the air gap between the optrode and fiber coupled to light source with index matching gel. However this procedure cannot be applied at the interface between cone tip and air. Since the cone angle affects tapered region and influences the size of tip-air interface, it may differently contribute to losses due to Fresnel reflection depending on size of cone angle. Surface scattering may also contribute to transmission losses within the cone tip [129]. Even though cone tips are polished to obtain a smooth surface with good optical quality, sidewall roughness cannot be completely eliminated. Amplitude and spatial periodicity of sidewall roughness in tapered region influence total integrated scatter (TIS) that represents the amount of light scattered by a surface from a single reflection. Depending on total number of reflections in tapered region, TIS accumulates and contributes to overall scattering loss. Smaller cone angle leads to longer tapered region, and thus higher number of reflections inside it, which may explain the effect of cone angle reduction on transmitted light power.

To achieve light stimulation of genetically modified neurons in optogenetic experiment, one needs to deliver required light power to the stimulation site. Therefore, it is crucial to have an information about optrode's transmission capabilities. Figure 3.7 shows transmitted light power of optrodes with various cone angles compared to optrode with flat cleaved fiber tip. Compared to a flat cleaved optical fiber, light power transmitted through optrodes with cone fiber tips drops approximately 66%. As already mentioned, this can be explained by various loss processes taking place in cone tip region.

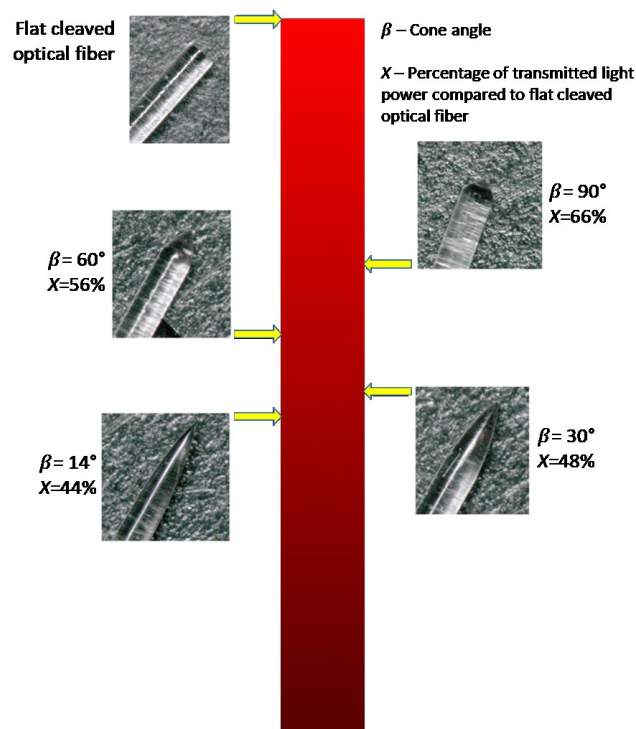


**Figure 3.7:** Comparison of transmitted light power through optrodes with various cone angles to that in case of flat cleaved optrode.



When planning an optogenetic experiment, beside power loss that arises from the coupling between the optrode and light source, optrode transmission properties need to be taken into account in order to set the sufficient power of the light source, and thus to deliver sufficient light power to the stimulation site. In addition to optrodes transmission properties, another important information, is the light emission profile. Depending on cone angle, light emission profile can be such to enable either wide volume, or very focused stimulation. In either case, a detailed characterization of emitted light power distribution is required to enable accurate optogenetic experiments. Details about dependence of emission profile on cone angle, as well as power distribution in particular emission profiles will be presented in next chapter.

### 3.3 Emission profiles

Compared to flat cleaved optical fibers, that limit illumination to relatively small and fixed tissue volume near the fiber facet, tapered fibers enable illumination of either spatially restricted or large tissue volumes. Since the tip geometry affects fibers emission properties, previously described mechanical grinding setup gives the possibility reconfigure optrode emission profile by shaping the fiber tip. Dependence of emission profile on cone angle, as well as the power distribution of emitted light in case of different emission profiles will be discussed in this chapter.

#### 3.3.1 Experimental procedure

Experimental demonstration of correlation between cone angles and emission profiles is achieved by immersing tapered fibers in a non-scattering medium, Rhodamine-6G dye water solution (R6G, Sigma Aldrich) with concentration of 1 mg/ml. The fluorescence excitation is achieved by green light (530 nm) butt-coupled into the tapered fiber. Experimental setup is presented on Figure 3.8.

Optical fiber with cone tip is positioned and fixed in a fiber holder such that cone fiber tip is placed in a container filled with Rhodamine 6G solution, while another flat cleaved end is butt coupled to LED-coupled optical fiber. To achieve accurate and reproducible butt coupling, microscope observation is required. Prior to experiment, light power on LED driver is set to 1 mW and kept constant throughout the whole experimental procedure. This experiment is done in dark room atmosphere to avoid any effect of ambient light. Liquid surface of Rhodamine solution is observed with microscope camera with optimal settings required for this experiment. Microscope images of induced fluorescence that corresponds to the tip emission profile are recorded in case of flat cleaved optical fiber, as well as in case of four tapered optical fibers with various cone angles (14°, 30°, 60°, and 90°).

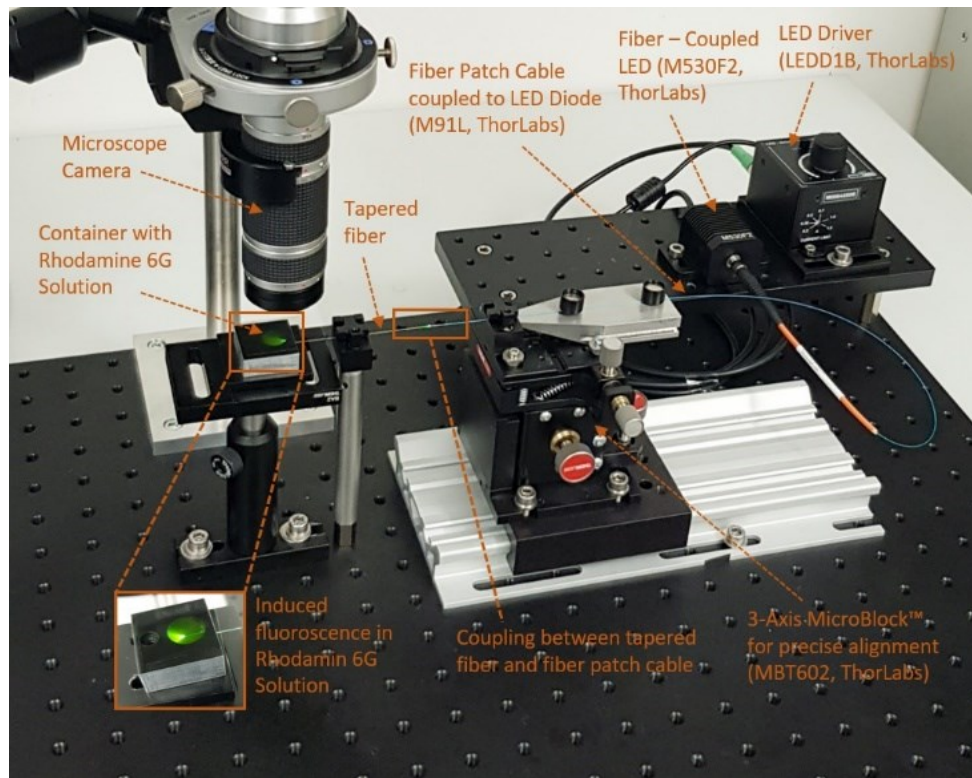


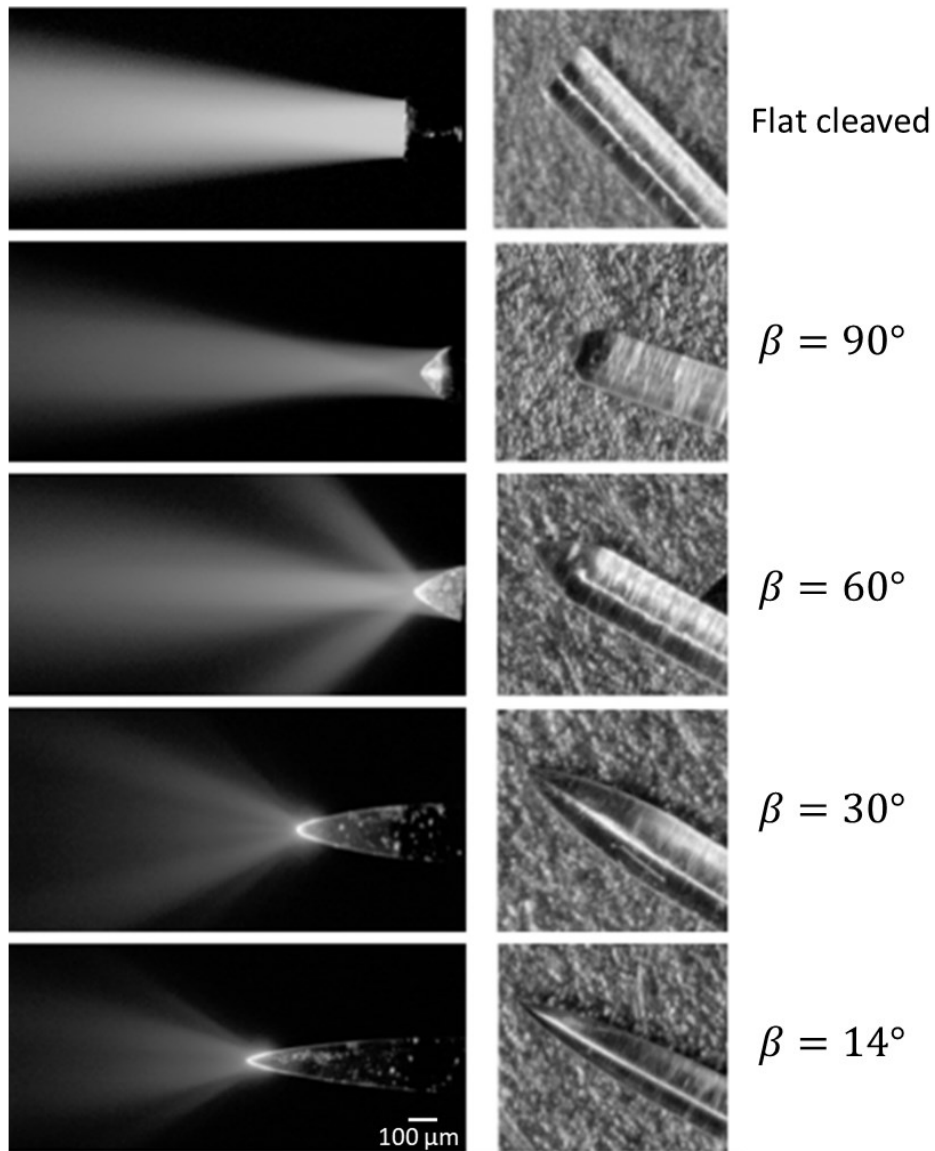
**Figure 3.8:** Custom assembled setup for observation of induced fluorescence in Rhodamine 6G water solution (1mg/ml). Cone fiber tips with various cone angles ( $14^\circ$ ,  $30^\circ$ ,  $60^\circ$ , and  $90^\circ$ ) are immersed in a container filled with rhodamine 6G water solution. Butt coupling with LED-coupled patch fiber enabled light (530 nm) delivery to optical fibers immersed in Rhodamine solution. Induced fluorescence is observed and recorded with microscope camera mounted above container with immersed fiber tips.

### 3.3.2 Results and discussion

Fluorescence profiles generated by light emitted from tapered fiber tips with various cone angles ( $\beta$ ), as well as from flat cleaved optical fiber immersed in Rhodamine 6G solution are presented on Figure 3.9. As mentioned previously, light rays are guided through fiber core by total internal reflection until they reach tapered region. Each ray reflection in tapered region leads to increase in its propagation angle, with respect to the fiber optical axis, by an amount equal to the value of cone angle ( $\beta$ ) [96]. When the total internal reflection is lost, light ray leaves the cone tip and radiates into the surrounding medium.

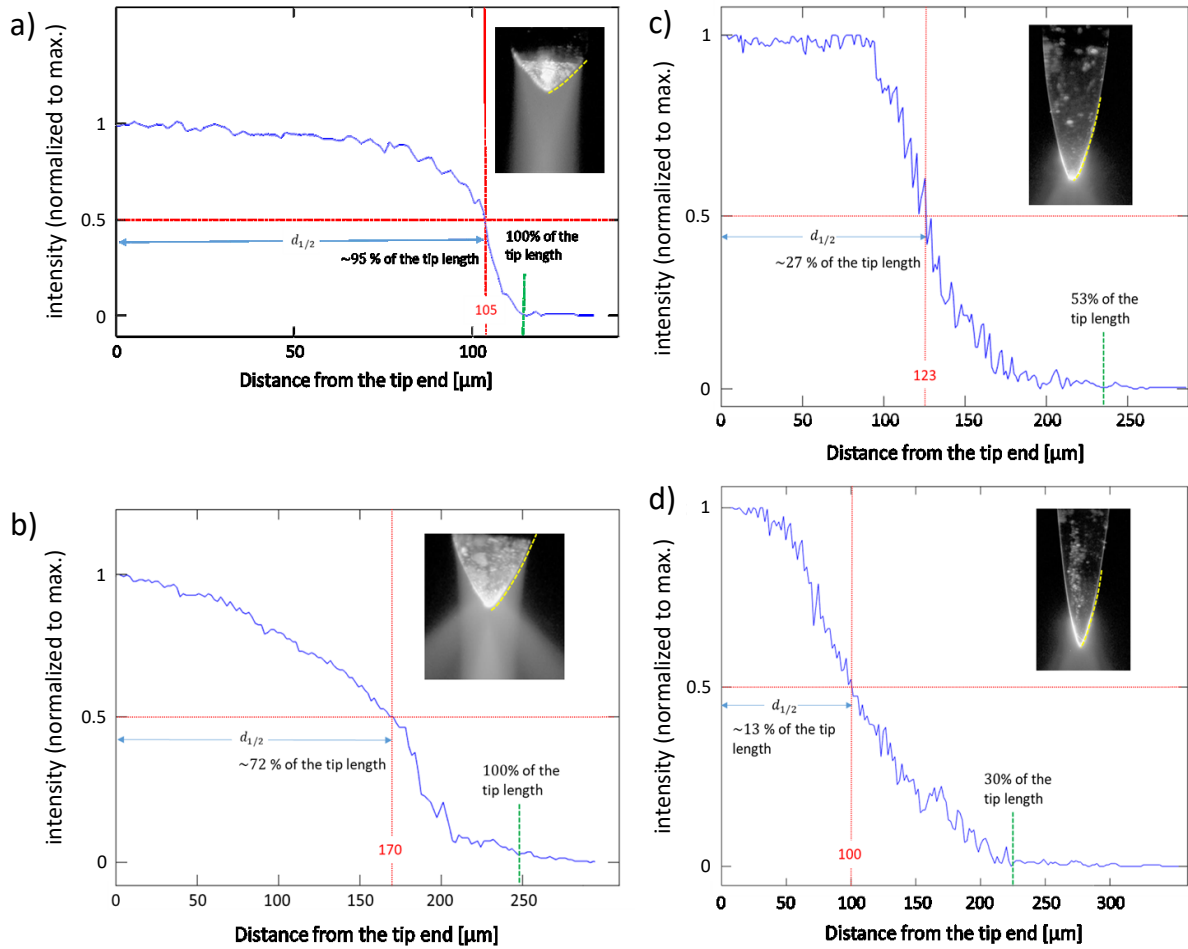
Compared to flat cleaved fiber tip, fiber tips with cone angles equal or less than  $60^\circ$  offer the possibility of spatially extended illumination (

Figure 3.9). Furthermore, fiber tip with  $90^\circ$  cone angle enables spatially restricted illumination close to fiber tip with a focusing feature. While light beam diverges immediately after leaving flat cleaved fiber tip, onset of beam divergence is located much further from tip end in case of  $90^\circ$  cone tip angle.



**Figure 3.9:** illumination profiles provided by flat cleaved optical fiber, and by optical fibers with various cone angles ( $14^\circ$ ,  $30^\circ$ ,  $60^\circ$ , and  $90^\circ$ ) recorded as induced fluorescence in Rhodamine 6G water solution.

Taper emitting length ( $d_{1/2}$ ), defined as the extent of taper light emitting segment [96] measured from the tip end at which fluorescence intensity decreases to half of its value at the tip end, can be determined based on microscope images of induced fluorescence in Rhodamine 6G water solution (Figure 3.9). Intensity profiles corresponding to various positions and directions on grey scale microscope images of induced fluorescence can be obtained in MATLAB by application of *improfile* function. Normalized fluorescence intensity profiles along the taper light emitting segment, starting from the tip end (maximum intensity), of four optical fibers with different cone angles ( $14^\circ$ ,  $30^\circ$ ,  $60^\circ$ ,  $90^\circ$ ) are presented on Figure 3.10.



**Figure 3.10:** Light emission from cone fiber tips in taper region. Normalized fluorescence intensity profiles, obtained by image analysis in MATLAB, along taper light emitting segment, starting from the tip end (maximum intensity), optical fibers with different cone angles (14°, 30°, 60°, 90°). Taper emitting length ( $d_{1/2}$ ), is determined as an extent of taper light emitting segment (measured from the tip end) at which fluorescence intensity decreases to half of its value at the tip end.

Intensity distribution of induced fluorescence (Figure 3.10) suggest that increase of cone angle leads to larger light emitting segment of the taper, as well as to larger taper emitting length. In case of fiber tip with 90° cone angle light is emitted from entire-tip length, with estimated taper emitting length of approximately 95%. Decreasing cone angle to 60° doesn't affect light emitting segment of the taper, but leads to reduction of taper emitting length to approximately 72%. Further reduction of cone angle to 30° and 14° is followed by decrease in both, light emitting segment and taper emitting length. Taper emitting length decreases to approximately 27% and 13% in case of fiber tips with cone angle of 30° and 14°, respectively.

Reduction of cone angle followed by reduction of output zone along the length of a specific taper can be explained by mechanism of total internal reflection in tapered region. Range of cone angles ( $\beta$ ) associated with different number of total internal reflections in tapered region is calculated according to (3.6), and presented in Table 3.2. Results presented in Table 3.2 are in agreement with observed fluorescence profiles (Figure 3.9), and indicate the absence of TIR in tapered region of two fiber tips with cone angles of 90° and 60°. This explains light emission along entire taper of these fiber tips. Furthermore, reduction of light emitting segment to 53% and 30% of entire taper length in case of fiber tips with cone angles of 30° and 14°, respectively, can be explained by increased number of TIRs taking place in taper region. It is important to

mention that equation (3.6) assumes linear taper, whereas the real structure has a modestly parabolic shape, which can slightly affect the results. Besides TIR, other events, described in Chapter 3.2.2 may contribute to difference in taper emitting length in case of fiber tips with different cone angles.

**Table 3.2:** Calculated range of cone angles ( $\beta$ ) for different number of total internal reflections (TIRs). Calculations are performed using equation (3.6) based on theoretical study presented in Chapter **Fehler!** *Verweisquelle konnte nicht gefunden werden.*

Number of TIRs in taper region	Range of cone angles (calculated using (3.6))
0	$\beta > 40^\circ$
1	$13^\circ < \beta \leq 40^\circ$
2	$8^\circ < \beta \leq 20^\circ$

Since previously presented illumination profiles are obtained by induced fluorescence in Rhodamine 6G water solution, absolute light intensity values are expected to significantly differ from those in tissue medium. Therefore, only a relative comparison of the cone angle effect on taper emitting length and light emitting taper segment was discussed in case of fiber tips with four different cone angles. The same applies when it comes to intensity distribution along illumination profiles.

Figure 3.11 shows normalized intensity profiles of induced fluorescence (obtained by image analysis in MATLAB), starting from the tip end, along the fiber optical axis, in case of flat cleaved optical fiber and tapered fibers with different cone angles. Compared to flat cleaved optical fiber, tapered fibers with cone angles of  $90^\circ$  and  $60^\circ$  show similar behavior of intensity reduction along fiber axis, except a focusing feature observed in case of tapered fibers with cone angles of  $90^\circ$  and  $60^\circ$ . However, tapered fibers with cone angles of  $30^\circ$  and  $14^\circ$  show a significantly different behavior of intensity distribution along fiber axis. Starting from the tip end, intensity decreases as soon as the light leaves fiber tip, and reduces to half of its maximum value after approximately  $430 \mu\text{m}$  and  $170 \mu\text{m}$  in case of  $30^\circ$  and  $14^\circ$  cone angles, respectively. Intensity drop to half of its maximum value is observed approximately one millimeter from tapered tip with  $60^\circ$  cone angle, whereas the same intensity reduction is reached approximately two millimeters from flat cleaved fiber tip, as well as from the tapered tip with  $45^\circ$  cone angle.

Drastic difference in emission profiles should be expected if these optical fibers are implanted in brain tissue. Due to scattering and absorption in brain tissue, penetration depth, as well as beam width are expected to vary significantly compared to these obtained from induced fluorescence in Rhodamine 6G water solution.

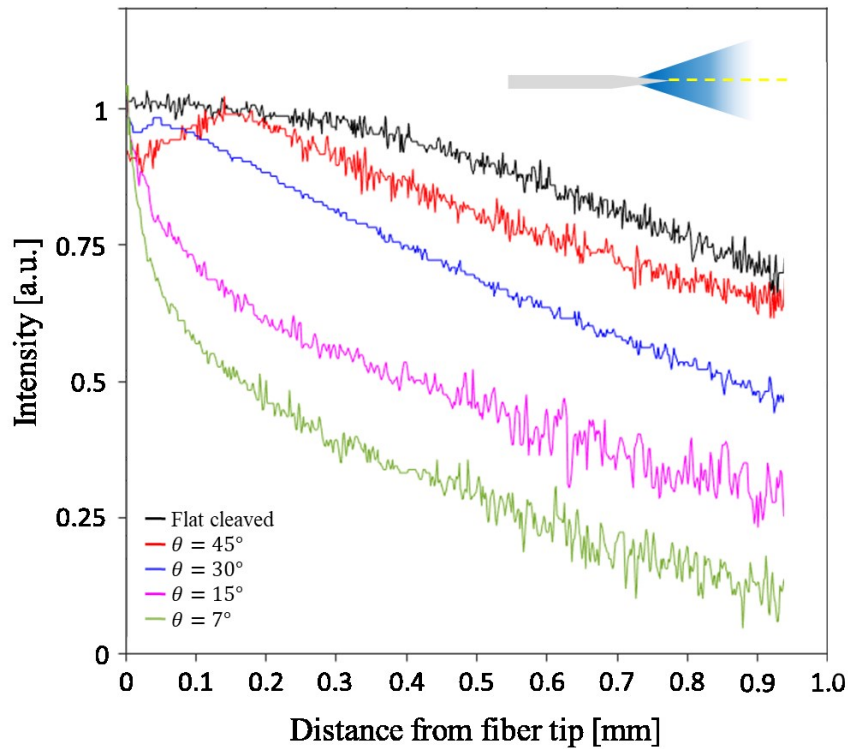


**Figure 3.11:** normalized intensity profiles of induced fluorescence (obtained by image analysis in MATLAB), starting from the tip end, along the fiber optical axis, in case of flat cleaved optical fiber and tapered fibers with different cone angles ( $14^\circ$ ,  $30^\circ$ ,  $60^\circ$ , and  $90^\circ$ ).

### 3.3.3 Estimation of emission profile in brain tissue

Previously presented results describe light propagation in Rhodamine 6G water solution (1mg/ml). Since optical characteristics of medium (refractive index, absorption and scattering) influence light propagation and intensity distribution along emission profile, it should be expected that intensity distribution in brain tissue would significantly differ from that obtained in Rhodamine 6G water solution.

Brain tissue is mostly considered as turbid medium (i.e., cloudy and/or opaque) [142] with characteristic heterogeneous structures and corresponding spatial variations of optical properties. Density and spatial distribution of these fluctuations influence light scattering in tissue. Brain tissue, as a turbid medium, is successfully modeled as a system consisting of homogeneous background medium with randomly distributed scattering and absorption particles [142].

Due to absence of absorption, significant portion of light delivered to tissue (turbid medium) undergoes multiple scattering, producing diffuse light field. Despite the fact that actual tissue is much more complex than above described turbid medium, simple model of a turbid medium has proven to give satisfactory results when it comes to light distribution in brain tissue. In this section, model based on Kubelka-Munk approach for light propagation in diffuse scattering media [143, 144] will be applied as a MATLAB to calculate and graphically present irradiance profile of flat cleaved optical fiber used in this research. The results will be compared with emission profile corresponding to induced fluorescence of flat cleaved optical fiber placed in Rhodamine 6G water solution. Based on difference in intensity distribution between calculated values for brain tissue, using Kubelka-Munk approach, and a distribution obtained from image

processing of microscope image presenting induced fluorescence in Rhodamine 6G in case of flat cleaved optical fiber, one can get an idea of possible emission profiles in brain tissue in case of various cone fiber tips.

Since brain tissue (refractive index ( $n_b \approx 1.36$  [142])) is not transparent to visible light, limited light penetration and confinement in deeper brain structures represent the main challenge for optogenetics. Due to light scattering and absorption, it is very hard for larger amount of light to reach deep brain structures. Beer-Lambert equation [144] is often used for determination of light attenuation after propagation in tissue:

$$I(z) = I_0 e^{-\mu_t(\lambda)z} \quad (3.8)$$

where,  $I(z)$  represents light intensity after a traveled distance  $z$ ,  $I_0$  is the initial intensity, and  $\lambda$  stands for light wavelength. In Equation (3.8)  $\mu_t$  is the extinction coefficient, which can be calculated using the absorption ( $\mu_a(\lambda)$ ) and scattering ( $\mu_s'(\lambda)$ ) coefficient in biological tissue:

$$\mu_t = \mu_a(\lambda) + \mu_s'(\lambda) \quad (3.9)$$

It is obvious from (3.9) that both coefficients ( $\mu_a(\lambda)$  and  $\mu_s'(\lambda)$ ) depend on the wavelength  $\lambda$ . Due to anisotropic light scattering in tissue, value of  $\mu_s'$  also depends on anisotropic factor ( $g$ ):

$$\mu_s' = \mu_s(1 - g) \quad (3.10)$$

Beside the fact that tissue scattering and absorption coefficients are wavelength dependent, they also vary between different brain regions (white and grey matter). Although it is hard to precisely estimate these values, and they vary among different literature, most used values of anisotropic factor and coefficients of scattering and absorption, for estimation of light propagation in brain tissue, in case of  $\lambda \sim 500$  nm are listed in Table 3.3 [142, 144].

Knowing values of fiber numerical aperture, and optical properties of brain tissue, it is possible to estimate effective activation volume near the fiber tip. Although there are numerous definitions of activation volume, it is mostly defined as the brain volume in which the achieved flux density is equal or greater than the lowest value required for activation of genetically modified neurons.

For example, in case of ChR2 that volume corresponds to tissue volume where the value of flux density is at least  $1 \text{ mW/mm}^2$  [44, 52, 143, 145]. The size of activation volume is dependent on fiber diameter, as well as on the tip shape, but in any case it can be enlarged by increasing the light intensity at the fiber tip. While increasing light intensity leads to a larger activation volume, it may lead to tissue damage caused by overheating. In some studies, flux density of around  $300 \text{ mW/mm}^2$  at the fiber tip was reported to be safe [146], while in another studies tissue damage due to overheating was reported at values of flux density above  $100 \text{ mW/mm}^2$  [65].

**Table 3.3:** Values of scattering ( $\mu_s$ ) and absorption ( $\mu_a$ ) coefficients, and anisotropic factor ( $g$ ) for brain tissue in case of white and grey matter table [142, 144].

Parameters	Tissue type	Values
$g$	White matter	0.8
	Grey matter	0.88
$\mu_s$	White matter	420 cm <sup>-1</sup>
	Grey matter	110 cm <sup>-1</sup>
$\mu_a$	White matter	1 to 2 cm <sup>-1</sup>
	Grey matter	0.17 to 20 cm <sup>-1</sup>

For better understanding of light propagation through brain tissue, two-dimensional representation of an irradiance profile can be calculated using model described by Foutz et al. [142, 143]. This model describes distribution of light exciting optical fiber, and starts from the fact that light at each point in space ( $I$ ) is defined by the source light irradiance ( $I_0$ , at the fiber tip center) and light transmittance between that point and the source ( $T$ ):

$$I(\mathbf{r}, \mathbf{z}) = T(\mathbf{r}, \mathbf{z})I_0 \quad (3.11)$$

where  $r$  stands for the radial distance, while  $z$  represents the height in a cylindrical coordinate system with the origin at center of the optical fiber tip. Transmittance is wavelength dependent and can be presented as the product of linear components:

$$T(\mathbf{r}, \mathbf{z}) = G(\mathbf{r}, \mathbf{z})C(\mathbf{z})M(\mathbf{r}, \mathbf{z}) \quad (3.12)$$

where  $G$  and  $C$  represent the Gaussian distribution of light emitted by optical fiber, and the conical spreading of unfocused light respectively, while  $M$  represents scattering and absorption of light according to the Kubelka-Munk theory of light propagation [144, 147]. Emitted from optical fiber, light spreads conically, with a divergence half angle ( $\gamma_{max}$ ) which depends on the tissue refractive index ( $n_t$ ) and the numerical aperture of the optical fiber (NA):

$$\gamma_{max} = \sin^{-1} \left( \frac{NA}{n_t} \right) \quad (3.13)$$

Knowing the optical fiber core radius ( $D_0$ ), equation for spreading of the light cone radius ( $D$ ) at height  $z$  is given as:

$$D(\mathbf{z}) = D_0 + z \tan(\gamma_{max}) \quad (3.14)$$

According to energy conservation law, light divergence leads to irradiance decrease. Considering geometric effects independently, radiant power ( $P$ ) is constant at all distances and is equal to the product between the irradiance and the illuminated surface area:

$$P = I(\mathbf{z})\pi D(\mathbf{z})^2 = I_0\pi D_0^2 \quad (3.15)$$

where  $I$  stands for the irradiance at distance  $z$  from the fiber tip. Therefore, the transmittance due to conical spreading ( $C$ ) can be written as [143]:



$$C(z) = \left[ \frac{D_0}{D(z)} \right]^2 \quad (3.16)$$

The Gaussian distribution of the light ( $G$ ) emitted by the optical fiber [148] can be approximated as a transmittance:

$$G(r, z) = \frac{1}{\sqrt{2\pi}} \exp \left\{ -2 \left[ \frac{r}{D(z)} \right]^2 \right\} \quad (3.17)$$

Scattering and absorption properties of the tissue affect the light distribution. In order to capture these effects, there is a need for implementation of Kubelka-Munk model of light propagation in diffuse scattering medium [142]:

$$M(r, z) = \frac{b}{a \sin h(bS\sqrt{r^2+z^2}) + b \cos h(bS\sqrt{r^2+z^2})} \quad (3.18)$$

$$a = 1 + K/S \quad (3.19)$$

$$b = \sqrt{a^2 - 1} \quad (3.20)$$

where  $S$  and  $K$  represent scattering and absorption coefficients per unit thickness ( $\text{mm}^{-1}$ ) respectively. According to Gradinaru et al. [52], coefficients for scattering ( $S = 7.37 \text{ mm}^{-1}$ ) and for absorbance ( $K = 0.125 \text{ mm}^{-1}$ ) were calculated from the fit of light transmission data acquired from rodent brain slices. This model assumes that sample is planar, optically homogenous medium which is illuminated normal to the sample surface with diffuse monochromatic light. Reflection and absorption are assumed constant over the illuminated area.

Experimental results of directly measured transmission fraction of total transmitted blue light as a function of distance through rat and mouse cortical tissue [20] showed that after passing through  $100 \mu\text{m}$  of cortical tissue, total transmitted light power was reduced by 50%. Results obtained in these experiments were similar in case of rat and mouse brain tissue and corresponded very well with the Kubelka-Munk model for diffuse scattering media (3.18) with best fit values for  $S$  of  $11.2 \text{ mm}^{-1}$  for mouse and  $10.3 \text{ mm}^{-1}$  for rat [20]. Since previous studies showed that in mammalian brain tissue, transmission loss from scattering is much greater than absorption loss for wavelengths ranging from 400 to 900 nm [149, 150], to simplify the model it is often assumed that no absorption occurs.

Two-dimensional (2D) intensity distribution, calculated using MATLAB script [144] based on Kubelka-Munk model is often applied to predict light propagation through brain tissue in case of flat cleaved optical fibers with various core size and numerical aperture. Due to a fact that emission profiles of induced fluorescence in Rhodamine 6G water solution (1mg/ml) are recorded using microscope camera positioned above the container (**Fehler! Verweisquelle konnte nicht gefunden werden.**), peak intensity at defined distance from tip end on such image doesn't correspond to peak intensity on beam profile at same distance. Thus, details of intensity distribution obtained from such image cannot be compared to 2D intensity distribution in brain tissue obtained from MATLAB script based on Kubelka-Munk model, which actually represents intensity distribution on 2D plane parallel to fiber optical axis and positioned at fiber core center. However, such 2D profile should help to understand overall difference between light propagation in brain tissue and in Rhodamine 6G water solution. Furthermore, difference in beam width, and light penetration depth in brain tissue compared to that in Rhodamine 6G

solution in case of flat cleaved fiber can help in estimation of expected beam width and light penetration depth in case of various cone tips implanted in brain tissue.

Figure 3.12 shows calculated 2D emission profile of light ( $\lambda \approx 530$  nm) emitted from flat cleaved optical fiber in rodent brain tissue, and recorded emission profile from induced fluorescence caused by light ( $\lambda \approx 530$  nm) emitted from flat cleaved optical fiber immersed in Rhodamine 6G water solution. Two-dimensional emission profile is obtained by application of MATLAB script based on Kubelka-Munk model with parameters similar to that of optical fiber immersed in Rhodamine 6G water solution (core radius:  $100 \mu\text{m}$ ,  $\text{NA}=0.22$ ). Previously listed values for refractive index ( $n_b = 1.36$ ), and coefficients of absorption ( $K = 0.125 \text{ mm}^{-1}$ ) and scattering ( $S = 7.37 \text{ mm}^{-1}$ ) in rodent brain tissue are used in calculation.

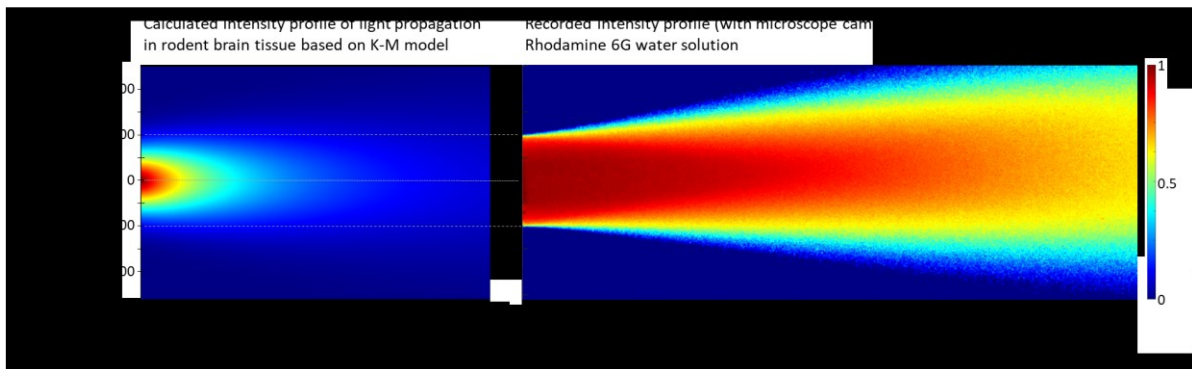


**Figure 3.12:** (left) Calculated emission profile (based on K-M model) of light propagation in rodent brain tissue.. (right) Emission profile recorded from induced fluorescence in Rhodamine 6G water solution. In both cases, flat cleaved optical fiber (core radius:  $100 \mu\text{m}$ ,  $\text{NA}=0.22$ ) represented the light source.

As expected, light emission in brain tissue drastically differs from that observed in water. Although light emission in brain tissue was calculated according to Kubelka-Munk theory of light propagation in diffuse scattering medium, according to previous publications [143, 144], it agrees well with experimental results and should be used for prediction of light propagation in optogenetic experiments with rodent brain.

### 3.4 Beam profiles

Previously presented emission profiles obtained by induced fluorescence in Rhodamine 6G water solution give an overall idea about beam shape and divergence, and they are very useful when it comes to comparison between extents of spatial illumination between fiber tips with various cone angles. However, an information about spatial intensity distribution, obtained from such emission profiles, is not reliable since they are recorded using microscope camera positioned above the container filled with Rhodamine 6G water solution containing full immersed optical fiber tip. Thus, peak intensity at defined distance from tip end on such image doesn't correspond to peak intensity on beam profile at same distance. More detailed information about spatial intensity distribution can be obtained from beam profiles at various distances from fiber tip end.

### 3.4.1 Experimental procedure

Beam profiles at various distances from fiber tip end are obtained in case of flat cleaved fiber tip, as well as for cone fiber tips. Experimental setup, presented on

Figure 3.13, enables recording of beam profiles in air at different distances from fiber tip end. The setup consists of horizontally mounted linear translation stage (LTS150 ThorLabs) with fixed and free plates. Fixed plate is not controlled by linear stage interface and contains fixed microscope camera objective and a fixed micro block containing mounted glass diffuser with a fine grit of 1500 (DG10-1500 ThorLabs). Another free plate, controlled with linear stage interface, contains fixed fiber holder and fixed micro block with mounted optical fiber coupled to LED light source. Prior to experiment, optrode is placed and fixed in fiber holder on free plate, such that fiber tip (cleaved or tapered) faces rough side of glass diffuser. On another end, optrode is then butt coupled to fiber-coupled LED. Precise coupling is achieved with controlled movements of LED coupled fiber enabled by micro block, and constantly observed with digital microscope camera.

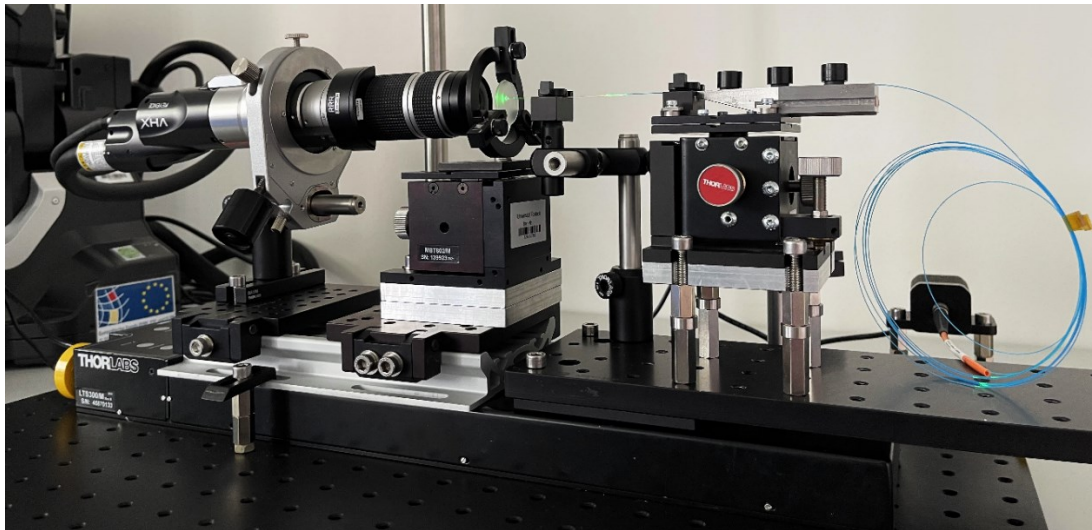


**Figure 3.13:** Custom assembled setup for observation and recording of beam profiles in case of light emitted from flat cleaved fiber tip and tapered fiber tips with various cone angles.

Depending on movement direction of a free plate, controlled remotely using PC, optrode tip can be moved either towards or away from the glass diffuser. Optrode is first moved towards glass diffuser and kept in a position where the fiber tip gently touches the rough surface of glass diffuser (starting position). Next, optical microscope camera, facing polished side of glass diffuser, is positioned to obtain a very sharp image of diffuse pattern from light exiting optrode tip. Optrode is then moved away from glass diffuser in steps of  $2\ \mu\text{m}$ , and an image of diffuse pattern is recorded at each position. Experimental procedure is done in a dark room to avoid any effect of the ambient light. Intensity of a light source is kept constant (1 mW) throughout the experiment.

### 3.4.2 Results and discussion

To gain a better understanding of the effect of cone angle on shape and intensity distribution of light delivered by optrode, microscope images of output beam profiles are obtained at various distances from the tip end (Figure 3.14). Based on microscope images presented on Figure 3.14, it can be noted that cone angle affects beam divergence, as well as the intensity distribution, and therefore determines illuminated volume. It is important to mention that microscope images presented on Figure 3.14 correspond to beam profiles at different distances from tip end placed in air. Absorption and scattering in brain tissue leads to changes in beam divergence and intensity distribution [151]. However relative comparison between flat cleaved fiber tip and cone tips with different angles positioned in the same medium should not be much affected by the characteristics of the surrounding medium.

Illumination volume depends on beam width near cone tip, as well as on beam divergence and tissue optical properties. According to beam profiles at various distances from tip end, fiber tip with cone angle of  $90^\circ$  provides most uniform illumination volume through tissue depth compared to other cone tips with smaller angles ( $60^\circ$ ,  $30^\circ$ , and  $14^\circ$ ). Decrease of cone angle leads to wider illumination volume, and intensity distribution specific to a certain cone angle. Based on microscope images of beam profiles, it can be noted that tip cone angle affects not only the size of illumination volume, but also its shape.

The shape of illumination volume in case of optical fiber with  $90^\circ$  cone angle doesn't differ much from that of flat cleaved optical fiber. However, optical fiber with  $90^\circ$  cone angle offers much wider illumination volume, which increases with distance from fiber tip end. Illumination volume obtained from fiber cone tips with angles smaller than  $90^\circ$  is less uniform with most of intensity located in the center of emission profile.

Further analysis of beam profiles is conducted using MATLAB Beam profiler [152]. Estimated values of beam width at various distances from tip end in case of flat cleaved optical fiber and fiber tips with various cone angles are presented in Table 3.4.

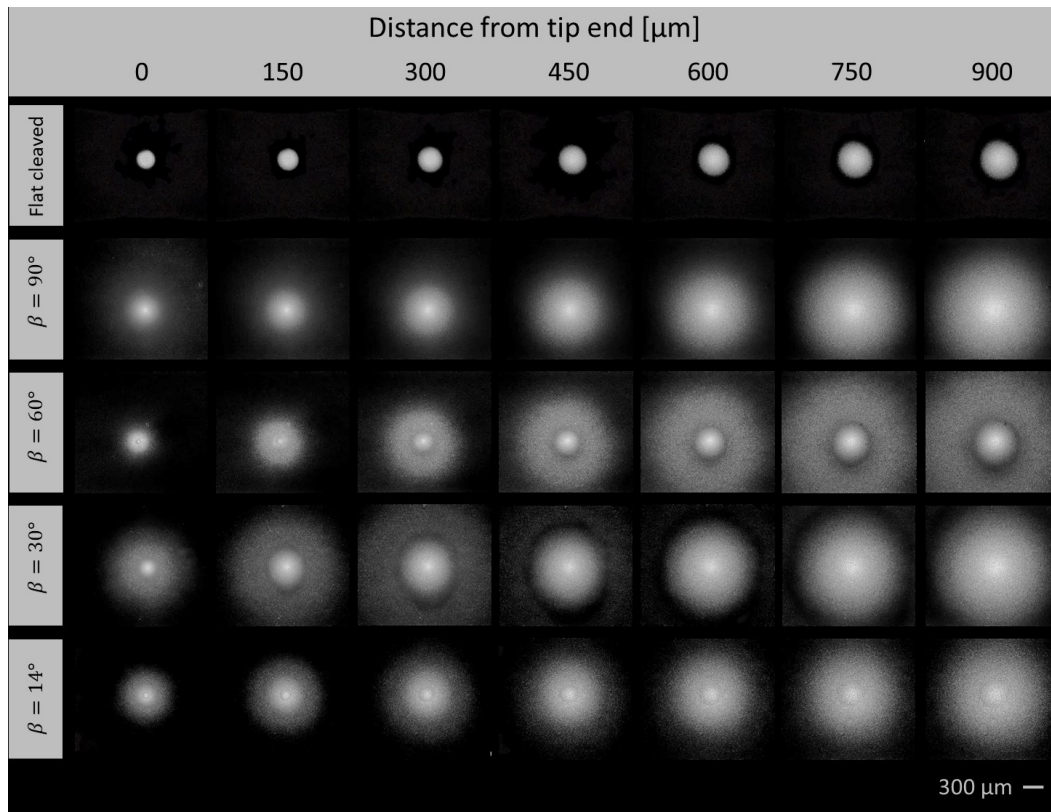


**Figure 3.14:** Beam profiles at various distances from tip end in case of flat cleaved optical fiber and tapered fibers with different cone angles. Profiles are recorded (with microscope camera) as light patterns on glass diffuser.

**Table 3.4:** Estimated values of beam width (using MATLAB Beam profiler [152]) at various distances from tip end in case of flat cleaved optical fiber and fiber tips with various cone angles.

Distance from the tip end [ $\mu\text{m}$ ]	Beam width in air [ $\mu\text{m}$ ]				
	Flat cleaved fiber	Cone angle			
		$\beta = 90^\circ$	$\beta = 60^\circ$	$\beta = 30^\circ$	$\beta = 14^\circ$
0	244	656	625	1111	694
150	269	775	831	1553	1019
300	319	944	1162	1935	1295
450	369	1126	1550	2050	1418
600	413	1335	1896	1494	1468
750	469	1500	2230	1537	1565
900	506	1700	2625	1768	1706
1050	567	1900	2974	2000	1846

For better comparison, results from Table 3.4 are presented graphically on Figure 3.15. Beam shape in case of  $90^\circ$  cone angle is comparable to that in case of flat cleaved optical fiber. However, compared to flat cleaved optical fiber, beam width at defined distance from fiber tip end is approximately three times larger in case of fiber tip with cone angle of  $90^\circ$ . Starting from fiber tip end up to distance of approximately  $700 \mu\text{m}$ , beam divergence significantly differ

among different cone angles. However, at a distance equal or larger than  $700\ \mu\text{m}$  from tip end, difference in width of light beams emitted in air by optical fibers with cone angles of  $90^\circ$ ,  $30^\circ$  and  $14^\circ$  becomes negligible. Compared to flat cleaved optical fiber, fibers with cone tips offer much larger illumination volume near tip end, but with different intensity distribution.

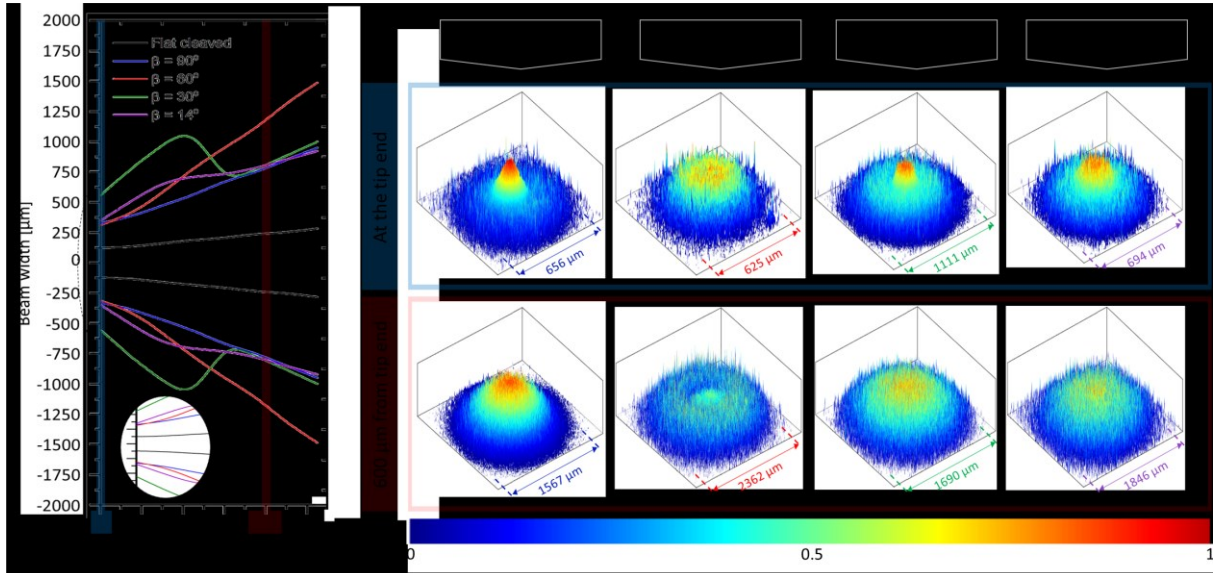


**Figure 3.15:** (left) Beam width of light emitted by flat cleaved optical fiber, and by optical fibers with various cone angles ( $14^\circ$ ,  $30^\circ$ ,  $60^\circ$ , and  $90^\circ$ ). (right) Comparison of beam profiles at distance of  $800\ \mu\text{m}$  to those at fiber tip in case of tapered fibers with various cone angles.

When calculating illumination volume from tapered fiber tip, it is important to take into an account side illumination that can be observed only on emission profiles. Schematic illustration of the procedure for calculation of illumination volume up to certain distance from fiber tip is presented on Figure 3.16. As already mentioned, in optogenetics, activation volume represents illuminated tissue volume with flux density equal or higher than minimum value required for activation of certain genetically modified neurons. Thus, activation volume is expected to be only a part of illumination volume, where these requirements are met.

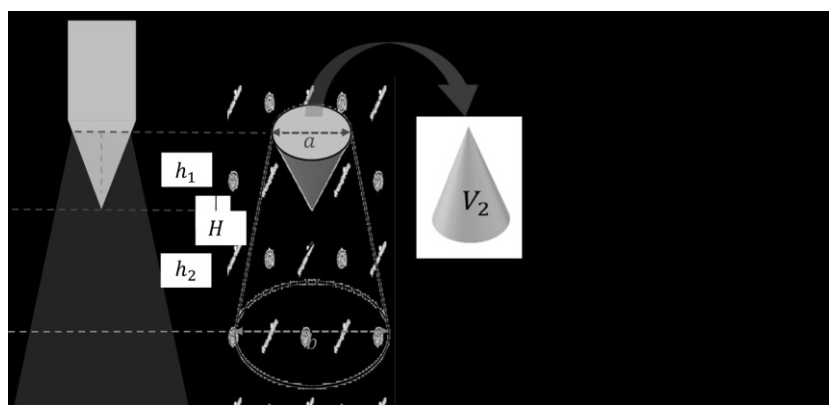


**Figure 3.16:** Schematic illustration of the procedure for calculation of illumination volume up to certain distance from fiber tip.

Previously observed focusing feature, located approximately  $170\ \mu\text{m}$  from tip end, in case of beam emitted in Rhodamine 6G water solution from optical fiber with cone tip of  $90^\circ$  can be

better understood from analysis of beam profiles. Since beam profiles are recorded in air, position of focal point is expected to be located closer to tip end compared to that on emission profile in Rhodamine 6G water solution. Beam profiles recorded in air starting from the tip end up to distance of 200  $\mu\text{m}$  confirm the existence of focal point with maximum intensity located at approximately 100  $\mu\text{m}$  from tip end (Figure 3.17). The diameter of focal point is estimated to be around 33  $\mu\text{m}$ .

This observation suggests that optical fiber with  $90^\circ$  cone angle, formed by mechanical grinding, provides the possibility to precisely focus light to defined location in brain tissue. Similar effect could be achieved using optical fiber with lensed tip. However fiber with lensed tip has a smooth curved tip surface which doesn't allow tissue penetration with minimal damage. Having a conic fiber tip with  $90^\circ$  cone angle makes it possible to minimize invasiveness caused by penetration while delivering focused light.

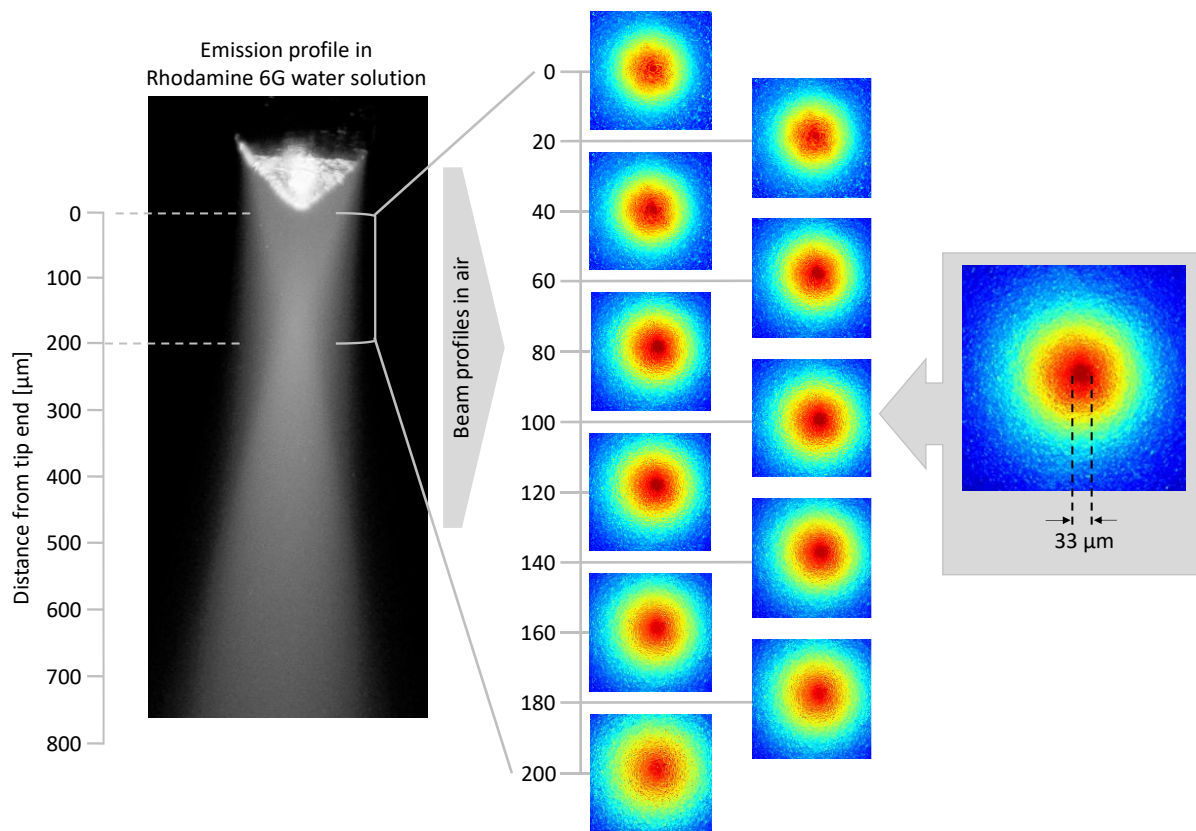


**Figure 3.17:** (left) Emission profile of tapered fiber with  $90^\circ$  cone angle, recorded as induced fluorescence in Rhodamine 6G water solution. Focal point is located approximately 180  $\mu\text{m}$  from tip end. (right) Beam profiles (recorded in air with microscope camera and analyzed using MATLAB beam profiler) of light emitted from tapered optical fiber with  $90^\circ$  cone angle starting from tip end, up to distance of 200  $\mu\text{m}$  from tip end.

## 4 ELECTRICAL CHARACTERIZATION

Although microelectrodes for recording neural activity have been used for decades, engineers are still trying to find a compromise between electrode size and recording capability. When designing and fabricating an optrode, microelectrodes have to be assembled such to enable recording of electrical signals that represent neural response to optical stimulation. Numerous solutions of optrode assemblies have been presented in Chapter 1.2.2. Fiber-based optrodes usually incorporate one or multiple microelectrodes simply glued to one or multiple optical fibers. As already mentioned, this approach leads to multi-tip optrode which may induce certain tissue damage during implantation. Optrode, fabricated in this research, incorporates two, approximately 600 nm thick and 60  $\mu\text{m}$  wide microelectrodes in form of thin gold coatings deposited on surface of optical fiber along the fiber length. Details of sputtering deposition process of such electrodes are presented in Chapter 2.2.2. However, only a small portion of such electrodes is exposed and can be used for electrical recording. Application of heat shrink tube, or epoxy coating enables controlled exposure of desired electrode portion (Figure 2.24).

Reducing the size of implanted microelectrodes also reduces the tissue damage, but increases total electrode impedance at the interface between electrode and brain [17]. Electrode-brain interface is also known as the electrode-electrolyte interface, because a double layer of polarized ions separates the electrode surface from the brain, resulting in a capacitive interface [153]. This interface is often modelled as Randles cell, with parallel connection of capacitor and resistor representing the double layer capacitance and faradaic resistance of the interface, respectively [17, 153, 154]. As the surface of electrode area decreases, capacitance also decreases leading to increase in impedance. Increased impedance is correlated with an increase of Johnson-Nyquist noise (thermal noise) [154, 155] and greater voltage division of the recorded signal [154], and thus is undesirable in case of microelectrodes for neural stimulation or recording. Effect of electrode size on impedance magnitude is discussed in detail in this chapter.

In this chapter, measurements of electrical resistance, as well as information concerning electrical impedance of deposited electrodes are presented. Results presented in this chapter may help when deciding on potential application of optrode fabricated in this research.

### 4.1 Electrical resistance

Electrical properties of deposited electrodes determine their usability in electrophysiological recording. Comparison of measurements of electrical resistance between deposited gold microelectrode and calculated values for gold microelectrodes of same geometry is a good indicator of electrode quality. Electrochemical impedance is a standard procedure for determination of electrodes recording capability in optogenetics. Depending on impedance value at 1 kHz, and a nature of its decrease with increase of frequency, recording electrodes are classified in two categories: electrodes that can record extracellular action potential (EAP) and electrodes suitable only for recording of local field potential (LFP). Measurements of electrical resistance of deposited electrodes, as well as the results of electrochemical impedance spectroscopy will be presented in this chapter. The effect of exposed electrode area on its recording performance will be discussed in detail.



### 4.1.1 Measurement procedure

To verify the quality of previously described electrode fabrication procedure, measurements of electrical resistance of deposited microelectrodes are performed using custom assembled setup (Figure 4.1). Measurements are performed on electrode deposited on flat glass surface using the same shadow mask and sputtering parameters as in case of electrode deposition on glass surface of optical fiber. Glass sheet with deposited electrode is mounted on micromanipulator. Electrical contacts are established using two probe needles with tip radius of 1  $\mu\text{m}$ . Digital microscope camera is used to ensure electrical contact between needle tip and deposited electrode. One probe needle remains fixed during the measurement, while another is mounted on a micromanipulator fixed on linear stage. Precise controlled movement of linear stage allows to perform resistance measurement along deposited electrode with step of 10 mm. Measurement procedure is repeated in case of 3 different electrodes deposited using same parameters.



**Figure 4.1:** Custom assembled setup for measurement of electrical resistance of approximately 60  $\mu\text{m}$  wide and 600 nm thick gold microelectrode using probe needles.

### 4.1.2 Results and discussion

Measured electrical resistance values along electrode length (with step of 10 mm) for three microelectrodes deposited with same parameters, as well as the average values are presented on Figure 4.2. Contact resistance of approximately 8.5  $\Omega$  is subtracted from measured values before calculation of average value and before plotting of the results. Calculated values of electrical resistance ( $R$ ) are also presented on the same graph. These values were calculated for different electrode lengths ( $l$ , from 10 to 60 mm) assuming measured electrode cross section area ( $A_{el}$ ), and well known value of bulk-gold electrical resistivity ( $\rho_{gold} = 2.44 \cdot 10^{-8} \Omega\text{m}$ ) at room temperature:

$$R = \rho_{gold} \frac{l}{A_{el}} \quad (4.1)$$

The area of electrode cross section is determined based on profilometry measurements (Figure 2.22) as the average area along 60 mm long electrode. Decrease of electrical resistance with reduction of electrode length can be approximated linearly. Difference between calculated and average measured electrical resistance increases as electrode length increases. Structure and morphology of gold thin films differs from that of bulk gold. As electrode length increases, effect of such morphological differences increases, leading to larger difference between measured and calculated resistance values. Another factor that may contribute to difference between measured and calculated resistance values is the approximation of electrode thickness and width. As it can be noticed from Figure 2.22, there are small variations of electrode width along electrode length. Furthermore, electrode thickness is not constant, and according to profilometry measurements, it varies in a range of 150 nm at the top of the electrode.

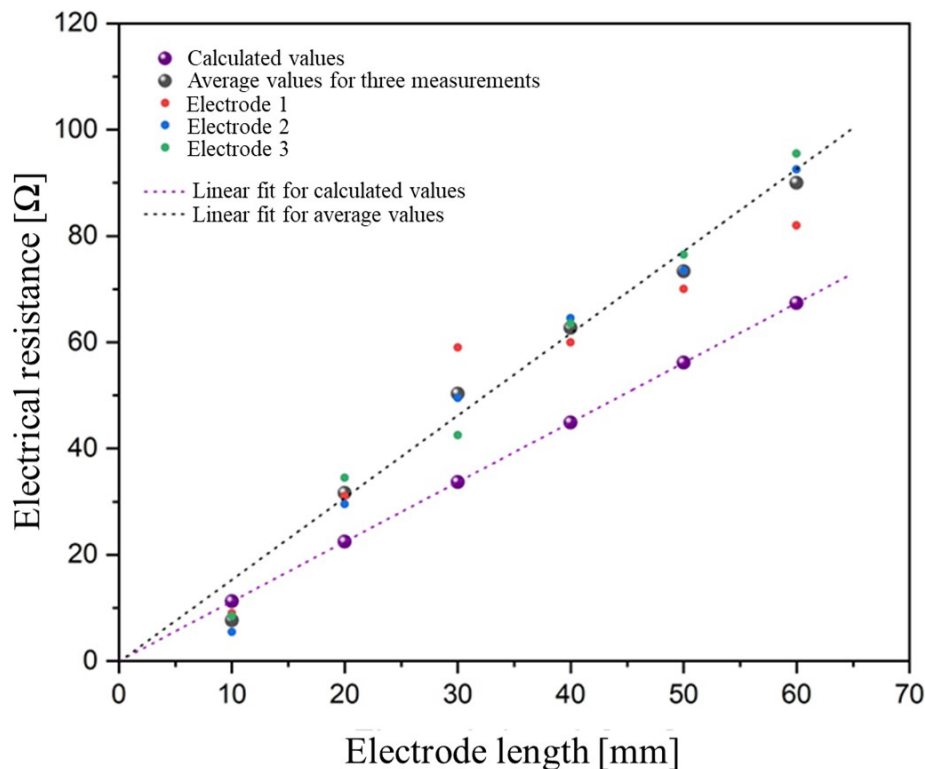


**Figure 4.2:** Measured and calculated electrical resistance of 60 mm long gold microelectrode (approximately 60  $\mu\text{m}$  wide and 600 nm thick). Resistance measurements are performed at each 10 mm of electrode length. Electrical resistance at each 10 mm is measured in case of three microelectrodes, deposited with identical parameters (Electrode 1, Electrode 2, and Electrode 3). Results are fitted based on average values calculated from measured values at each 10 mm of electrode length. Fit for calculated electrical resistance values is based on bulk-gold value of electrical resistance.

## 4.2 Electrochemical impedance spectroscopy

In addition to its application as a tool for investigation of electrochemical reaction mechanism and measurements of dielectric and transport properties of materials, electrochemical impedance spectroscopy (EIS) is widely used for electrical characterization of electrodes and metal coatings [156, 157]. The concept of electrical impedance is considered as one of the most important physical characteristics concerning resistance that the medium opposes to transport

of electrical current. It is usually defined as a measure of the ability of circuit to resist the flow of electrical current [158]. In a typical EIS, an alternating current (AC) signal is applied to tested electrode as driving force. As a result, characteristic response from the system interface is obtained. The system behaviour is usually simulated by means of an idealized circuit model that represents certain arrangement of passive electrical components (i.e. resistor, capacitor, inductances). These electrical components represent electrochemical process taking place at the system interface under study. High measurement sensitivity, resulting from the possibility to perform measurements applying very small amplitude signal at variable frequencies, makes EIS even more attractive when obtaining detailed information of the system (i.e. investigating oxide films formed on metals, monitoring degradation of polymer layers and paint coatings, corrosion).

When performing EIS to obtain detailed information about electrode characteristics in electrolyte environment, it is important to understand the nature of electrode-electrolyte interface. Solid-solution interface, called electrical double layer, forms at the interface between a conductive electrode and surrounding liquid electrolyte. This double layer is composed of two charged layers with opposing polarity. One layer consists of electrons on the electrode surface, while another layer represents ions in the electrolyte. These two layers are typically separated by a single layer of solvent molecules, adhered to the electrode surface, acting as dielectric in conventional capacitor. This kind of ion arrangement at the interface between electrode surface and liquid electrolyte is known as double layer capacitance (DLC) [159] (Figure 4.3). Dielectric polarization of electrolyte, charge separation by ion displacement, and adsorption of ions and molecules on electrode surface contribute to capacitance of double layer and are typically probed with EIS [159, 160]. To characterize electrical properties of double layer, equivalent circuit that considers double layer behaviour as pure capacitor and assumes that ion flow through metal surface (electrode) can be described by Ohm's law is assigned based on outcome data of EIS. This allows separating contribution response of different components in terms of double layer capacitance, solution resistance, resistance of electron charge transfer, and other parameters [158].

Measurement approach is typically either galvanostatic (application of sinusoidal current) or potentiostatic (application of sinusoidal voltage) mode. When sinusoidal current or voltage of a certain amplitude and frequency is applied, data obtained by EIS represent measured amplitude and phase shift of the output voltage or current, respectively [161, 162]. Above mentioned procedure is repeated over frequency range (typically in the kHz to Hz range) thereby generating a characteristic impedance spectrum.

Electrical resistance ( $R$ ), defined the ability of circuit element to resist the flow of electrical current, is described by Ohm's law in terms of ratio between voltage ( $U$ ) and current ( $I$ ):

$$R = \frac{U}{I} \quad (4.2)$$

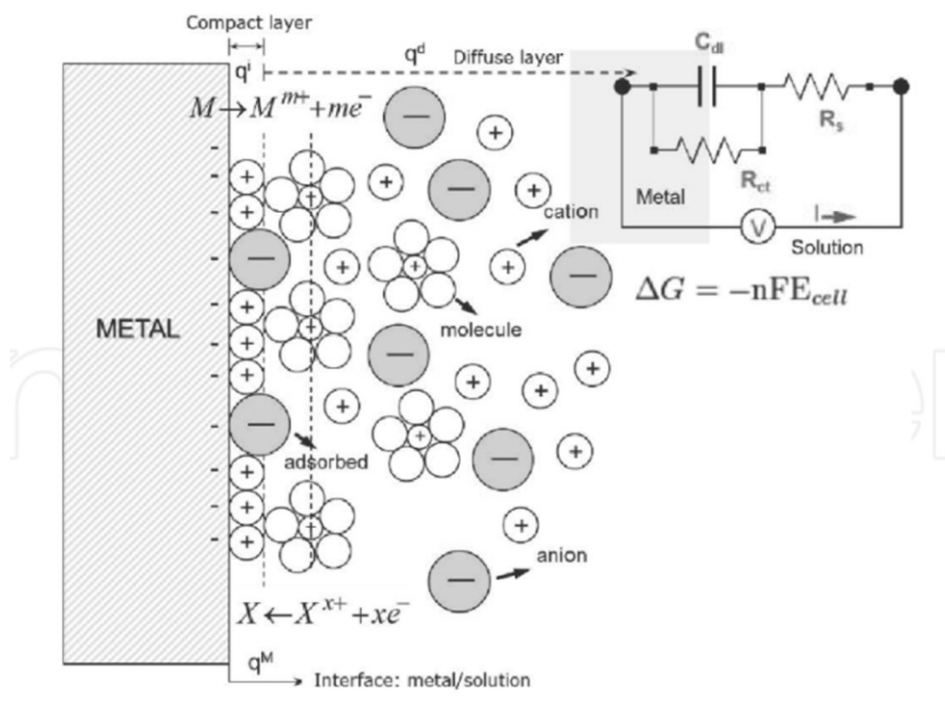


**Figure 4.3:** Illustration of electrochemical interface between metal electrode and electrolyte solution (electrical double layer) and its representative equivalent electrical circuit model with following components:  $R_s$ - resistance of the electrolyte solution,  $R_{ct}$ - charge transfer resistance, and  $C_{dl}$ - capacity of double layer. Image adapted from [158].

However application of (4.2) is limited to ideal resistor whose resistance value is independent on frequency. Furthermore AC current and voltage signals through such resistor are assumed to be in phase with each other. However, real resistors exhibit much more complex behavior, which leads to replacing of the simple resistance concept with more general circuit parameter – impedance ( $Z$ ).

Similar to resistance, impedance represents measure of the circuit ability to resist electrical current flow, but unlike resistance it is not limited to conditions valid for Ohm's law. As already mentioned, in potentiostatic mode sinusoidal voltage ( $V = V(t)$ ) is applied resulting in measurement of sinusoidal current response ( $I = I(t)$ ) over a defined frequency domain. Both sinusoidal signals are presented on Figure 4.4. Both, applied voltage, and resulting current, oscillate at the same frequency and intensity, but with constant time shift at certain angle known as phase shift angle ( $\phi$ ) which can vary from 0 to 90°.

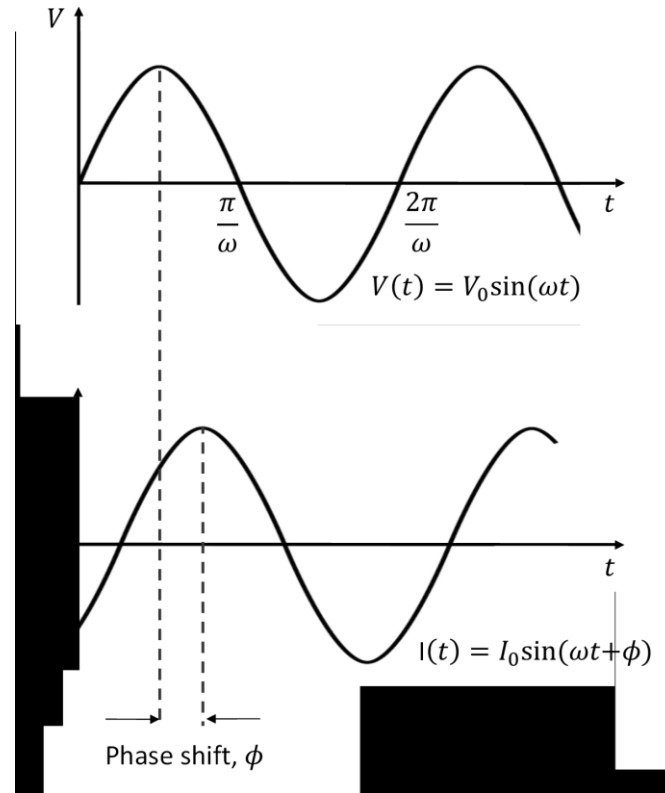


**Figure 4.4:** Sinusoidal current response to sinusoidal applied voltage in linear system

The excitation voltage signal, expressed as a function of time, has the form:

$$V(t) = V_0 \sin(\omega t) \quad (4.3)$$

where  $V(t)$  represents voltage at time  $t$ ,  $V_0$  and  $\omega$  represent amplitude of the signal and angular frequency, respectively. The relationship between angular frequency ( $\omega$ ) expressed in rad/s and a frequency  $f$  expressed in Hz is:

$$\omega = 2\pi f \quad (4.4)$$

To allow pseudo-linear system response, a small amplitude of AC voltage (5 – 10 mV) is usually applied. As a response to sinusoidal voltage signal, in linear (or pseudo-linear) system, sinusoidal current signal is characterized with the same frequency, but shifted in phase (figure), and can be expressed as:

$$I(t) = I_0 \sin(\omega t + \phi) \quad (4.5)$$

An expression for system impedance with magnitude  $Z_0$  and phase  $\phi$ , analogous to Ohm's Law, can be written as [158]:

$$Z = \frac{V(t)}{I(t)} = \frac{V_0 \sin(\omega t)}{I_0 \sin(\omega t + \phi)} = Z_0 \frac{\sin(\omega t)}{\sin(\omega t + \phi)} \quad (4.6)$$

Passive electrical components of the equivalent circuit assigned to the particular system mostly include resistors and capacitors which contribute to the total impedance value. Their contribution to total impedance value can be expressed in form of real ( $Z_{re}$ ) and imaginary

( $Z_{im}$ ) components, and thus impedance ( $Z$ ) can be expressed in complex form by incorporating the complex number ( $i = \sqrt{-1}$ ) [158]:

$$\mathbf{Z}(\omega) = \mathbf{Z}_{re} + i\mathbf{Z}_{im} \quad (4.7)$$

Phase angle can be expressed as:

$$\tan(\phi) = \frac{Z_{im}}{Z_{re}} \quad (4.8)$$

According to Euler's relationship:

$$e^{i\phi} = \cos\phi + i\sin\phi \quad (4.9)$$

Voltage and current signals can be described as:

$$\mathbf{V}(t) = \mathbf{V}_0 e^{i\omega t} \quad (4.10)$$

$$\mathbf{I}(t) = \mathbf{I}_0 e^{(i\omega t - \phi)} \quad (4.11)$$

Impedance is then presented as complex number:

$$\mathbf{Z}(\omega) = \frac{\mathbf{V}(t)}{\mathbf{I}(t)} = \mathbf{Z}_0 e^{i\phi} = \mathbf{Z}_0 (\cos\phi + i\sin\phi) \quad (4.12)$$

Typical measurement setup consists of working electrode (WE), which represents electrode under investigation, immersed in electrolyte solution together with counter electrode (CE) and reference electrode (RE). Reference electrode is used to determine the potential across electrochemical interface accurately. Since absolute potential of a single electrode cannot be measured, all potential measurements, in electrochemical systems are performed with respect to a reference electrode. Once experimental data are collected, they are usually analysed in form of Nyquist plots ( $-Z_{im}$  vs.  $Z_{re}$ ) presenting real impedance plotted against its imaginary part, and Bode plots ( $\log|Z|$  vs.  $\log|f|$ ,  $\phi$  vs.  $\log|f|$ ) presenting impedance modulus and its phase angle as a function of frequency.

#### 4.2.1 Electrode interface in brain and impedance of recording electrodes

As mentioned earlier, in case of either electrical stimulation or recording, microelectrode is always one in a pair. Beside recording/stimulating electrode, there is a second ground electrode representing potential/current sink. When implanted in brain, microelectrode is not in a direct contact with tissue. It actually forms a physical interface with extracellular fluid (electrolyte) present in brain. For the purpose of electrode characterization, this situation is usually compared to electrode immersed in a beaker with a salt solution [163]. The whole system is then considered as electrochemical cell where the microelectrode represents the working electrode (WE) of that cell, while ground electrode has a role of counter electrode (CE). However, the real scenario is much different, due to effect of tissue anisotropy on conductivity [164]. When characterizing electrode performance, immediate liquid environment surrounding the electrode surface matters the most. This liquid environment in brain has many similarities with simple phosphate buffered saline (PBS), which is often used for short-term electrode characterization in vitro. Using previously described setup for in vitro characterization allows addition of

reference electrode (RE) that measures electrical potential of the beaker with respect to WE and CE [163] (Figure 4.5), and thus enables detailed characterization of recording/stimulating microelectrodes.

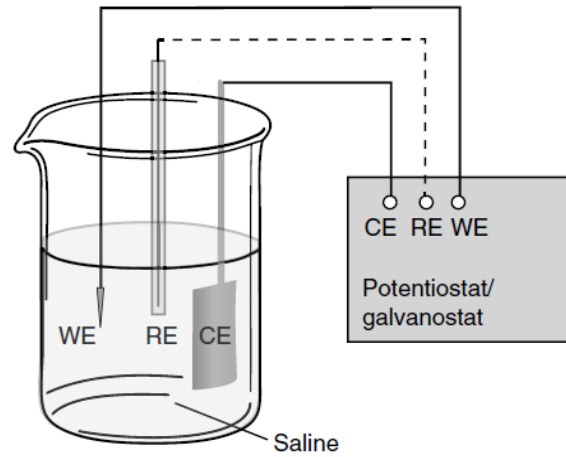


**Figure 4.5:** Representation of electrochemical cell for EIS measurements. Microelectrode represents the working electrode (WE) of that cell, while ground electrode has a role of counter electrode (CE). Reference electrode (RE) that measures electrical potential of the beaker with respect to WE and CE. Image adapted from [163].

To obtain electrochemical impedance of electrode-electrolyte system, similar to that in brain environment, microelectrode to be characterized (WE), CE and RE are immersed in PBS solution which mimics the liquid surrounding of implanted microelectrode and closes the electrical circuit. This setup actually represents a typical electrochemical cell for EIS measurements. Comparison between amplitude and phase of applied input signal with that of recorded output signal enables estimation of electrochemical impedance ( $Z$ ) of the system. As already explained, repeating measurement procedure over a certain frequency range results in a spectrum of impedances. Data is usually graphically presented as impedance magnitude ( $|Z|$ ) in logarithmic scale at each tested frequency. Knowing real ( $Z_{re}$ ) and imaginary ( $Z_{im}$ ) parts of impedance, impedance magnitude can be calculated as:

$$|Z| = \sqrt{|Z_{re}|^2 + |Z_{im}|^2} \quad (4.13)$$

Another common way of representing data obtained by EIS is plotting the impedance phase shift ( $\phi$ ) in linear scale over tested frequency range. According to (equation), impedance phase shift can be determined as:

$$\phi = \arctan\left(\frac{Z_{im}}{Z_{re}}\right) \quad (4.14)$$

Both ways of data presentation represent Bode plot which describes how well various frequency contents of an input signal are transferred over a solid-liquid boundary [163].

Electrochemical impedance spectroscopy is broadly used as a method for determining the quality of recording electrodes. Due to practical reasons, many researchers perform impedance characterization of microelectrodes only at 1 kHz [17, 94, 123, 165], claiming that the main information content in an action potential resides around this frequency. Even though this

statement is true, it should be noted that biological signals cover a much broader frequency range, and that an action potential has also higher frequency components in the depolarization and repolarization phases [163]. Furthermore, microelectrodes recording action potentials are also in parallel used for recording of local field potential with a broader frequency range. Since the difference in impedance magnitude between high and low frequencies is often several orders of magnitude, impedance value at 1 kHz ( $Z_{1\text{kHz}} = |Z_{1\text{kHz}}|$ ) shouldn't be used as a comparative measure of overall electrode recording capability.

Commenting on cut-off frequency of the electrode ( $f_{\text{cut-off}}$ ) is more relevant than just mentioning impedance magnitude at 1 kHz [163]. Following the phase angle from higher to lower frequencies leads to determination of cut-off frequency of an electrode. Cut-off frequency of an electrode can be determined from Bode plot as the frequency corresponding to phase angle of  $-45^\circ$  (Figure 4.6). Electrode transitioning from predominantly resistive to capacitive behavior, estimated from magnitude of impedance, can also be used to determine  $f_{\text{cut-off}}$  [163]. Signals above cut-off frequency can be reliably recorded by microelectrode, while signals recorded below  $f_{\text{cut-off}}$  are substantially phase shifted experiencing nonlinear distortion.

Even though based on numerous experiments and calculations, it has been confirmed that low impedance electrodes enable recording at high sound to noise ratio (SNR) [166, 167], some studies show that impedance makes little difference in practice. Furthermore, recent study [168] showed that two groups of microelectrodes with a difference in  $Z_{1\text{kHz}}$  of several orders of magnitude did not show difference in SNR of recorded signals. Possible explanation of such results is that neural interface represents a complex multi-component system, and that the electrode is just one component in recording chain where overall performance depends on system configuration.

Impedance is usually reduced either by making larger electrodes or by addition of more efficient electrode materials. Lower impedance is associated with larger electrode area, where recorded signal represent averaged signals from more cells. As the electrode area increases, number of cells contributing to the recording signal also increases. To enable more localized recording with smaller electrode area, impedance is lowered by addition of another material, resulting in larger electrochemical surface area and higher SNR [163].

The size of electrode-electrolyte interface area directly determines the impedance at 1 kHz, as well as cut-off frequency. In case of uncoated electrodes, and electrodes without additional surface modification, larger electrode area is associated with lower  $f_{\text{cut-off}}$ , and also lower impedance at 1 kHz [32, 163, 169, 170].



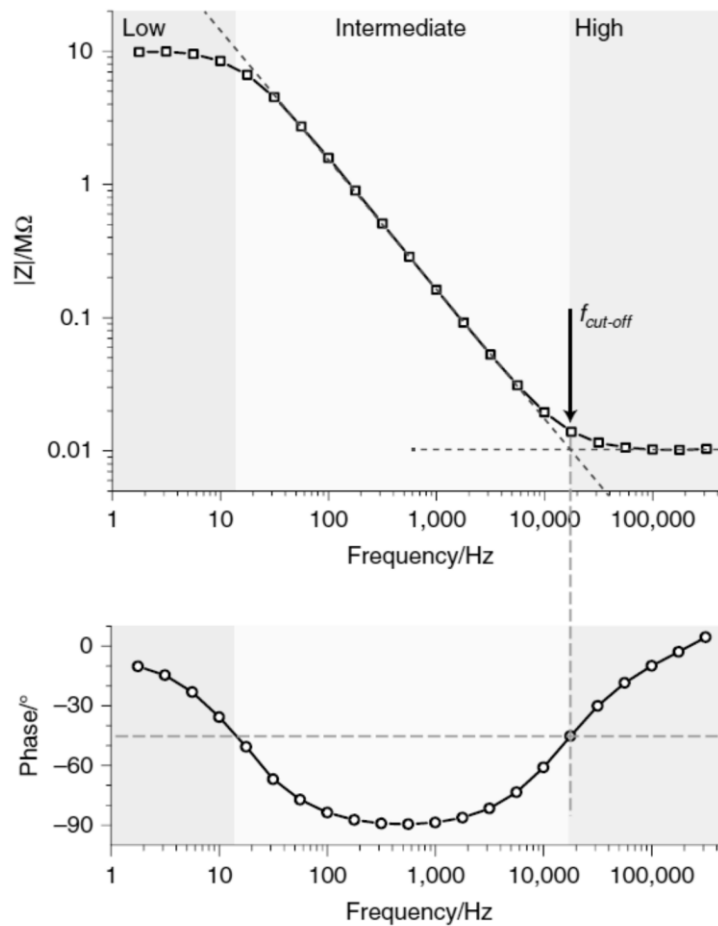


**Figure 4.6:** Determination of cut-off frequency ( $f_{cut-off}$ ) from Bode-plot as the frequency corresponding to phase angle of  $-45^\circ$ . Image adapted from [163].

#### 4.2.2 Measurement procedure

Electrochemical impedance spectroscopy (EIS) is performed using Gamry Potentiostat (the Reference 600). To avoid any artifacts due to impedance of counter electrode, 3-electrode setup is used (Figure 4.7). Working electrode and working sensing leads are both connected to tested electrode (WE). Counter electrode is connected to 99.99% platinum electrode, while reference electrode and reference sensing are both connected to an encapsulated Ag/AgCl wire (Gamry Instruments). Measurements are performed in frequency range from 100 kHz to 10 Hz, with 10 points per decade at a voltage of 10 mV against the reference electrode.

To obtain results close to those expected in brain environment, EIS measurements are performed in PBS. Optical fiber with deposited electrode is fixed to copper-covered FR4 substrate with one component silver conductive epoxy. Application of this epoxy helped fixing optical fiber to a holder and at the same time led to establishment of electrical connection between electrode deposited on optical fiber surface and copper layer on FR4 substrate. Adhesive copper tape is attached to copper layer on FR4 substrate for connection of working electrode and working sense leads of EIS equipment. Part of copper-covered FR4 substrate that doesn't contain fixed electrode is electrically insulated and fixed on micromanipulator. Side view of optical fiber with deposited electrode is observed with digital microscope camera.

Measurements are performed on optrodes containing heat shrink tube, so that only a small controlled portion of electrode area in fiber tip region is exposed. Same measurement procedure is repeated in case of three different electrode areas ( $60\mu\text{m} \times 50\mu\text{m}$ ,  $60\mu\text{m} \times 500\mu\text{m}$ , and  $100\mu\text{m} \times 500\mu\text{m}$ ). For each electrode, EIS is repeated several times until reproducible curve appeared. This procedure represents an important step before application of deposited microelectrodes for recording purpose, and helps to determine electrode area that should be exposed to obtain the most satisfying results.



**Figure 4.7:** Measurement setup (3-electrode setup) for electrochemical impedance of recording electrode fabricated in this work. Working electrode and working sensing leads are both connected to tested electrode (WE). Counter electrode is connected to 99.99% platinum electrode, while reference electrode and reference sensing are both connected to an encapsulated Ag/AgCl wire.

### 4.2.3 Results and discussion

Bode plot containing information about impedance magnitude (logarithmic) against frequency (logarithmic) for 600 nm thick gold microelectrodes of different sizes is presented on Figure 4.8. As expected, impedance magnitude at 1 kHz, and cut-off frequency both decrease with increase of electrode area. Smallest tested,  $60\mu\text{m}$  wide and  $50\mu\text{m}$  long, electrode has a very high impedance magnitude ( $455\text{ k}\Omega$ ) at 1 kHz. According to previous research [125], gold electrodes coated on optical fiber with such impedance value are considered to be applicable for electrophysiological recording in optogenetic experiments. However,  $f_{\text{cut-off}}$  of such small electrode is located outside measurement frequency range (10 Hz-100 kHz).

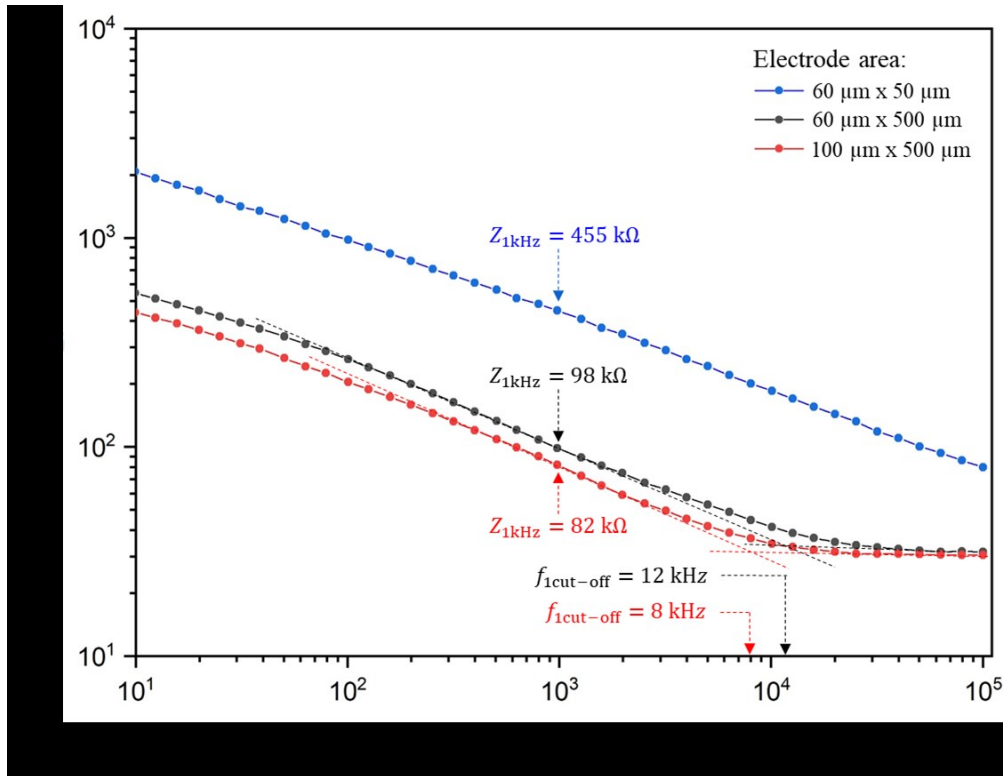


**Figure 4.8:** Bode plot of impedance magnitude (logarithmic) against frequency (logarithmic) for 600 nm thick gold microelectrodes of different sizes. Impedance magnitude at 1 kHz, as well as position of cut-off frequency are presented for each electrode

Some studies showed that signals above cut-off frequency can be reliably recorded by microelectrode, while signals recorded below  $f_{\text{cut-off}}$  are expected to be phase shifted experiencing nonlinear distortion. In this particular case, it means that a gold microelectrode with cut-off frequency higher than 100 kHz would not be suitable for reliable recordings (due to high SNR) at frequency of 1 kHz, where main information content in an action potential resides. One way to address this issue is the use of rough electrode materials or various roughening methods providing a large electrochemically active surface area on minimal geometrical dimensions [17, 171, 172]. Even though these methods enable to maintain small electrode size while achieving electrochemical properties of large electrodes, most roughening methods require rather complex processes which usually result in limited mechanical stability [173] or delamination [174]. Comparably easier method to achieve rough electrode surface is electrolyte-based electrochemically deposition of platinum coating [174, 175], which leads to 28 times lower average impedance compared to non-coated platinum electrodes [174]. Another approach consists of application of nanostructured 3,4-ethylene dioxythiophene/polystyrene sulfonate (PEDOT/PSS) coating which enables 10 times reduction of the impedance magnitude at 1 kHz, compared to uncoated gold electrodes [170].

Increasing of the electrode area, by increasing exposed electrode length from 50  $\mu\text{m}$  to 500  $\mu\text{m}$ , resulted in decrease of  $Z_{1\text{kHz}}$  to 98 k $\Omega$  followed by shifting of  $f_{\text{cut-off}}$  to 12 kHz. Further enlargement of 500  $\mu\text{m}$  long electrode area, by increasing electrode width from 60  $\mu\text{m}$  to 100  $\mu\text{m}$ , have led to further reduction of  $Z_{1\text{kHz}}$  to 82 k $\Omega$  and  $f_{\text{cut-off}}$  to 8 kHz. These values agree well with previously published EIS data for gold electrodes [170], and prove already established method of decreasing  $Z_{1\text{kHz}}$  and  $f_{\text{cut-off}}$  by increasing geometrical electrode area. However, application of large electrodes is limited to recording of LFPs due to spatial averaging of

recorded signals. Since there is no significant difference in signal amplitudes detected by differently sized electrodes far from the peak signal [32], these electrodes ( $60\mu\text{m} \times 500\mu\text{m}$  and  $100\mu\text{m} \times 500\mu\text{m}$ ) are expected to be suitable for extracellular distant recording of LFPs.

Even though large electrodes are considered to be not suitable for standard recordings at 1 kHz, they can be used for low frequency recordings. Disorders such as schizophrenia and epilepsy are associated with low frequency neuronal oscillations, which are filtered out by using standard MEAs [176]. Extremely large electrode areas (compared to standard MEAs) of few  $\text{mm}^2$  with very low impedance are successfully used to record these low frequency neuronal signals [176].

# 5 CONCLUSIONS AND OUTLOOK

Primary goals of this thesis include establishment of fabrication process, for fiber-based optrode with tapered fiber tip and two deposited metal electrodes on fiber surface, as well as optical and electrical characterization of optrode performance. Realization of these goals required arranging for necessary laboratory equipment, extensive experimental work, and application of multiple measurement techniques. Furthermore, a characterization environment for fabricated optrode was designed and assembled. Work conducted during this thesis represents a solid technological basis for further fabrication and characterization of fiber-based optrodes at the institute of Electronic Appliances and Circuits (IGS), University of Rostock.

This research advanced current fiber-based optrode designs, and introduced an approach for custom light delivery with reduced invasiveness based on fabrication of cone fiber tips with various angles. In addition, metal coatings as electrodes enable fabrication of one-tip fiber-based optrode which enables simultaneous light delivery and electrophysiological recording with minimal tissue damage. All results concerning optrode fabrication and its optical and electrical characterization are made easily accessible and well-structured in this thesis. In this chapter, milestones of this research are summarized and discussed. In addition, an outlook on advisable future work is described.

## 5.1 Conclusions

### 5.1.1 Fabrication

Optical fiber used for optrode fabrication was chosen such to satisfy requirements in terms of size (core diameter), numerical aperture, and biocompatibility. Fabrication process of fiber-based optrode was conducted in four steps:

1. Formation of conical fiber tip by mechanical grinding
2. Deposition of metal electrodes on fiber surface
3. Application of heat shrink tube / epoxy coating
4. Optrode assembly (establishment of electrical contacts and coupling to a light source)

Formation of conical fiber tip was achieved with custom made grinding setup described in chapter. The complete setup was built in-house as a part of this thesis. Main advantage of this setup is the possibility to fabricate tapered fiber tips with various cone angles. To achieve symmetric conical tips of good optical quality, an effect of various process parameters had to be taken into consideration. Determination of mutual rotation speed between optical fiber and grinding disc, as well as decision on processing time were the most important steps in whole process. Alignment of the optical fiber in fiber rotator represented another time consuming step that had to be successfully accomplished. As a result of numerous trials, process parameters were established such to enable fabrication of very smooth symmetric tapered tip with desired cone angle.

Although deposition of metal electrodes on curved fiber surface was achieved using sputtering equipment present in-house, custom fiber holder with shadow mask had to be

designed and fabricated such that deposited electrodes meet certain requirements in terms of position and size. Furthermore, substrate holder that would accept custom fiber holder, and fit in the transport arm of sputtering equipment was also designed and fabricated. Fiber holder and shadow mask, designed as part of this thesis, were assembled such to allow fiber rotation between sputtering steps without taking it out of holder with aligned shadow mask, and thus enable multiple electrode deposition on curved fiber surface. Mask alignment represented the most challenging task in this fabrication step, especially when sputtering electrode on surface of tapered tip region.

To enable multiple electrode deposition on surface of the same optical fiber, custom rotation and alignment setup was required. Setup was built using two microblocks and fiber rotator (ThorLabs) and included digital microscope camera for constant observation. This setup allowed angular control of electrode deposition, and thus enabled achieving two separate opposite microelectrodes on the surface of optical fiber.

To meet requirements in terms of biocompatibility, gold was chosen as electrode material. Initially, this fabrication step was hindered by poor adhesion between electrode and fiber glass surface. Although a thin titanium layer was deposited prior to gold sputtering, adhesion could be only improved by surface plasma treatment prior to sputtering.

Optical fiber, used for optrode fabrication in this thesis, was originally coated with polyimide layer which improved its mechanical stability. Fiber tips were formed with this polyimide layer still being coated on fiber. However, to reduce fiber diameter, this coating had to be removed prior to electrode deposition. First attempt to remove polyimide coating with open flame resulted in curved optical fiber due to exposure to heat. Another procedure of polyimide removal had to be conducted. Removing polyimide coating from optical fiber was done with hot sulfuric acid, which required chemical lab environment.

Since the fiber was brittle after removal of polyimide coating, an additional coating (much thinner than previous polyimide coating) was required. First solution was to coat optical fiber with biocompatible UV curable epoxy. This procedure required establishment of process chain that would be conducted in clean room atmosphere. Process chain contained four steps: dip coating, baking, development, and UV exposure (described in chapter). Process parameters of dip coating procedure (pulling speed, number of dipping cycles) were established based on numerous trials. Although this epoxy coating improved mechanical stability of the optical fiber, there was a need for achieving better optrode performance in terms of elasticity and bending capabilities. Another approach consisted of application of heat shrink tube and led to better results in terms of mechanical stability. It was difficult to find such heat shrink tube with very thin walls that would meet biocompatible requirements and improve optrode's mechanical stability. Contact with *Zeus Industrial Products* resulted in obtaining PTFE heat shrink tube (PTFE Sub-Lite Wall<sup>®</sup>) which fulfilled all of above mentioned requirements.

To turn optrode into functional device, establishment of electrical contacts between deposited electrodes on fiber surface and PCB, as well as coupling to a light source was required. Solution for establishment of electrical contacts was presented in a form of small (1 x 1 cm) FR4 substrate with copper layer on one side. Micromachining was applied to drill a centered hole on FR4 substrate that corresponds to diameter of optical fiber, and also to mechanically divide copper layer into two separate areas. Custom setup was designed and assembled for alignment and fixture of the optrode. Due to low thickness of deposited electrodes (approximately 600 nm) soldering was not an option. Another way to establish electrical contacts between electrodes deposited on fiber surface and corresponding copper areas on FR4 substrate was application of

conductive epoxy. One part silver conductive epoxy was identified as very good solution. Coupling to light source was achieved in a way of butt coupling between flat cleaved fiber end of the optrode and patch fiber coupled to LED.

### 5.1.2 Optical and electrical characterization

Optical characterization of fabricated optrode led to a conclusion that cone angle of fiber tip affects output light in terms of beam shape and intensity distribution. Furthermore, a correlation between cone angle and total transmitted optical power was experimentally observed.

An integrating sphere was used to quantify total transmitted light power of optrodes with various fiber tips. Optical setup for such measurements was assembled as part of this thesis. Tapered end of optrode was positioned inside integrating sphere, while another end was butt coupled to patch fiber coupled to LED. Once set, intensity of light source was kept constant throughout measurement process. Results obtained from these measurements suggest that increase in cone angle is followed by exponential increase in total transmitted light power (figure). Obtained correlation can serve as a guide when deciding on cone angle based on transmission requirements of particular optogenetic experiment. Compared to flat cleaved optical fiber, fiber tip with  $90^\circ$  cone angle transmits 34% less optical power, and represents the most efficient tapered optrode (fabricated in this thesis) in terms of transmission efficacy. A 10% decrease in transmitted optical power, compared to fiber tip with  $90^\circ$  cone angle, is observed in case of optrode with  $60^\circ$  cone tip angle. Further decrease of cone angle to  $30^\circ$  and  $14^\circ$  is followed by minor decrease in transmitted light power compared to optrode with  $60^\circ$  cone tip angle, and is estimated to be  $8^\circ$  and  $12^\circ$  respectively. Optical losses leading to above mentioned decrease in transmitted optical power were discussed in terms of total internal reflection, back scattering, Fresnel reflection, and surface scattering.

Illumination profiles of flat cleaved optrode and four optrodes with different cone angles ( $14^\circ$ ,  $30^\circ$ ,  $60^\circ$ , and  $90^\circ$ ) were observed as induced fluorescence in Rhodamine 6G water solution. To obtain such illumination profiles, custom setup allowing precise position adjustments had to be assembled. Container for Rhodamine 6G water solution was design and fabricated such to accept 0.5 ml of the solution, while having micro hole drilled on a side allowing optrode to be inserted with tip totally immersed. When inserted through side hole, optrode was supposed to fit in the side hole not allowing Rhodamine solution to leak out. A very thin glass sheet was placed on the upper side of container which was observed with microscope camera. Another end of optrode was butt coupled to patch fiber coupled to LED. Precise butt coupling was allowed by adjustable movements of micromanipulators with three orthogonal linear translation degrees of freedom. Camera settings had to be adjusted such to avoid overexposure, and were kept constant throughout characterization process.

Comparison of illumination profiles, recorded as induced fluorescence in Rhodamine 6G water solution, from optrodes with various fiber tips suggested that cone angle affects not only output beam shape, but also intensity distribution along. Detailed analysis of side illumination from tapered region and determination of taper emitting length (defined as the extent of taper light emitting segment measured from the tip end at which fluorescence intensity decreases to half of its value at the tip end) provided information about spatial extent of illumination around optrode tip.

Analysis of illumination profile recorded from optrode with 90° cone angle led to observation of focusing feature characteristic to lensed fiber. This feature can be used if focused light delivery is required in particular optogenetic experiment. Using lensed fiber as light delivery tool in optrode would lead to problems during implantation, and thus having a tapered fiber with focusing feature can be a big advantage.

Electrical characterization of deposited electrodes is done using electrochemical impedance spectroscopy (EIS). This method provides enough information about electrode applicability for electrophysiological recording. Previously mentioned heat shrink tube and epoxy coating enable controlled exposure of electrode area in the tip region. Results obtained from EIS showed that larger electrode area is associated with lower impedance magnitude. Initially, heat shrink tube was positioned such that 50  $\mu\text{m}$  long area of 60  $\mu\text{m}$  wide deposited electrode was exposed. This resulted in very high impedance magnitude (455  $\text{k}\Omega$  at 1 kHz) followed by cut-off frequency located far above 100 kHz. Such electrode would not enable accurate electrophysiological recordings at frequencies characteristic for neural activity (around and above 1 kHz). Enlargement of electrode area was achieved by increasing exposed electrode length from 50  $\mu\text{m}$  to 500  $\mu\text{m}$ , which resulted in much lower impedance magnitude (98  $\text{k}\Omega$  at 1 kHz) and cut-off frequency of 12 kHz. Further reduction of impedance magnitude (to 82  $\text{k}\Omega$  at 1 kHz) and cut-off frequency (to 8 kHz) was achieved by increasing the width of 500  $\mu\text{m}$  long electrode from 60  $\mu\text{m}$  to 100  $\mu\text{m}$ .

Even though impedance and cut-off frequency were decreased, the application of such large electrode is limited to recording of LFPs rather than EAP. The possibility for improvement of electrode recording capability will be discussed in next chapter.

## 5.2 Recommendations and future work

In the following, possible directions for improvement of optical and electrical optrode performances are proposed. Furthermore, possibilities of design modification, leading towards various optrode assemblies are also discussed.

### 5.2.1 Improvement of fabrication process

Although optrode fabrication process, described in this thesis, led to development of functional device, there are certain aspects that need improvement. Grinding setup for fabrication of fiber tips with various cone angles should be improved by incorporating a single angular stage with a possibility of controlled incline and height adjustment. This would enable more accurate positioning of the optical fiber on grinding disc after its substitution, which should result in higher reproducibility. Furthermore, it would enable fabrication of bigger range of cone angles starting from very small to very large.

Electrode deposition process should be more investigated in terms of effect of sputtering parameters on film morphology. Atomic force microscopy (AFM) should be applied to investigate surface roughness and porosity, which would help to adjust parameters of the sputtering process. As already discussed, electrode roughness affects impedance magnitude at 1 kHz, as well as cut-off frequency. Increasing surface roughness would increase electrochemically active electrode area without increase of electrode geometrical size. This approach would enable fabrication of small microelectrodes with lower impedance magnitude,



and cut-off frequency close to 1 kHz, which would allow recordings of EAPs. Current electrode deposition process allows electrode deposition on one optrode at a time. Designing fiber holder that accepts multiple optical fibers and enables simultaneous sputtering on multiple fibers would reduce time required for optrode fabrication. Although rotation and alignment setup allow precise angular control of deposited electrodes even in tapered region, small variations in position of deposited electrodes on fiber surface and in tapered region are result of manual fiber rotation after deposition of first electrode. When deposition of only two electrodes is required, a different approach to fiber holder design should be implemented. Ideally a new approach to fiber holder design would require only one alignment of cone tip in respect to mask opening, which would result in two equally positioned microelectrodes (with angle of  $180^\circ$  between them) in tapered region, as well as along optical fiber on its surface. However, when three or more electrodes should be deposited on the fiber surface, current approach to fiber holder should be applied.

### 5.2.2 Improvement of characterization methods and optrode functionality

Without access to animals and mice's or rat's brain tissue slices, optrode characterization was limited. Optical characterization was performed in air and water environment. Emission profiles were obtained in Rhodamine 6G water solution, and only relative comparison between tapered tips with various cone angles was possible. Since emission profiles from flat cleaved and tapered fiber tips were all recorded in water environment, analysis of effect of cone angle on beam shape and intensity distribution should be only discussed in terms of relative comparison. Application of Kubelka-Munk based model led to calculation of probable emission profile in brain tissue. However these calculations were limited to flat cleaved optical fiber. Even though calculations couldn't be performed in case of tapered fibers, based on a difference observed when comparing calculation results to emission profile of flat cleaved fiber in water solution, change in emission profiles of tapered fibers in brain tissue could be predicted to some extent. Detailed optical characterization of tapered fibers with various cone tips should be performed in brain tissue. Each custom assembled setup in this work for optical characterization in water or air can be modified in case of characterization in brain tissue environment.

Although electrochemical impedance enable reliable characterization of quality of electrical recording in case of microelectrodes fabricated in this work, better understanding of electrode's recording capability is usually achieved by performing actual electrophysiological recording in brain tissue.

Results presented in Chapter 4.2.3 in Chapter 4.2.3 suggest that cut-off frequency of 1 kHz could only be reached by increasing electrode area. This approach would limit the application of these electrodes to recording LFPs averaged from multiple neurons. On the other side, reduction of electrode area, leads to very high impedance magnitude at 1 kHz, and cut-off frequency located outside measured frequency interval (10 Hz – 100 kHz), not allowing to apply these electrodes in case of EAP detection. To address this issue, and to lower impedance magnitude at 1 kHz, as well as to reduce cut-off frequency to 1 kHz or lower, surface roughening techniques should be applied. Furthermore, PEDOT/PSS coating would, according to numerous studies, drastically reduce impedance magnitude at 1 kHz and significantly lower cut-off frequency. Establishment of PEDOT/PSS coating process, as well as investigation of its effect on impedance magnitude at 1 kHz and cut-off frequency represent the next step to improve recording capabilities of microelectrodes fabricated in this work.

## 6 BIBLIOGRAPHY

- [1] Fakhoury, M., Neural prostheses for restoring functions lost after spinal cord injury, *Neural regeneration research*, 10 (10) (2015), 1594–1595, doi:10.4103/1673-5374.165267.
- [2] Prakash, P., Srimathveeravalli, G., *Principles and Technologies for Electromagnetic Energy Based Therapies*, Academic Press, 2021.
- [3] Normann, R.A., Technology Insight: future neuroprosthetic therapies for disorders of the nervous system, *Nature Clinical Practice Neurology*, 3 (8) (2007), 444–452, doi:10.1038/ncpneuro0556.
- [4] Grill, W.M., Kirsch, R.F., Neuroprosthetic applications of electrical stimulation, *Assistive technology the official journal of RESNA*, 12 (1) (2000), 6–20, doi:10.1080/10400435.2000.10132006.
- [5] Min Zhao, Laura Chalmers, Lin Cao, Ana C. Vieira, Mark Mannis, Brian Reid, Electrical signaling in control of ocular cell behaviors, *Progress in Retinal and Eye Research*, 31 (1) (2012), 65–88, doi:10.1016/j.preteyeres.2011.10.001,
- [6] Sundelacruz, S., Levin, M., Kaplan, D.L., Role of Membrane Potential in the Regulation of Cell Proliferation and Differentiation, *Stem Cell Reviews and Reports*, 5 (3) (2009), 231–246, doi:10.1007/s12015-009-9080-2.
- [7] Tseng, A., Levin, M., Cracking the bioelectric code: Probing endogenous ionic controls of pattern formation, *Communicative & Integrative Biology*, 6 (1) (2013), e22595, doi:10.4161/cib.22595.
- [8] McCaig, C.D., Rajnicek, A.M., Song, B., Zhao, M., Controlling Cell Behavior Electrically: Current Views and Future Potential, *Physiological Reviews*, 85 (3) (2005), 943–978, doi:10.1152/physrev.00020.2004.
- [9] Min Zhao, Electrical fields in wound healing—An overriding signal that directs cell migration, *Seminars in Cell & Developmental Biology*, 20 (6) (2009), 674–682, doi:10.1016/j.semcdb.2008.12.009,
- [10] Matt Carter, Jennifer Shieh (eds.), *Guide to Research Techniques in Neuroscience (Second Edition)*, Academic Press, San Diego, 2015.
- [11] Jones, K.E., Campbell, P.K. & Normann, R.A. A glass/silicon composite intracortical electrode array. *Ann Biomed Eng* **20**, 423–437 (1992). <https://doi.org/10.1007/BF02368134>
- [12] Xie, X., Rieth, L., Negi, S., Bhandari, R., Caldwell, R., Sharma, R., Tathireddy, P., Solzbacher, F., Self aligned tip deinsulation of atomic layer Al<sub>2</sub>O<sub>3</sub> and parylene C coated Utah electrode array based neural interfaces, *Journal of micromechanics and microengineering structures, devices, and systems*, 24 (3) (2014), 35003, doi:10.1088/0960-1317/24/3/035003.
- [13] Boehler, C., Aqrawe, Z., Asplund, M., Applications of PEDOT in bioelectronic medicine, *Bioelectronics in Medicine*, 2 (2) (2019), 89–99, doi:10.2217/bem-2019-0014.
- [14] Cogan, S.F., Ehrlich, J., Plante, T.D., Smirnov, A., Shire, D.B., Gingerich, M., Rizzo, J.F., Sputtered iridium oxide films for neural stimulation electrodes, *Journal of biomedical materials research. Part B, Applied biomaterials*, 89 (2) (2009), 353–361, doi:10.1002/jbm.b.31223 .

- [15] Luo, X., Weaver, C.L., Zhou, D.D., Greenberg, R., Cui, X.T., Highly stable carbon nanotube doped poly(3,4-ethylenedioxythiophene) for chronic neural stimulation, *Biomaterials*, 32 (24) (2011), 5551–5557, doi:10.1016/j.biomaterials.2011.04.051.
- [16] C. Boehler, T. Stieglitz, M. Asplund, Nanostructured platinum grass enables superior impedance reduction for neural microelectrodes, *Biomaterials*, 67 (2015), 346–353, doi:10.1016/j.biomaterials.2015.07.036,
- [17] Bo Fan, Alexander V Rodriguez, Daniel G Vercosa, Caleb Kemere, Jacob T Robinson, Sputtered porous Pt for wafer-scale manufacture of low-impedance flexible microelectrodes, *J. Neural Eng.*, 17 (3) (2020), 36029, doi:10.1088/1741-2552/ab965c.
- [18] Ronchi, S., Fiscella, M., Marchetti, C., Viswam, V., Müller, J., Frey, U., Hierlemann, A., Single-Cell Electrical Stimulation Using CMOS-Based High-Density Microelectrode Arrays, *Frontiers in neuroscience*, 13 (2019), 208, doi:10.3389/fnins.2019.00208.
- [19] Mandat, T.S., Hurwitz, T., Honey, C.R., Hypomania as an adverse effect of subthalamic nucleus stimulation: report of two cases, *Acta neurochirurgica*, 148 (8) (2006), 895-7; discussion 898, doi:10.1007/s00701-006-0795-4.
- [20] Aravanis, A.M., Wang, L.-P., Zhang, F., Meltzer, L.A., Mogri, M.Z., Schneider, M.B., Deisseroth, K., An optical neural interface: in vivo control of rodent motor cortex with integrated fiberoptic and optogenetic technology, *Journal of neural engineering*, 4 (3) (2007), S143-56, doi:10.1088/1741-2560/4/3/S02.
- [21] Hariz, M.I., Complications of deep brain stimulation surgery, *Movement disorders official journal of the Movement Disorder Society*, 17 Suppl 3 (2002), S162-6.
- [22] Alivisatos, A.P., Andrews, A.M., Boyden, E.S., Chun, M., Church, G.M., Deisseroth, K., Donoghue, J.P., Fraser, S.E., Lippincott-Schwartz, J., Looger, L.L., Masmanidis, S., McEuen, P.L., Nurmikko, A.V., Park, H., Peterka, D.S., Reid, C., Roukes, M.L., Scherer, A., Schnitzer, M., Sejnowski, T.J., Shepard, K.L., Tsao, D., Turrigiano, G., Weiss, P.S., Xu, C., Yuste, R., Zhuang, X., Nanotools for Neuroscience and Brain Activity Mapping, *ACS Nano*, 7 (3) (2013), 1850–1866, doi:10.1021/nn4012847.
- [23] Zeck, G., Jetter, F., Channappa, L., Bertotti, G., Thewes, R., Electrical Imaging: Investigating Cellular Function at High Resolution, *Advanced Biosystems*, 1 (11) (2017), 1700107, doi:10.1002/adbi.201700107.
- [24] Rossant, C., Kadir, S., Goodman, D.F.M., Schulman, J., Belluscio, M., Buzsaki, G., Harris, K.D., Spike sorting for large, dense electrode arrays, *bioRxiv* (2015), doi:10.1101/015198,
- [25] Obien, M.E.J., Deligkaris, K., Bullmann, T., Bakkum, D.J., Frey, U., Revealing neuronal function through microelectrode array recordings, *Frontiers in neuroscience*, 8 (2015), doi:10.3389/fnins.2014.00423, <https://www.frontiersin.org/articles/10.3389/fnins.2014.00423>.
- [26] Bruce L. McNaughton, John O’Keefe, Carol A. Barnes, The stereotrode: A new technique for simultaneous isolation of several single units in the central nervous system from multiple unit records, *Journal of neuroscience methods*, 8 (4) (1983), 391–397, doi:10.1016/0165-0270(83)90097-3, <https://www.sciencedirect.com/science/article/pii/0165027083900973>.
- [27] Campbell, P.K., Jones, K.E., Huber, R.J., Horch, K.W., Normann, R.A., A silicon-based, three-dimensional neural interface: manufacturing processes for an intracortical electrode array, *IEEE Transactions on Biomedical Engineering*, 38 (8) (1991), 758–768, doi:10.1109/10.83588.

- [28] Blanche, T.J., Spacek, M.A., Hetke, J.F., Swindale, N.V., Polytrodes: High-Density Silicon Electrode Arrays for Large-Scale Multiunit Recording, *Journal of neurophysiology*, 93 (5) (2005), 2987–3000, doi:10.1152/jn.01023.2004.
- [29] Mora Lopez, C., Putzeys, J., Raducanu, B.C., Ballini, M., Wang, S., Andrei, A., Rochus, V., Vandebriel, R., Severi, S., van Hoof, C., Musa, S., van Helleputte, N., Yazicioglu, R.F., Mitra, S., A Neural Probe With Up to 966 Electrodes and Up to 384 Configurable Channels in 0.13  $\mu\text{m}$  SOI CMOS, *IEEE Transactions on Biomedical Circuits and Systems*, 11 (3) (2017), 510–522, doi:10.1109/TBCAS.2016.2646901.
- [30] Kim, R., Joo, S., Jung, H., Hong, N., Nam, Y., Recent trends in microelectrode array technology for in vitro neural interface platform, *Biomedical Engineering Letters*, 4 (2) (2014), 129–141, doi:10.1007/s13534-014-0130-6.
- [31] Rossant, C., Kadir, S., Goodman, D.F.M., Schulman, J., Belluscio, M., Buzsaki, G., Harris, K.D., Spike sorting for large, dense electrode arrays, *bioRxiv* (2015), doi:10.1101/015198,
- [32] Viswam, V., Obien, M.E.J., Franke, F., Frey, U., Hierlemann, A., Optimal Electrode Size for Multi-Scale Extracellular-Potential Recording From Neuronal Assemblies, *Frontiers in neuroscience*, 13 (2019), doi:10.3389/fnins.2019.00385,
- [33] Hughes, M.P., Bustamante, K., Banks, D.J., Ewins, D.J., Effects of electrode size on the performance of neural recording microelectrodes, in: 1st Annual International IEEE-EMBS Special Topic Conference on Microtechnologies in Medicine and Biology. Proceedings (Cat. No.00EX451), pp. 220–223, 2000.
- [34] Ahuja, A.K., Behrend, M.R., Whalen, J.J., Humayun, M.S., Weiland, J.D., The Dependence of Spectral Impedance on Disc Microelectrode Radius, *IEEE Transactions on Biomedical Engineering*, 55 (4) (2008), 1457–1460, doi:10.1109/TBME.2007.912430.
- [35] Buzsáki, G., Anastassiou, C.A., Koch, C., The origin of extracellular fields and currents — EEG, ECoG, LFP and spikes, *Nature Reviews Neuroscience*, 13 (6) (2012), 407–420, doi:10.1038/nrn3241.
- [36] Supratim Ray, Challenges in the quantification and interpretation of spike-LFP relationships, *Current opinion in neurobiology*, 31 (2015), 111–118, doi:10.1016/j.conb.2014.09.004,
- [37] Alt, M.T., Fiedler, E., Rudmann, L., Ordonez, J.S., Ruther, P., Stieglitz, T., Let There Be Light—Optoprobes for Neural Implants, *Proc. IEEE*, 105 (1) (2017), 101–138, doi:10.1109/JPROC.2016.2577518.
- [38] Yawo, H., Kandori, H., Koizumi, A. (eds.), *Optogenetics: Light-Sensing Proteins and Their Applications*, Springer, Tokyo, 2015.
- [39] Fork, R.L., Laser Stimulation of Nerve Cells in *Aplysia*, *Science*, 171 (3974) (1971), 907–908, doi:10.1126/science.171.3974.907.
- [40] Nagel, G., Szellas, T., Huhn, W., Kateriya, S., Adeishvili, N., Berthold, P., Ollig, D., Hegemann, P., Bamberg, E., Channelrhodopsin-2, a directly light-gated cation-selective membrane channel, *Proceedings of the National Academy of Sciences of the United States of America*, 100 (24) (2003), 13940–13945, doi:10.1073/pnas.1936192100.
- [41] Chow, B.Y., Han, X., Dobry, A.S., Qian, X., Chuong, A.S., Li, M., Henninger, M.A., Belfort, G.M., Lin, Y., Monahan, P.E., Boyden, E.S., High-performance genetically targetable optical neural silencing by light-driven proton pumps, *Nature*, 463 (7277) (2010), 98–102, doi:10.1038/nature08652.

- [42] Spudich, J.L., Yang, C.S., Jung, K.H., Spudich, E.N., Retinylidene proteins: structures and functions from archaea to humans, *Annual review of cell and developmental biology*, 16 (2000), 365–392, doi:10.1146/annurev.cellbio.16.1.365.
- [43] Yizhar, O., Fenno, L.E., Davidson, T.J., Mogri, M., Deisseroth, K., Optogenetics in neural systems, *Neuron*, 71 (1) (2011), 9–34, doi:10.1016/j.neuron.2011.06.004.
- [44] Boyden, E.S., Zhang, F., Bamberg, E., Nagel, G., Deisseroth, K., Millisecond-timescale, genetically targeted optical control of neural activity, *Nature neuroscience*, 8 (9) (2005), 1263–1268, doi:10.1038/nn1525.
- [45] Fan, B., Li, W., Miniaturized optogenetic neural implants: a review, *Lab on a chip*, 15 (19) (2015), 3838–3855, doi:10.1039/c5lc00588d.
- [46] Zhang, F., Wang, L.-P., Brauner, M., Liewald, J.F., Kay, K., Watzke, N., Wood, P.G., Bamberg, E., Nagel, G., Gottschalk, A., Deisseroth, K., Multimodal fast optical interrogation of neural circuitry, *Nature*, 446 (7136) (2007), 633–639, doi:10.1038/nature05744.
- [47] Gradinaru, V., Zhang, F., Ramakrishnan, C., Mattis, J., Prakash, R., Diester, I., Goshen, I., Thompson, K.R., Deisseroth, K., Molecular and cellular approaches for diversifying and extending optogenetics, *Cell*, 141 (1) (2010), 154–165, doi:10.1016/j.cell.2010.02.037.
- [48] Zhao, H., Recent Progress of Development of Optogenetic Implantable Neural Probes, *International journal of molecular sciences*, 18 (8) (2017), doi:10.3390/ijms18081751.
- [49] Zhang, F., Gradinaru, V., Adamantidis, A.R., Durand, R., Airan, R.D., Lecea, L. de, Deisseroth, K., Optogenetic interrogation of neural circuits: technology for probing mammalian brain structures, *Nature protocols*, 5 (3) (2010), 439–456, doi:10.1038/nprot.2009.226.
- [50] Dawydow, A., Gueta, R., Ljaschenko, D., Ullrich, S., Hermann, M., Ehmann, N., Gao, S., Fiala, A., Langenhan, T., Nagel, G., Kittel, R.J., Channelrhodopsin-2-XXL, a powerful optogenetic tool for low-light applications, *Proceedings of the National Academy of Sciences of the United States of America*, 111 (38) (2014), 13972–13977, doi:10.1073/pnas.1408269111.
- [51] Mohanty, S.K., Lakshminarayanan, V., Optical Techniques in Optogenetics, *Journal of Modern Optics*, 62 (12) (2015), 949–970, doi:10.1080/09500340.2015.1010620.
- [52] Gradinaru, V., Mogri, M., Thompson, K.R., Henderson, J.M., Deisseroth, K., Optical deconstruction of parkinsonian neural circuitry, *Science (New York, N.Y.)*, 324 (5925) (2009), 354–359, doi:10.1126/science.1167093.
- [53] Krook-Magnuson, E., Armstrong, C., Oijala, M., Soltesz, I., On-demand optogenetic control of spontaneous seizures in temporal lobe epilepsy, *Nature communications*, 4 (2013), 1376 EP -, doi:10.1038/ncomms2376, <https://doi.org/10.1038/ncomms2376>.
- [54] Fenno, L., Yizhar, O., Deisseroth, K., The development and application of optogenetics, *Annual review of neuroscience*, 34 (2011), 389–412, doi:10.1146/annurev-neuro-061010-113817.
- [55] Barrett, J.M., Berlinguer-Palmini, R., Degenaar, P., Optogenetic approaches to retinal prosthesis, *Visual neuroscience*, 31 (4-5) (2014), 345–354, doi:10.1017/S0952523814000212.
- [56] Albert, P.R., Light up your life: optogenetics for depression? *Journal of psychiatry & neuroscience JPN*, 39 (1) (2014), 3–5, doi:10.1503/jpn.130267.
- [57] Stujenske, J.M., Spellman, T., Gordon, J.A., Modeling the Spatiotemporal Dynamics of Light and Heat Propagation for In Vivo Optogenetics, *Cell reports*, 12 (3) (2015), 525–534, doi:10.1016/j.celrep.2015.06.036.

- [58] Rungta, R.L., Osmanski, B.-F., Boido, D., Tanter, M., Charpak, S., Light controls cerebral blood flow in naive animals, *Nature communications*, 8 (2017), 14191, doi:10.1038/ncomms14191.
- [59] Yizhar, O., Fenno, L.E., Davidson, T.J., Mogri, M., Deisseroth, K., Optogenetics in neural systems, *Neuron*, 71 (1) (2011), 9–34, doi:10.1016/j.neuron.2011.06.004.
- [60] Pavone, F.S., Shoham, S. (eds.), *Handbook of neurophotonics*, CRC Press Taylor & Francis Group, Boca Raton, 2020.
- [61] Thompson, S.M., Masukawa, L.M., Prince, D.A., Temperature dependence of intrinsic membrane properties and synaptic potentials in hippocampal CA1 neurons in vitro, *Journal of Neuroscience*, 5 (3) (1985), 817–824, doi:10.1523/JNEUROSCI.05-03-00817.1985,
- [62] Moser, E., Mathiesen, I., Andersen, P., Association between brain temperature and dentate field potentials in exploring and swimming rats, *Science*, 259 (5099) (1993), 1324–1326, doi:10.1126/science.8446900.
- [63] Adamantidis, A.R., Zhang, F., Aravanis, A.M., Deisseroth, K., Lecea, L. de, Neural substrates of awakening probed with optogenetic control of hypocretin neurons, *Nature*, 450 (7168) (2007), 420–424, doi:10.1038/nature06310.
- [64] Caggiano, V., Cheung, V.C.K., Bizzi, E., An Optogenetic Demonstration of Motor Modularity in the Mammalian Spinal Cord, *Scientific reports*, 6 (1) (2016), 35185, doi:10.1038/srep35185.
- [65] Cardin, J.A., Carlén, M., Meletis, K., Knoblich, U., Zhang, F., Deisseroth, K., Tsai, L.-H., Moore, C.I., Targeted optogenetic stimulation and recording of neurons in vivo using cell-type-specific expression of Channelrhodopsin-2, *Nature protocols*, 5 (2) (2010), 247–254, doi:10.1038/nprot.2009.228.
- [66] Bernstein, J.G., Boyden, E.S., Optogenetic tools for analyzing the neural circuits of behavior, *Trends in cognitive sciences*, 15 (12) (2011), 592–600, doi:10.1016/j.tics.2011.10.003.
- [67] Falkner, A.L., Lin, D., Recent advances in understanding the role of the hypothalamic circuit during aggression, *Frontiers in systems neuroscience*, 8 (2014), 168, doi:10.3389/fnsys.2014.00168.
- [68] Pienaar, I.S., Gartside, S.E., Sharma, P., Paola, V. de, Gretenkord, S., Withers, D., Elson, J.L., Dexter, D.T., Pharmacogenetic stimulation of cholinergic pedunculopontine neurons reverses motor deficits in a rat model of Parkinson’s disease, *Molecular Neurodegeneration*, 10 (1) (2015), 47, doi:10.1186/s13024-015-0044-5.
- [69] Jiang, J., Cui, H., Rahmouni, K., Optogenetics and pharmacogenetics: principles and applications, *American journal of physiology. Regulatory, integrative and comparative physiology*, 313 (6) (2017), R633-R645, doi:10.1152/ajpregu.00091.2017.
- [70] Steinberg, E.E., Christoffel, D.J., Deisseroth, K., Malenka, R.C., Illuminating circuitry relevant to psychiatric disorders with optogenetics, *Current opinion in neurobiology*, 30 (2015), 9–16,
- [71] Chiang, C.-C., Ladas, T.P., Gonzalez-Reyes, L.E., Durand, D.M., Seizure suppression by high frequency optogenetic stimulation using in vitro and in vivo animal models of epilepsy, *Brain stimulation*, 7 (6) (2014), 890–899, doi:10.1016/j.brs.2014.07.034.
- [72] Paz, J.T., Huguenard, J.R., Optogenetics and epilepsy: past, present and future, *Epilepsy currents*, 15 (1) (2015), 34–38, doi:10.5698/1535-7597-15.1.34.
- [73] Tania Zaglia, Nicola Pianca, Giulia Borile, Francesca Da Broi, Claudia Richter, Marina Campione, Stephan E. Lehnart, Stefan Luther, Domenico Corrado, Lucile Miquerol, Marco Mongillo, Optogenetic determination of the myocardial requirements for extrasystoles by cell

- type-specific targeting of ChannelRhodopsin-2, *Proceedings of the National Academy of Sciences*, 112 (32) (2015), E4495-E4504, doi:10.1073/pnas.1509380112.
- [74] Lu, C., Frierip, U.P., Koppes, R.A., Canales, A., Caggiano, V., Selvidge, J., Bizzi, E., Anikeeva, P., Polymer Fiber Probes Enable Optical Control of Spinal Cord and Muscle Function In Vivo, *Adv. Funct. Mater.*, 24 (42) (2014), 6594–6600, doi:10.1002/adfm.201401266.
- [75] Moser, T., Optogenetic stimulation of the auditory pathway for research and future prosthetics, *Current opinion in neurobiology*, 34 (2015), 29–36, doi:10.1016/j.conb.2015.01.004.
- [76] Hernandez, V.H., Gehrt, A., Jing, Z., Hoch, G., Jeschke, M., Strenzke, N., Moser, T., Optogenetic Stimulation of the Auditory Nerve, *JoVE* (92) (2014), e52069, doi:10.3791/52069,
- [77] Cheng, M.Y., Wang, E.H., Steinberg, G.K., Optogenetic Approaches to Study Stroke Recovery, *ACS chemical neuroscience*, 5 (12) (2014), 1144–1145, doi:10.1021/cn500216f.
- [78] Huber, D., Petreanu, L., Ghitani, N., Ranade, S., Hromádka, T., Mainen, Z., Svoboda, K., Sparse optical microstimulation in barrel cortex drives learned behaviour in freely moving mice, *Nature*, 451 (7174) (2008), 61–64, doi:10.1038/nature06445,
- [79] Iwai, Y., Honda, S., Ozeki, H., Hashimoto, M., Hirase, H., A simple head-mountable LED device for chronic stimulation of optogenetic molecules in freely moving mice, *Neuroscience research*, 70 (1) (2011), 124–127, doi:10.1016/j.neures.2011.01.007.
- [80] Ueda, O., Pearton, S.J., *Materials and Reliability Handbook for Semiconductor Optical and Electron Devices*, Springer New York, New York, NY, 2013.
- [81] Held, G., *Introduction to light emitting diode technology and applications*, CRC Press, Boca Raton, 2009.
- [82] Grossman, N., Poher, V., Grubb, M.S., Kennedy, G.T., Nikolic, K., McGovern, B., Berlinguer Palmi, R., Gong, Z., Drakakis, E.M., Neil, M.A.A., Dawson, M.D., Burrone, J., Degenaar, P., Multi-site optical excitation using ChR2 and micro-LED array, *Journal of neural engineering*, 7 (1) (2010), 16004, doi:10.1088/1741-2560/7/1/016004.
- [83] Tae-il Kim, Jordan G. McCall, Yei Hwan Jung, Xian Huang, Edward R. Siuda, Yuhang Li, Jizhou Song, Young Min Song, Hsuan An Pao, Rak-Hwan Kim, Chaofeng Lu, Sung Dan Lee, Il-Sun Song, GunChul Shin, Ream Al-Hasani, Stanley Kim, Meng Peun Tan, Yonggang Huang, Fiorenzo G. Omenetto, John A. Rogers, Michael R. Bruchas, *Injectable, Cellular-Scale Optoelectronics with Applications for Wireless Optogenetics*, *Science*, 340 (6129) (2013), 211–216, doi:10.1126/science.1232437.
- [84] Klein, E., Gossler, C., Paul, O., Ruther, P., High-Density  $\mu$ LED-Based Optical Cochlear Implant With Improved Thermomechanical Behavior, *Frontiers in neuroscience*, 12 (2018), 659, doi:10.3389/fnins.2018.00659.
- [85] Moser, E., Mathiesen, I., Andersen, P., Association between brain temperature and dentate field potentials in exploring and swimming rats, *Science*, 259 (5099) (1993), 1324–1326, doi:10.1126/science.8446900.
- [86] Zhang, J., Laiwalla, F., Kim, J.A., Urabe, H., van Wagenen, R., Song, Y.-K., Connors, B.W., Zhang, F., Deisseroth, K., Nurmikko, A.V., Integrated device for optical stimulation and spatiotemporal electrical recording of neural activity in light-sensitized brain tissue, *Journal of neural engineering*, 6 (5) (2009), 55007, doi:10.1088/1741-2560/6/5/055007.

- [87] Doronina-Amitonova, L.V., Fedotov, I.V., Ivashkina, O.I., Zots, M.A., Fedotov, A.B., Anokhin, K.V., Zheltikov, A.M., Implantable fiber-optic interface for parallel multisite long-term optical dynamic brain interrogation in freely moving mice, *Scientific reports*, 3 (1) (2013), 3265, doi:10.1038/srep03265.
- [88] Sileo, L., Bitzenhofer, S.H., Spagnolo, B., Pöpplau, J.A., Holzhammer, T., Pisanello, M., Pisano, F., Bellistri, E., Maglie, E., Vittorio, M. de, Ruther, P., Hanganu-Opatz, I.L., Pisanello, F., Tapered Fibers Combined With a Multi-Electrode Array for Optogenetics in Mouse Medial Prefrontal Cortex, *Frontiers in neuroscience*, 12 (2018), 771, doi:10.3389/fnins.2018.00771.
- [89] Cui, G., Jun, S.B., Jin, X., Pham, M.D., Vogel, S.S., Lovinger, D.M., Costa, R.M., Concurrent activation of striatal direct and indirect pathways during action initiation, *Nature*, 494 (7436) (2013), 238–242, doi:10.1038/nature11846.
- [90] Cui, G., Jun, S.B., Jin, X., Luo, G., Pham, M.D., Lovinger, D.M., Vogel, S.S., Costa, R.M., Deep brain optical measurements of cell type-specific neural activity in behaving mice, *Nature protocols*, 9 (6) (2014), 1213–1228, doi:10.1038/nprot.2014.080.
- [91] Guo, Q., Zhou, J., Feng, Q., Lin, R., Gong, H., Luo, Q., Zeng, S., Luo, M., Fu, L., Multi-channel fiber photometry for population neuronal activity recording, *Biomedical optics express*, 6 (10) (2015), 3919–3931, doi:10.1364/BOE.6.003919.
- [92] Lütcke, H., Murayama, M., Hahn, T., Margolis, D.J., Astori, S., zum Alten Borgloh, S.M., Göbel, W., Yang, Y., Tang, W., Kügler, S., Sprengel, R., Nagai, T., Miyawaki, A., Larkum, M.E., Helmchen, F., Hasan, M.T., Optical recording of neuronal activity with a genetically-encoded calcium indicator in anesthetized and freely moving mice, *Frontiers in neural circuits*, 4 (2010), 9, doi:10.3389/fncir.2010.00009.
- [93] Anikeeva P, Andalman AS, Witten I, Warden M, Goshen I, Grosenick L, Gunaydin LA, Frank LM, Deisseroth K. Optetrode: a multichannel readout for optogenetic control in freely moving mice. *Nat Neurosci*. 2011 Dec 4;15(1):163-70. doi: 10.1038/nn.2992.
- [94] Wang, L., Huang, K., Zhong, C., Wang, L., Lu, Y., Fabrication and modification of implantable optrode arrays for in vivo optogenetic applications, *Biophysics reports*, 4 (2) (2018), 82–93, doi:10.1007/s41048-018-0052-4.
- [95] Pisano, F., Pisanello, M., Lee, S.J., Lee, J., Maglie, E., Balena, A., Sileo, L., Spagnolo, B., Bianco, M., Hyun, M., Vittorio, M. de, Sabatini, B.L., Pisanello, F., Depth-resolved fiber photometry with a single tapered optical fiber implant, *Nature methods*, 16 (11) (2019), 1185–1192, doi:10.1038/s41592-019-0581-x.
- [96] Pisanello, F., Mandelbaum, G., Pisanello, M., Oldenburg, I.A., Sileo, L., Markowitz, J.E., Peterson, R.E., Della Patria, A., Haynes, T.M., Emara, M.S., Spagnolo, B., Datta, S.R., Vittorio, M. de, Sabatini, B.L., Dynamic illumination of spatially restricted or large brain volumes via a single tapered optical fiber, *Nature neuroscience*, 20 (8) (2017), 1180–1188, doi:10.1038/nn.4591.
- [97] Park, S., Guo, Y., Jia, X., Choe, H.K., Grena, B., Kang, J., Park, J., Lu, C., Canales, A., Chen, R., Yim, Y.S., Choi, G.B., Fink, Y., Anikeeva, P., One-step optogenetics with multifunctional flexible polymer fibers, *Nature neuroscience*, 20 (4) (2017), 612–619, doi:10.1038/nn.4510.
- [98] Acker, L., Pino, E.N., Boyden, E.S., Desimone, R., FEF inactivation with improved optogenetic methods, *Proceedings of the National Academy of Sciences of the United States of America*, 113 (46) (2016), E7297-E7306, doi:10.1073/pnas.1610784113.



- [99] Anthony N. Zorzos, Edward S. Boyden, Clifton G. Fonstad, Multiwaveguide implantable probe for light delivery to sets of distributed brain targets, *Opt. Lett.*, 35 (24) (2010), 4133–4135, doi:10.1364/OL.35.004133.
- [100] Kampasi, K., English, D.F., Seymour, J., Stark, E., McKenzie, S., Vöröslakos, M., Buzsáki, G., Wise, K.D., Yoon, E., Dual color optogenetic control of neural populations using low-noise, multishank optoelectrodes, *Microsystems & nanoengineering*, 4 (2018), doi:10.1038/s41378-018-0009-2.
- [101] Kanno, S., Lee, S., Harashima, T., Kuki, T., Kino, H., Mushiake, H., Yao, H., Tanaka, T., Multiple optical stimulation to neuron using Si opto-neural probe with multiple optical waveguides and metal-cover for optogenetics, in: 2013 35th Annual International Conference of the IEEE Engineering in Medicine and Biology Society (EMBC), pp. 253–256, 2013.
- [102] Hoffman, L., Welkenhuysen, M., Andrei, A., Musa, S., Luo, Z., Libbrecht, S., Severi, S., Soussan, P., Baekelandt, V., Haesler, S., Gielen, G., Puers, R., Braeken, D., High-density optrode-electrode neural probe using SixNy photonics for in vivo optogenetics, in: 2015 IEEE International Electron Devices Meeting (IEDM), 29.5.1-29.5.4, 2015.
- [103] Son, Y., Jenny Lee, H., Kim, J., Shin, H., Choi, N., Justin Lee, C., Yoon, E.-S., Yoon, E., Wise, K.D., Geun Kim, T., Cho, I.-J., In vivo optical modulation of neural signals using monolithically integrated two-dimensional neural probe arrays, *Scientific reports*, 5 (1) (2015), 15466, doi:10.1038/srep15466.
- [104] Kim, C., Jeong, J., Kim, S.J., Recent Progress on Non-Conventional Microfabricated Probes for the Chronic Recording of Cortical Neural Activity, *Sensors*, 19 (5) (2019), doi:10.3390/s19051069, <https://www.mdpi.com/1424-8220/19/5/1069>.
- [105] Cho, I.-J., Baac, H.W., Yoon, E., A 16-site neural probe integrated with a waveguide for optical stimulation, in: 2010 IEEE 23rd International Conference on Micro Electro Mechanical Systems (MEMS), pp. 995–998, 2010.
- [106] Rubehn, B., Wolff, S.B.E., Tovote, P., Lüthi, A., Stieglitz, T., A polymer-based neural microimplant for optogenetic applications: design and first in vivo study, *Lab on a chip*, 13 (4) (2013), 579–588, doi:10.1039/c2lc40874k.
- [107] Azimipour, M., Baumgartner, R., Liu, Y., Jacques, S.L., Eliceiri, K., Pashaie, R., Extraction of optical properties and prediction of light distribution in rat brain tissue, *Journal of biomedical optics*, 19 (7) (2014), 75001, doi:10.1117/1.JBO.19.7.075001.
- [108] Gysbrechts, B., Wang, L., Trong, N.N.D., Cabral, H., Navratilova, Z., Battaglia, F., Saeys, W., Bartic, C., Light distribution and thermal effects in the rat brain under optogenetic stimulation, *Journal of biophotonics*, 9 (6) (2016), 576–585, doi:10.1002/jbio.201500106.
- [109] Mehdi Azimipour, Farid Atry, Ramin Pashaie, Effect of blood vessels on light distribution in optogenetic stimulation of cortex, *Opt. Lett.*, 40 (10) (2015), 2173–2176, doi:10.1364/OL.40.002173.
- [110] B. Beauvoit, S.M. Evans, T.W. Jenkins, E.E. Miller, B. Chance, Correlation Between the Light Scattering and the Mitochondrial Content of Normal Tissues and Transplantable Rodent Tumors, *Analytical Biochemistry*, 226 (1) (1995), 167–174, doi:10.1006/abio.1995.1205,
- [111] Wu, F., Stark, E., Im, M., Cho, I.-J., Yoon, E.-S., Buzsáki, G., Wise, K.D., Yoon, E., An implantable neural probe with monolithically integrated dielectric waveguide and recording electrodes for optogenetics applications, *Journal of neural engineering*, 10 (5) (2013), 56012, doi:10.1088/1741-2560/10/5/056012.

- [112] Fan-Gang Zeng, Barbara Canlon, Recognizing the journey and celebrating the achievement of cochlear implants, *Hearing Research*, 322 (2015), 1–3, doi:10.1016/j.heares.2015.02.003,
- [113] Connor, C.M., Craig, H.K., Raudenbush, S.W., Heavner, K., Zwolan, T.A., The Age at Which Young Deaf Children Receive Cochlear Implants and Their Vocabulary and Speech-Production Growth: Is There an Added Value for Early Implantation? *Ear and Hearing*, 27 (6) (2006),
- [114] Andrej Kral, Rainer Hartmann, Dariusch Mortazavi, Rainer Klinke, Spatial resolution of cochlear implants: the electrical field and excitation of auditory afferents, *Hearing Research*, 121 (1) (1998), 11–28, doi:10.1016/S0378-5955(98)00061-6,
- [115] Marcus Jeschke, Tobias Moser, Considering optogenetic stimulation for cochlear implants, *Hearing Research*, 322 (2015), 224–234, doi:10.1016/j.heares.2015.01.005,
- [116] Goßler, C., Bierbrauer, C., Moser, R., Kunzer, M., Holc, K., Pletschen, W., Köhler, K., Wagner, J., Schwaerzle, M., Ruther, P., Paul, O., Neef, J., Keppeler, D., Hoch, G., Moser, T., Schwarz, U.T., GaN-based micro-LED arrays on flexible substrates for optical cochlear implants, *J. Phys. D: Appl. Phys.*, 47 (20) (2014), 205401, doi:10.1088/0022-3727/47/20/205401.
- [117] Kampasi, K., Stark, E., Seymour, J., Na, K., Winful, H.G., Buzsáki, G., Wise, K.D., Yoon, E., Fiberless multicolor neural optoelectrode for in vivo circuit analysis, *Scientific reports*, 6 (2016), 30961, doi:10.1038/srep30961.
- [118] Gradinaru, V., Thompson, K.R., Zhang, F., Mogri, M., Kay, K., Schneider, M.B., Deisseroth, K., Targeting and readout strategies for fast optical neural control in vitro and in vivo, *The Journal of neuroscience the official journal of the Society for Neuroscience*, 27 (52) (2007), 14231–14238, doi:10.1523/JNEUROSCI.3578-07.2007.
- [119] Diester, I., Kaufman, M.T., Mogri, M., Pashaie, R., Goo, W., Yizhar, O., Ramakrishnan, C., Deisseroth, K., Shenoy, K.V., An optogenetic toolbox designed for primates, *Nature neuroscience*, 14 (3) (2011), 387–397, doi:10.1038/nn.2749.
- [120] Liu, X., Ramirez, S., Pang, P.T., Puryear, C.B., Govindarajan, A., Deisseroth, K., Tonegawa, S., Optogenetic stimulation of a hippocampal engram activates fear memory recall, *Nature*, 484 (7394) (2012), 381–385, doi:10.1038/nature11028.
- [121] Kim, G.B., Cho, J.R., Shin, H.-S., Choi, J.H., Cortical mapping of the optically evoked responses in channelrhodopsin-2 mouse model, *Annual International Conference of the IEEE Engineering in Medicine and Biology Society. IEEE Engineering in Medicine and Biology Society. Annual International Conference, 2011* (2011), 6769–6772, doi:10.1109/IEMBS.2011.6091669.
- [122] Ji Dai, Ilker Ozden, Daniel I. Brooks, Fabien Wagner, Travis May, Naubahar S. Agha, Benjamin R. Brush, David Borton, Arto V. Nurmikko, David L. Sheinberg, Modified toolbox for optogenetics in the nonhuman primate, *Neurophotonics*, 2 (2015), 31202.
- [123] Stark, E., Koos, T., Buzsáki, G., Diode probes for spatiotemporal optical control of multiple neurons in freely moving animals, *Journal of neurophysiology*, 108 (1) (2012), 349–363, doi:10.1152/jn.00153.2012.
- [124] Royer, S., Zemelman, B.V., Barbic, M., Losonczy, A., Buzsáki, G., Magee, J.C., Multi-array silicon probes with integrated optical fibers: light-assisted perturbation and recording of local neural circuits in the behaving animal, *European Journal of Neuroscience*, 31 (12) (2010), 2279–2291, doi:10.1111/j.1460-9568.2010.07250.x.

- [125] Ozden, I., Wang, J., Lu, Y., May, T., Lee, J., Goo, W., O'Shea, D.J., Kalanithi, P., Diester, I., Diagne, M., Deisseroth, K., Shenoy, K.V., Nurmikko, A.V., A coaxial optrode as multifunction write-read probe for optogenetic studies in non-human primates, *Journal of neuroscience methods*, 219 (1) (2013), 142–154, doi:10.1016/j.jneumeth.2013.06.011.
- [126] John P. Seymour, Daryl R. Kipke, Neural probe design for reduced tissue encapsulation in CNS, *Biomaterials*, 28 (25) (2007), 3594–3607, doi:10.1016/j.biomaterials.2007.03.024,
- [127] Wang, J., Wagner, F., Borton, D.A., Zhang, J., Ozden, I., Burwell, R.D., Nurmikko, A.V., van Wagenen, R., Diester, I., Deisseroth, K., Integrated device for combined optical neuromodulation and electrical recording for chronic in vivo applications, *Journal of neural engineering*, 9 (1) (2012), 16001, doi:10.1088/1741-2560/9/1/016001.
- [128] Welkenhuysen, M., Hoffman, L., Luo, Z., Proft, A. de, van den Haute, C., Baekelandt, V., Debyser, Z., Gielen, G., Puers, R., Braeken, D., An integrated multi-electrode-optrode array for in vitro optogenetics, *Scientific reports*, 6 (2016), 20353, doi:10.1038/srep20353.
- [129] Abaya, T.V.F., Blair, S., Tathireddy, P., Rieth, L., Solzbacher, F., A 3D glass optrode array for optical neural stimulation, *Biomedical optics express*, 3 (12) (2012), 3087–3104, doi:10.1364/BOE.3.003087.
- [130] Kim, H., Brünner, H.S., Carlén, M., The DMCdrive: practical 3D-printable micro-drive system for reliable chronic multi-tetrode recording and optogenetic application in freely behaving rodents, *Scientific reports*, 10 (1) (2020), 11838, doi:10.1038/s41598-020-68783-9.
- [131] Sileo, L., Pisanello, M., Vittorio, M. de, Pisanello, F., Fabrication of multipoint light emitting optical fibers for optogenetics, in: *Optical Techniques in Neurosurgery, Neurophotonics, and Optogenetics II*, SPIE Proceedings, Eds. H. Hirschberg, S.J. Madsen, E.D. Jansen, Q. Luo, S.K. Mohanty, N.V. Thakor, 93052O, SPIE, 2015.
- [132] Stöckle, R., Fokas, C., Deckert, V., Zenobi, R., Sick, B., Hecht, B., Wild, U.P., High-quality near-field optical probes by tube etching, *Appl. Phys. Lett.*, 75 (2) (1999), 160–162, doi:10.1063/1.124305.
- [133] Wasa, K., Kanno, I., Kotera, H., *Handbook of sputter deposition technology: Fundamentals and applications for functional thin films, nanomaterials and MEMS*, 2nd edn., William Andrew, Waltham MA, 2012.
- [134] Okuyama, H., Iwata, N., Yamamoto, H., Position-selective growth of carbon nanotubes on Ni catalysts/Mo underlayers by thermal chemical vapor deposition, *J. Mater. Res.*, 21 (11) (2006), 2888–2893, doi:10.1557/jmr.2006.0351.
- [135] Sabu Thomas, Yves Grohens, Yasir Beeran Pottathara (eds.), *Industrial Applications of Nanomaterials*, Elsevier, 2019.
- [136] Addanki, S., Amiri, I.S., Yupapin, P., Review of optical fibers-introduction and applications in fiber lasers, *Results in Physics*, 10 (2018), 743–750, doi:10.1016/j.rinp.2018.07.028.
- [137] G. E. Town, J. T. Lizier, Tapered holey fibers for spot-size and numerical-aperture conversion, *Opt. Lett.*, 26 (14) (2001), 1042–1044, doi:10.1364/OL.26.001042.
- [138] Verdaasdonk, R.M., Borst, C., Ray tracing of optically modified fiber tips. 1: Spherical probes, *Appl Opt*, 30 (16) (1991), 2159–2171, doi:10.1364/AO.30.002159,
- [139] Patiño-Jurado, B., Botero-Cadavid, J.F., Garcia-Sucerquia, J., Analytical study of the numerical aperture of cone-shaped optical fibers: A tool for tailored designs, *Heliyon*, 5 (5) (2019), e01612, doi:10.1016/j.heliyon.2019.e01612.

- [140] Chuong, A.S., Miri, M.L., Busskamp, V., Matthews, G.A.C., Acker, L.C., Sørensen, A.T., Young, A., Klapoetke, N.C., Henninger, M.A., Kodandaramaiah, S.B., Ogawa, M., Ramanlal, S.B., Bandler, R.C., Allen, B.D., Forest, C.R., Chow, B.Y., Han, X., Lin, Y., Tye, K.M., Roska, B., Cardin, J.A., Boyden, E.S., Noninvasive optical inhibition with a red-shifted microbial rhodopsin, *Nature neuroscience*, 17 (8) (2014), 1123–1129, doi:10.1038/nn.3752.
- [141] Van Truong, G., Park, S., van Tran, N., Kang, H.W., Spatial effect of conical angle on optical-thermal distribution for circumferential photocoagulation, *Biomedical optics express*, 8 (12) (2017), 5663–5674, doi:10.1364/BOE.8.005663.
- [142] Vo-Dinh, T., *Biomedical photonics handbook*, CRC Press, Boca Raton, Fla, 2003.
- [143] Foutz, T.J., Arlow, R.L., McIntyre, C.C., Theoretical principles underlying optical stimulation of a channelrhodopsin-2 positive pyramidal neuron, *Journal of neurophysiology*, 107 (12) (2012), 3235–3245, doi:10.1152/jn.00501.2011.
- [144] Dufour, S., Koninck, Y. de, Optrodes for combined optogenetics and electrophysiology in live animals, *Neurophotonics*, 2 (3) (2015), 31205, doi:10.1117/1.NPh.2.3.031205.
- [145] Zhang, F., Wang, L.-P., Boyden, E.S., Deisseroth, K., Channelrhodopsin-2 and optical control of excitable cells, *Nature methods*, 3 (10) (2006), 785–792, doi:10.1038/nmeth936.
- [146] Han, X., In vivo application of optogenetics for neural circuit analysis, *ACS chemical neuroscience*, 3 (8) (2012), 577–584, doi:10.1021/cn300065j.
- [147] P. Kubelka, and F. Munk, Ein Beitrag Zur Optik Der Farbanstriche, *Z. Techn. Phys.*, 12 (1931), 593–601.
- [148] Weik M., *Fiber Optics Standard Dictionary*, Springer New York, New York, 1997.
- [149] Bevilacqua, F., Piguet, D., Marquet, P., Gross, J. d., Tromberg, B.J., Depeursinge, C., In vivo local determination of tissue optical properties: applications to human brain, *Appl Opt*, 38 (22) (1999), 4939, doi:10.1364/AO.38.004939.
- [150] Yaroslavsky, A.N, Schulze, P.C., Yaroslavsky, I.V., Schober, R., Ulrich, F. Schwarzmaier, H, Optical properties of selected native and coagulated human brain tissues in vitro in the visible and near infrared spectral range, *Physics in medicine and biology*, 47 (12) (2002), 2059–2073.
- [151] Abaya, T.V.F., Diwekar, M., Blair, S., Tathireddy, P., Rieth, L., Solzbacher, F., Deep-tissue light delivery via optrode arrays, *Journal of biomedical optics*, 19 (1) (2014), 15006, doi:10.1117/1.JBO.19.1.015006.
- [152] David Brinkmeier, ISO11146 Laser Beam Profiler (<https://github.com/david-brinkmeier/fokuspokus/releases/tag/v1.0>), Matlab, 2022.
- [153] Daniel R. Merrill, Marom Bikson, John G.R. Jefferys, Electrical stimulation of excitable tissue: design of efficacious and safe protocols, *Journal of neuroscience methods*, 141 (2) (2005), 171–198, doi:10.1016/j.jneumeth.2004.10.020.
- [154] Robinson, D.A., The electrical properties of metal microelectrodes, *Proc. IEEE*, 56 (6) (1968), 1065–1071, doi:10.1109/PROC.1968.6458.
- [155] Nyquist, H., Thermal Agitation of Electric Charge in Conductors, *Phys. Rev.*, 32 (1) (1928), 110–113, doi:10.1103/PhysRev.32.110,
- [156] Digby D. Macdonald, Reflections on the history of electrochemical impedance spectroscopy, *Electrochimica Acta*, 51 (8) (2006), 1376–1388, doi:10.1016/j.electacta.2005.02.107,

- [157] Srinivasan, R., Punathil Meethal, R., EIS Technique for Corrosion Study and Analysis, in: A Treatise on Corrosion Science, Engineering and Technology, Eds. U. Kamachi Mudali, T. Subba Rao, S. Ningshen, R. G. Pillai, R. P. George, T.M. Sridhar, pp. 3–20, Springer Nature Singapore, Singapore, 2022.
- [158] Ruiz, A., Hernández, H., Hernández, J., Orozco-Cruz, R., Ruiz Reynoso, A., González, C., Miranda-Hernández, J., Electrochemical Impedance Spectroscopy (EIS): A Review Study of Basic Aspects of the Corrosion Mechanism Applied to Steels, in: 2020.
- [159] Wolfgang Schmickler, Douglas Henderson, New models for the structure of the electrochemical interface, *Progress in Surface Science*, 22 (4) (1986), 323–419, doi:10.1016/0079-6816(86)90005-5,
- [160] Schalenbach, M., Durmus, Y.E., Tempel, H., Kungl, H., Eichel, R.-A., Double layer capacitances analysed with impedance spectroscopy and cyclic voltammetry: validity and limits of the constant phase element parameterization, *Phys. Chem. Chem. Phys.*, 23 (37) (2021), 21097–21105, doi:10.1039/D1CP03381F.
- [161] Jie Li, Catia Arbizzani, Signe Kjelstrup, Jie Xiao, Yong-yao Xia, Yan Yu, Yong Yang, Ilias Belharouak, Thomas Zawodzinski, Seung-Taek Myung, Rinaldo Raccichini, Stefano Passerini, Good practice guide for papers on batteries for the Journal of Power Sources, *Journal of Power Sources*, 452 (2020), 227824, doi:10.1016/j.jpowsour.2020.227824,
- [162] Nina Meddings, Marco Heinrich, Frédéric Overney, Jong-Sook Lee, Vanesa Ruiz, Emilio Napolitano, Steffen Seitz, Gareth Hinds, Rinaldo Raccichini, Miran Gaberšček, Juyeon Park, Application of electrochemical impedance spectroscopy to commercial Li-ion cells: A review, *Journal of Power Sources*, 480 (2020), 228742, doi:10.1016/j.jpowsour.2020.228742,
- [163] Boehler, C., Carli, S., Fadiga, L., Stieglitz, T., Asplund, M., Tutorial: guidelines for standardized performance tests for electrodes intended for neural interfaces and bioelectronics, *Nature protocols*, 15 (11) (2020), 3557–3578, doi:10.1038/s41596-020-0389-2.
- [164] McCann, H., Pisano, G., Beltrachini, L., Variation in Reported Human Head Tissue Electrical Conductivity Values, *Brain topography*, 32 (5) (2019), 825–858, doi:10.1007/s10548-019-00710-2.
- [165] Ozden, I., Wang, J., Lu, Y., May, T., Lee, J., Goo, W., O'Shea, D.J., Kalanithi, P., Diester, I., Diagne, M., Deisseroth, K., Shenoy, K.V., Nurmikko, A.V., A coaxial optrode as multifunction write-read probe for optogenetic studies in non-human primates, *Journal of neuroscience methods*, 219 (1) (2013), 142–154, doi:10.1016/j.jneumeth.2013.06.011.
- [166] Ludwig, K.A., Uram, J.D., Yang, J., Martin, D.C., Kipke, D.R., Chronic neural recordings using silicon microelectrode arrays electrochemically deposited with a poly(3,4-ethylenedioxythiophene) (PEDOT) film, *Journal of neural engineering*, 3 (1) (2006), 59–70, doi:10.1088/1741-2560/3/1/007.
- [167] Zhao, Z., Gong, R., Zheng, L., Wang, J., In Vivo Neural Recording and Electrochemical Performance of Microelectrode Arrays Modified by Rough-Surfaced AuPt Alloy Nanoparticles with Nanoporosity, *Sensors*, 16 (11) (2016), doi:10.3390/s16111851,
- [168] Neto, J.P., Baião, P., Lopes, G., Frazão, J., Nogueira, J., Fortunato, E., Barquinha, P., Kampff, A.R., Does Impedance Matter When Recording Spikes With Polytrodes? *Frontiers in neuroscience*, 12 (2018), doi:10.3389/fnins.2018.00715,
- [169] Rocha, P.R.F., Schlett, P., Kintzel, U., Mailänder, V., Vandamme, L.K.J., Zeck, G., Gomes, H.L., Biscarini, F., Leeuw, D.M. de, Electrochemical noise and impedance of Au

- electrode/electrolyte interfaces enabling extracellular detection of glioma cell populations, *Scientific reports*, 6 (1) (2016), 34843, doi:10.1038/srep34843.
- [170] Wang, A., Jung, D., Lee, D., Wang, H., Impedance Characterization and Modeling of Subcellular to Micro-sized Electrodes with Varying Materials and PEDOT:PSS Coating for Bioelectrical Interfaces, *ACS Applied Electronic Materials*, 3 (12) (2021), 5226–5239, doi:10.1021/acsaelm.1c00687.
- [171] Fairfield, J.A., Nanostructured Materials for Neural Electrical Interfaces, *Adv. Funct. Mater.*, 28 (12) (2018), 1701145, doi:10.1002/adfm.201701145.
- [172] Jonathan Rivnay, Huiliang Wang, Lief Fenno, Karl Deisseroth, George G. Malliaras, Next-generation probes, particles, and proteins for neural interfacing, *Science Advances*, 3 (6) (2017), e1601649, doi:10.1126/sciadv.1601649.
- [173] Arcot Desai, S., Rolston, J., Guo, L., Potter, S., Improving impedance of implantable microwire multi-electrode arrays by ultrasonic electroplating of durable platinum black, *Frontiers in Neuroengineering*, 3 (2010), doi:10.3389/fneng.2010.00005,
- [174] Boehler, C., Oberueber, F., Schlabach, S., Stieglitz, T., Asplund, M., Long-Term Stable Adhesion for Conducting Polymers in Biomedical Applications: IrOx and Nanostructured Platinum Solve the Chronic Challenge, *ACS Applied Materials & Interfaces*, 9 (1) (2017), 189–197, doi:10.1021/acsaami.6b13468.
- [175] Tang, R., Pei, W., Chen, S., Zhao, H., Chen, Y., Han, Y., Wang, C., Chen, H., Fabrication of strongly adherent platinum black coatings on microelectrodes array, *Science China Information Sciences*, 57 (4) (2014), 1–10, doi:10.1007/s11432-013-4825-6.
- [176] Rocha, P.R.F., Schlett, P., Kintzel, U., Mailänder, V., Vandamme, L.K.J., Zeck, G., Gomes, H.L., Biscarini, F., Leeuw, D.M. de, Electrochemical noise and impedance of Au electrode/electrolyte interfaces enabling extracellular detection of glioma cell populations, *Scientific reports*, 6 (1) (2016), 34843, doi:10.1038/srep34843.

# Jelena Petrovic

---

## LEBENS LAUF

Geburtsdatum und -ort	07.03.1990, Brcko, Bosnien und Herzegovinen
Staatsangehörigkeit	Bosnisch
Familienstand	verheiratet
Anschrift	Carl von Ossietzky Strasse, 18147 Rostock

## UNIVERSITÄRER WERDEGANG

01/2019 – heute	<b>Doktorandin</b> Institut für Gerätesysteme und Schaltungstechnik, Universität Rostock <b>Forschungsschwerpunkte:</b> Mikrosystemtechnik, Optogenetik, Optroden, Faser Optik
10/2015 - 09/2016	<b>Master Physik (Materialien)</b> Universität Novi Sad, Institut für Physik, Novi Sad, Serbien
09/2009 - 02/2014	<b>Bachelor Physik</b> Universität Novi Sad, Institut für Physik, Novi Sad, Serbien

## BERUFLICHER WERDEGANG

01/2019 - heute	<b>Wissenschaftliche Mitarbeiterin</b> Universität Rostock Fakultät für Gerätesysteme und Schaltungstechnik Rostock, Deutschland
11/2016 - 12/2018	<b>Wissenschaftliche Mitarbeiterin</b> Friedrich Schiller Universität Jena Otto Schott Institut für Materialsforschung Jena, Deutschland